UCRL-JRNL-229539

LAWRENCE LIVERMORE NATIONAL LABORATORY

Quantification of corrosion resistance of a new-class of criticality control materials – thermal-spray coatings of high-boron iron-based amorphous metals: $Fe_{49.7}Cr_{17.7}Mn_{1.9}Mo_{7.4}W_{1.6}B_{15.2}C_{3.8}Si_{2.4}$

Authors:

J. C. Farmer, J-S. Choi, C-K. Saw, R. H. Rebak, S. D. Day, T. Lian and P. D. Hailey , *Lawrence Livermore National Laboratory, Livermore, California*

J. H. Payer, *Case Western Reserve University, Cleveland, Ohio*

D. J. Branagan, *The NanoSteel Company, Idaho Falls, Idaho*

L. F. Aprigliano, *Strategic Analysis, Arlington, Virginia*

Journal of Nuclear Technology
May 10, 2007

This document was prepared as an account of work sponsored by an agency of the United States government. Neither the United States government nor Lawrence Livermore National Security, LLC, nor any of their employees makes any warranty, expressed or implied, or assumes any legal liability or responsibility for the accuracy, completeness, or usefulness of any information, apparatus, product, or process disclosed, or represents that its use would not infringe privately owned rights. Reference herein to any specific commercial product, process, or service by trade name, trademark, manufacturer, or otherwise does not necessarily constitute or imply its endorsement, recommendation, or favoring by the United States government or Lawrence Livermore National Security, LLC. The views and opinions of authors expressed herein do not necessarily state or reflect those of the United States government or Lawrence Livermore National Security, LLC, and shall not be used for advertising or product endorsement purposes.

Quantification of corrosion resistance of a new-class of criticality control materials – thermal-spray coatings of high-boron iron-based amorphous metals: $Fe_{49.7}Cr_{17.7}Mn_{1.9}Mo_{7.4}W_{1.6}B_{15.2}C_{3.8}Si_{2.4}$ (DRAFT)

J. C. Farmer, J-S. Choi, C-K. Saw, R. H. Rebak, S. D. Day, T. Lian and P. D. Hailey
Lawrence Livermore National Laboratory, Livermore, California

J. H. Payer
Case Western Reserve University, Cleveland, Ohio

D. J. Branagan
The NanoSteel Company, Idaho Falls, Idaho

L. F. Aprigliano
Strategic Analysis, Arlington, Virginia

An iron-based amorphous metal, $Fe_{49.7}Cr_{17.7}Mn_{1.9}Mo_{7.4}W_{1.6}B_{15.2}C_{3.8}Si_{2.4}$ (SAM2X5), with very good corrosion resistance was developed. This material was produced as a melt-spun ribbon, as well as gas atomized powder and a thermal-spray coating. Chromium (Cr), molybdenum (Mo) and tungsten (W) provided corrosion resistance, and boron (B) enabled glass formation. The high boron content of this particular amorphous metal made it an effective neutron absorber, and suitable for criticality control applications. Earlier studies have shown that ingots and melt-spun ribbons of these materials have good passive film stability in these environments. Thermal spray coatings of these materials have now been produced, and have undergone a variety of corrosion testing, including both atmospheric and long-term immersion testing. The modes and rates of corrosion have been determined in the various environments, and are reported here.

I. INTRODUCTION

The outstanding corrosion that may be possible with amorphous metals was recognized several years ago.[1-4] Compositions of several iron-based amorphous metals were published, including several with very good corrosion resistance. Examples included: thermally sprayed coatings of Fe-10Cr-10-Mo-(C,B), bulk Fe-Cr-Mo-C-B, and Fe-Cr-Mo-C-B-P.[5-7] The corrosion resistance of an iron-based amorphous alloy with yttrium (Y), $Fe_{48}Mo_{14}Cr_{15}Y_2C_{15}B_6$ was also been established.[8-12] Yttrium was added to this alloy to lower the critical cooling rate. Several nickel-based amorphous metals were developed that exhibit exceptional corrosion performance in acids.[13] Very good thermal spray coatings of nickel-based crystalline coatings were deposited with thermal spray, but appear to have less corrosion resistance than nickel-based amorphous metals.[14]

A family of iron-based amorphous metals with very good corrosion resistance was developed that can be applied as a protective thermal spray coating. One of the most promising formulations within this family was found to be $Fe_{49.7}Cr_{17.7}Mn_{1.9}Mo_{7.4}W_{1.6}B_{15.2}C_{3.8}Si_{2.4}$ (SAM2X5), which included chromium (Cr), molybdenum (Mo), and tungsten (W) for enhanced corrosion resistance, and boron (B) to enable glass formation and neutron absorption. The parent alloy for this series of amorphous alloys, which is known as SAM40 and represented by the formula $Fe_{52.3}Cr_{19}Mn_2Mo_{2.5}W_{1.7}B_{16}C_4Si_{2.5}$, has less molybdenum than SAM2X5 and was

originally developed by Branagan.[15-16] SAM2X5 may have beneficial for applications such as the safe long-term storage of spent nuclear fuel.[17-19]

Conclusions regarding the exceptional passive film stability and corrosion resistance of this iron-based amorphous alloy compared to crystalline reference materials were based on measurements of passive film breakdown potential and corrosion rate, as well as observed performance during salt fog testing. Such measurements enabled the corrosion performance of various iron-based amorphous alloys, carbon steel, iron-based stainless steels and nickel-based alloys to be directly compared.

The high boron content of $Fe_{49.7}Cr_{17.7}Mn_{1.9}Mo_{7.4}W_{1.6}B_{15.2}C_{3.8}Si_{2.4}$ (SAM2X5) makes it an effective neutron absorber, and suitable for criticality control applications. Average measured values of the neutron absorption cross section in transmission (Σ_t) for Type 316L stainless steel, Alloy C-22, borated stainless steel, Ni-Cr-Mo-Gd, and HVOF SAM2X5 have been determined to be approximately 1.1, 1.3, 2.3, 3.8 and 7.1, respectively, and are discussed in detail in a separate publication.[19] These average values are compared graphically in Figure 1, and were calculated from the values summarized in Table I. The high boron content of this particular amorphous metal makes this amorphous alloy an effective neutron absorber, and suitable for criticality control applications. The thermal spray coating of SAM2X5 has a significantly higher neutron absorption cross-section than either the Ni-Cr-Mo-Gd alloy, or the borated stainless steel, which are commonly used in the design of spent nuclear fuel containers. The effectiveness of SAM2X5 with natural boron as an absorber of thermal neutrons in nuclear applications is three-to-four times greater than the borated stainless steel samples tested, and twice as good as the Ni-Cr-Mo-Gd samples tested. This material and its parent alloy have been shown to maintain corrosion resistance up to the glass transition temperature, and to remain in the amorphous state after receiving relatively high neutron dose.

II. EXPERIMENTAL

A. Melt Spinning Process

Maximum cooling rates of one million Kelvin per second (10^6 K/s) have been achieved with melt spinning, which is an ideal process for producing amorphous metals over a very broad range of compositions. This process was used to synthesize completely amorphous, Fe-based, corrosion-resistant alloys with near theoretical density, and thereby enabled the effects of coating morphology on corrosion resistance to be separated from the effects of elemental composition. The melt-spun ribbon (MSR) samples produced with this equipment were several meters long, several millimeters wide and approximately 150 microns thick.

B. Thermal Spray Process

The coatings discussed here were made with the high-velocity oxy-fuel (HVOF) process, which involves a combustion flame, and is characterized by gas and particle velocities that are three to four times the speed of sound (mach 3 to 4). This process is ideal for depositing metal and cermet coatings, which have typical bond strengths of 5,000 to 10,000 pounds per square inch (5-10 ksi), porosities of less than one percent (< 1%) and extreme hardness. The cooling rate that can be achieved in a typical thermal spray process such as HVOF are on the order of ten thousand Kelvin per second (10^4 K/s), and are high enough to enable many alloy compositions to be deposited above their respective critical cooling rate, thereby maintaining the vitreous state. However, the range of amorphous metal compositions that can be processed with HVOF is more

restricted than those that can be produced with melt spinning, due to the differences in achievable cooling rates. Both kerosene and hydrogen have been investigated as fuels in the HVOF process used to deposit SAM2X5.

C. Energy Dispersive Spectroscopy

The target concentrations of heavier elements such as Cr, Mo and W were verified with Energy Dispersive Spectroscopy (EDS). Microanalysis of each sample was performed at three randomly selected locations at 10,000X magnification. Compositional analysis was performed on the smoother side of each melt-spun ribbon (MSR), as the rougher sides were found in some cases to be contaminated with small amounts of copper, presumably from contact with the copper wheel during the melt spinning process. The concentrations of relatively light elements such as B and C could not be determined with EDS, and were therefore estimated with a simple difference calculation, so that the sum of concentrations for all elements totaled one hundred percent.

D. X-Ray Diffraction

The basic theory for X-ray diffraction (XRD) of amorphous materials is well developed and has been published in the literature.[20-21] In an amorphous material, there are broad diffraction peaks. During this study, XRD was done with CuK_α X-rays, a graphite analyzing crystal, and a Philips vertical goniometer, using the Bragg-Bretano method. The X-ray optics were self-focusing, and the distance between the X-ray focal point to the sample position was equal to the distance between the sample position and the receiving slit for the reflection mode. Thus, the intensity and resolution was optimized. Parallel vertical slits were added to improve the scattering signal. Step scanning was performed from 20 to 90° (2θ) with a step size of 0.02° at 4 to 10 seconds per point, depending on the amount of sample. The samples were loaded into low-quartz holder since the expected intensity was very low, thus requiring that the background scattering be minimized.

E. Thermal Analysis

The thermal properties of these Fe-based amorphous metals have also been determined. Thermal analysis of these Fe-based amorphous metals, with differential scanning calorimetry (DSC) or differential thermal analysis (DTA), allowed determination of important thermal properties such as the glass transition temperature (T_g), crystallization temperature (T_x), and the melting point (T_m). Results from the thermal analysis of amorphous samples provides initial assessment of the glass forming ability of these materials through conventional metrics, such as the reduced glass transition temperature ($T_{rg} = T_g/T_L$).

F. Mechanical Properties

Hardness was also measured, since it determines wear resistance, as well as resistance to erosion-corrosion. Vickers micro-hardness (HV) was the standard approach used to assess the hardness of these thermal spray coatings. A 300-gram load was used since it was believed that this load and the affected area were large enough to sample across any existing macro-porosity, thereby producing a spatially averaged measurement. Micro-hardness measurements were also made with a 100-gram load since it was believed that this load and the affected area were small enough to accurately sample bulk material properties.

G. Salt Fog Testing

Salt fog tests were conducted according to the standard General Motors (GM) salt fog test, identified as GM9540P. The protocol for this test is summarized in Table II. The salt solution mists (denoted with asterisks) consisted of 1.25% solution containing 0.9% sodium chloride, 0.1% calcium chloride, and 0.25% sodium bicarbonate. The four reference samples included Type 316L stainless steel, nickel-based Alloy C-22, Ti Grade 7, and the 50:50 nickel-chromium binary.

H. Solutions for Immersion Testing

Several standardized test solutions have been developed based upon the well J-13 water composition determined by Harrar et al.[22] Relevant test environments are assumed to include simulated dilute water (SDW), SCW, and SAW at 30, 60, and 90°C, as well as SSW at 100 and 120°C. The compositions of all of the environments are given in Table III. The compositions of these test media are based upon the work of Gdowski et al.[23-46] In general, anions such as chloride promote localized corrosion, whereas other anions such as nitrate tend to act as corrosion inhibitors. Thus, there is a very complex synergism of corrosion effects in the test media.

The BSW composition was established on the basis of results from a distillation experiment by Wang et al.[27]. The total concentration of dissolved salts in the starting liquid was approximately five-times (5×) more concentrated than that in the standard SCW solution. It was prepared by using five-times the amount of each chemical that is specified for the preparation of SCW. After evaporation of approximately ninety percent (~90%) of the water from the starting solution, the residual solutions reaches the highest chloride concentration and has a boiling point of ~111°C. The resultant BSW solution contains (sampled at 111°C) 9% chloride, 9% nitrate, 0.6% sulfate, 0.1% fluoride, 0.1% metasilicate, 1% TIC (total inorganic carbon from carbonate and bicarbonate), 5% potassium ion and 11% sodium ion.

The synthetic BSW solution represented by Table IV has been slightly modified for these and other corrosion tests, yielding BSW-11, BSW-12, and BSW-13. The three solutions have pH values of approximately 13, 12, and 11 respectively. All BSW-type solutions contain 9% chloride, 9% nitrate, 0.6% sulfate, and 0.1% fluoride. Sodium and potassium ions are used to balance the charge. More specifically, each testing solution contains 8.7 g KCl, 7.9 g NaCl, 0.2 g NaF, 13.6 g $NaNO_3$, and 1.4 g Na_2SO_4 (anhydrous). The pH 13 solution (BSW-13) was prepared by adding 65 mL of water and 2.0 mL of the 10 N NaOH to the chemicals (total weight = 100 g). The measured pH was 13.13. The pH 12 solution (BSW-12) was prepared by adding 66 mL of water and 2.0 mL of the 1 N NaOH to the chemicals. The measured pH was 12.25. The pH 11 solution (BSW-11) was prepared by adding 66 mL of water and 2.0 mL of the 0.1 N NaOH to the chemicals.

I. Cyclic Polarization

Spontaneous breakdown of the passive film and localized corrosion require that the open-circuit corrosion potential exceed the critical potential:

$$E_{corr} \geq E_{critical} \qquad (1)$$

The resistance to localized corrosion is quantified through measurement of the open-circuit corrosion potential (E_{corr}), the breakdown or critical potential ($E_{critical}$), and the repassivation

potential (E_{rp}). The greater the difference between the open-circuit corrosion potential and the critical potential (ΔE), the more resistant a material is to modes of localized corrosion such a pitting and crevice corrosion. In integrated corrosion models, general corrosion is invoked when E_{corr} is less than $E_{critical}$ ($E_{corr} < E_{critical}$), and localized corrosion is invoked when E_{corr} exceeds $E_{critical}$.[29] Measured values of the repassivation potential (E_{rp}) are sometimes used as conservative estimates of the critical potential ($E_{critical}$).

In the published scientific literature, different bases exist for determining the critical potential from electrochemical measurements.[29-31] The breakdown or critical potential has been defined as the potential where the passive current density increases to a level between 1 to 10 μA/cm^2 (10^{-6} to 10^{-5} A/cm^2) while increasing potential in the positive (anodic) directing during cyclic polarization or potential-step testing. The repassivation potential has been defined as the potential where the current density drops to a level indicative of passivity, which has been *assumed* to be between 0.1 to 1.0 μA/cm^2 (10^{-6} to 10^{-7} A/cm^2), while decreasing potential from the maximum level reached during cyclic polarization or potential-step testing. Alternatively, the repassivation potential has been defined as the potential during cyclic polarization where the forward and reverse scans intersect, a point where the measured current density during the reverse scan drops to a level *known* to be indicative of passivity.

Cyclic polarization (CP) measurements was based on a procedure similar to ASTM (American Society for Testing and Materials) G-5 and other similar standards, with slight modification.[32-35] The ASTM G-5 standard calls for a 1N H_2SO_4 electrolyte, whereas synthetic bicarbonate, sulfate-chloride, chloride-nitrate, and chloride-nitrate solutions, with sodium, potassium and calcium cations, as well as natural seawater were used for this investigation. The natural seawater used in these tests was obtained directly from Half Moon Bay along the northern coast of California. Furthermore, the ASTM G-5 standard calls for the use of de-aerated solutions, whereas aerated and de-aerated solutions were used here. In regard to current densities believed to be indicative of passivity, all data was interpreted in a manner consistent with the published literature.[28-30]

Temperature-controlled borosilicate glass (Pyrex) electrochemical cells were used for cyclic polarization and other similar electrochemical measurements. This cell had three electrodes, a working electrode (test specimen), a reference electrode, and a counter electrode. A standard silver silver-chloride electrode, filled with near-saturation potassium chloride solution, was used as the reference, and communicated with the test solution via a Luggin probe placed in close proximity to the working electrode, which minimized Ohmic losses. The electrochemical cell was equipped with a water-cooled junction to maintain reference electrode at ambient temperature, which thereby maintained integrity of the potential measurement, and a water-cooled condenser, which prevented the loss of volatile species from the electrolyte.

J. Linear Polarization

The linear polarization method was used as a method for determining the corrosion rates of the various amorphous metal coatings. The procedure used for linear polarization testing consisted of the following steps: (1) holding the sample for ten seconds at the OCP; (2) beginning at a potential 20 mV below the OCP, increasing the potential linearly at a constant rate of 0.1667 mV per second to a potential 20 mV above the OCP; (3) recording the current being passed from the counter electrode to the working electrode as a function of potential relative to a standard Ag/AgCl reference electrode; and (4) determining the parameters in the cathodic Tafel line by performing linear regression on the voltage-current data, from 10 mV below the OCP, to 10 mV

above the OCP. The slope of this line was the polarization resistance, *Rp* (ohms), and was defined in the published literature.[36] While no values for the Tafel parameter (*B*) of Fe-based amorphous metals have yet been developed, it was believed that a conservative value of approximately 25 mV was reasonable, based upon the range of published values for several Fe- and Ni-based alloys.[36] The corrosion current density was then defined in terms of *B*, R_p and *A*, the actual exposed area of the sample being tested. The general corrosion rate was calculated from the corrosion current density through application of Faraday's Law: [37]

$$R_P = \left(\frac{\partial E}{\partial I}\right)_{E_{corr}} \tag{2}$$

A parameter (*B*) was defined in terms of the slopes of the anodic and cathodic branches of the Tafel line:

$$B = \frac{\beta_a \beta_c}{2.303(\beta_a + \beta_c)} \tag{3}$$

Values of B were published for a variety of iron-based alloys, and varied slightly from one alloy-environment combination to another.[36] Values for carbon steel, as well as Type 304, 304L and 430 stainless steels, in a variety of electrolytes which include seawater, sodium chloride, and sulfuric acid, ranged from 19 to 25 mV. A value for nickel-based Alloy 600 in lithiated water at 288°C was given as approximately 24 mV. While no values have yet been developed for the Fe-based amorphous metals that are the subject of this investigation, it was believed that a conservative representative value of approximately 25 mV was appropriate for the conversion of polarization resistance to corrosion current. Given the value for Alloy 600, a value of 25 mV was also believed to be acceptable for converting the polarization resistance for nickel-based Alloy C-22 to corrosion current. The corrosion current, I_{corr} (A) was then defined as:

$$I_{corr} = \frac{B}{R_p} \tag{4}$$

The parameter B was conservatively assumed to be approximately 25 mV. The corrosion current density, i_{corr} (A cm^{-2}), was defined as the corrosion current, normalized by electrode area, and was:

$$i_{corr} = \frac{I_{corr}}{A} \tag{5}$$

A was the surface area of the sample in square centimeters (cm^2). The corrosion (or penetration) rates of the amorphous alloy and reference materials were calculated from the corrosion current densities with the following formula, which was similar to that given by Jones: [37]

$$\frac{dp}{dt} = \frac{i_{corr}}{\rho_{alloy} n_{alloy} F} \tag{6}$$

where p was the penetration depth, t was time, i_{corr} was the corrosion current density, ρ_{alloy} was the density of the alloy (g cm^{-3}), n_{alloy} was the number of gram equivalents per gram of alloy, and F was Faraday's constant. The value of n_{alloy} was calculated with the following formula:

$$n_{alloy} = \sum_j \left(\frac{f_j n_j}{a_j} \right) \tag{7}$$

where f_j was the mass fraction of the jth alloying element in the material, n_j was the number of electrons involved in the anodic dissolution process, which was assumed to be congruent, and a_j was the atomic weight of the jth alloying element. Congruent dissolution was assumed, which meant that the dissolution rate of a given alloy element was proportional to its concentration in the bulk alloy. These equations were used to calculate factors for the conversion of corrosion current density to the penetration rate (corrosion rate).

K. Junction Potential Correction

It is important to understand the magnitude of the error in the potential measurements due to the junction potential. Consistent with the methods given by Bard and Faulkner, a correction was performed based upon the Henderson Equation.[37] Calculated junction potentials for several test solutions were estimated with ionic properties taken from Bard and Faulkner. These corrections were not very large, with the largest being less than approximately 10 mV. It was therefore concluded that no significant error would result from neglecting the junction potential correction.

III. EXPERIMENTAL RESULTS

A. Elemental Composition

A systematic study of various elemental compositions, each based on the Fe-based SAM40 composition, with additions of specific elements believed to be beneficial to glass formation or corrosion resistance. Elemental additions investigated included nickel (Ni), molybdenum (Mo), yttrium (Y), titanium (Ti), zirconium (Zr) and chromium (Cr). The SAM2X-series of amorphous alloys was prepared by adding one, three, five and seven atomic percent (1, 3, 5 and 7 atomic %) Mo to the parent alloy, $Fe_{52.3}Mn_2Cr_{19}Mo_{2.5}W_{1.7}B_{16}C_4Si_{2.5}$ (SAM40), and were designated SAM2X1, SAM2X3, SAM2X5 and SAM2X7, respectively. The $Fe_{49.7}Cr_{17.7}Mn_{1.9}Mo_{7.4}W_{1.6}B_{15.2}C_{3.8}Si_{2.4}$ (SAM2X5) provided adequate corrosion resistance, and was a formulation that could be processed with relative ease. The SAM2X7 composition had a higher calculated pitting-resistance equivalence number (PREN) than the alloys with less molybdenum, and slightly better corrosion resistance than SAM2X5, but was somewhat more difficult to make.

The target compositions of these amorphous alloys, Type 316L stainless steel (UNS # S31603), and nickel-based Alloy C-22 (UNS # N06022) are given in Table V. Energy dispersive X-ray spectroscopy (EDS) was used to confirm the concentrations of heavy elements such as Cr, Mo, and W, with representative data for a series of melt-spun ribbons shown in Table VI. The concentrations of relatively light elements such as B and C could not be determined with EDS, and were therefore estimated with a simple difference calculation, so that the sum of concentrations for all elements totaled one hundred percent.

B. Amorphous Structure

X-ray diffraction (XRD) was done with SAM2X5 gas-atomized powder identified as Lot # 05-079. Measurements of X-ray intensity as a function of diffraction angle (2θ) are shown in Figure 2 and shows devitrification, and the formation of deleterious crystalline phases, including bcc ferrite and Cr_2B.

As shown in Figure 3, XRD data was also obtained with a SAM2X5 thermal spray coating produced with Lot # 05-079 powder and deposited on Type 316L stainless steel substrate. The broad halo observed at 2θ ~ 44° is due to the presence of the the amorphous matrix, while the pronounced sharp peaks are attributed to the presence of crystalline phases. These phases are believed to include Cr_2B, WC, $M_{23}C_6$ and bcc ferrite, and are known to have a detrimental effect on corrosion resistance. These deleterious precipitates deplete the amorphous matrix of those alloying elements, such as Cr, Mo and W responsible for enhanced passivity. The distinctive satellite peak at 2θ ~ 36° may be due to the formation of tungsten carbide during the thermal spray process. Note that this satellite is absent in the XRD data for the feed powder. The structure seen near 2θ ~ 60° may be due to bcc ferrite, and has been correlated with increased susceptibility of such amorphous metal coatings to corrosion. Other structure is due to $M_{23}C_6$ and Cr_2B. Coatings with less residual crystalline phase have been successfully produced, and will be discussed subsequently.

X-ray diffraction (XRD) was done with SAM2X5 gas-atomized powder identified as Lot # 06-015. Measurements of X-ray intensity as a function of diffraction angle (2θ) are shown in Figure 4. The broad halos observed at 2θ ~ 44° and 78° indicated that the powder was essentially amorphous, with very little residual crystalline structure. This amorphous powder was used to prepare the thermal-spray coatings tested during this study.

As shown in Figure 5, XRD data was also obtained with a SAM2X5 thermal spray coating produced with Lot # 06-015 powder and deposited on an Alloy C-22 substrate, identified as Sample # CC-22 4019. The broad halo observed at 2θ ~ 44° indicated that the coating was predominately amorphous, and the small sharp peaks are attributed to the presence of minor crystalline phases. These phases are believed to include Cr_2B, WC, $M_{23}C_6$ and bcc ferrite, which are known to have a detrimental effect on corrosion performance. These potentially deleterious precipitates deplete the amorphous matrix of those alloying elements, such as chromium, responsible for enhanced passivity. Coatings with less residual crystalline phase have been observed. The distinctive satellite peak at 2θ ~ 36° may be due to the formation of tungsten carbide during the thermal spray process. Note that this satellite is absent in the XRD data for the feed powder. The structure seen near 2θ ~ 60° may be due to bcc ferrite, and has been correlated with increased susceptibility of such amorphous metal coatings to corrosion. Other structure is due to $M_{23}C_6$ and Cr_2B.

As shown in Figure 6, XRD data was also obtained with a SAM2X5 thermal spray coating produced with Lot # 06-015 powder and deposited on a Type 316L stainless steel substrate, identified as Sample # E316L511. The broad halo observed at 2θ ~ 44° indicated that the coating was predominately amorphous, and the small sharp peaks are attributed to the presence of minor crystalline phases. These phases are believed to include Cr_2B, WC, $M_{23}C_6$ and bcc ferrite, which are known to have a detrimental effect on corrosion performance. These potentially deleterious precipitates deplete the amorphous matrix of those alloying elements, such as chromium, responsible for enhanced passivity. Coatings with less residual crystalline phase have been observed. The distinctive satellite peak at 2θ ~ 36° may be due to the formation of tungsten carbide during the thermal spray process. Note that this satellite is absent in the XRD data for the

feed powder. The structure seen near 2θ ~ 60° may be due to bcc ferrite, and has been correlated with increased susceptibility of such amorphous metal coatings to corrosion. Other structure is due to $M_{23}C_6$ and Cr_2B.

C. Thermal Properties

The thermal properties of these Fe-based amorphous metals have been determined. $Fe_{49.7}Cr_{17.7}Mn_{1.9}Mo_{7.4}W_{1.6}B_{15.2}C_{3.8}Si_{2.4}$ (SAM2X5) has a glass transition temperature of ~579°C, a crystallization temperature of ~628°C, a melting point of ~1133°C, and a reduced glass transition temperature of ~0.57 (with a value of 0.6 being ideal). SAM2X7, an alloy in the same family as SAM2X5, but with more molybdenum, had a glass transition temperature of ~573°C, a crystallization temperature of ~630°C, a melting point of ~1137°C, and a reduced glass transition temperature of 0.57. In contrast, yttrium-containing $Fe_{48}Mo_{14}Cr_{15}Y_2C_{15}B_6$ (SAM1651) had a glass transition temperature of ~584°C, a crystallization temperature of ~653°C, a melting point of ~1121°C, and a reduced glass transition temperature of ~0.55. The critical cooling rates for SAM2X7 and SAM1651, have been determined to be ~ 610 and ≤ 80 K per second, respectively. Clearly, the yttrium additions in SAM1651 enhance glass-forming ability of these materials.

Thermal analysis data (DTA or DSC) for Fe-based glass forming alloys suitable for thermal spray deposition are summarized in Table VII. The two formulations of greatest interest at the present time are SAM2X5 ($Fe_{49.7}Cr_{17.7}Mn_{1.9}Mo_{7.4}W_{1.6}B_{15.2}C_{3.8}Si_{2.4}$), which has a relatively high CCR, and yttrium-containing SAM1651 ($Fe_{48.0}Cr_{15.0}Mo_{14.0}B_{6.0}C_{15.0}Y_{2.0}$), which has a relatively low CCR. These selections are based upon their good corrosion resistance and relative ease or processing.

D. Mechanical Properties

As previously discussed, hardness determines wear resistance, as well as resistance to erosion-corrosion. Vickers micro-hardness (HV) was the standard approach used to assess the hardness of these thermal spray coatings. A 300-gram load was used since it was believed that this load and the affected area were large enough to sample across any existing macro-porosity, thereby producing a spatially averaged measurement. Micro-hardness measurements were also made with a 100-gram load since it was believed that this load and the affected area were small enough to accurately sample bulk material properties. Measurements of the micro-hardness of Fe-based amorphous metal thermal spray coatings are given in Table VIII, and show the exceptional hardness of these materials.

E. Salt-Fog Performance

Early salt fog testing confirmed the corrosion resistance of the corrosion resistance of thermal spray coatings of SAM2X5 relative to other alloys with less molybdenum. As previously discussed, these coatings were deposited with the high-velocity oxy-fuel (HVOF) process, using amorphous metal powders. HVOF coatings of Type 316L stainless steel and the parent alloy, SAM40, showed significant rusting after only 13 cycles in the GM salt fog test. In contrast, HVOF coatings on nickel-based Alloy C-22 and amorphous SAM2X5 showed no obvious corrosion or rusting after more than 60 cycles. Figure 21 shows several samples coated with SAM2X5, prepared with Lot # 06-015 powder and thermally sprayed with the JK2000 gun using hydrogen fuel, and 1018 carbon steel samples, after eight full cycles in the GM salt fog test. No rust was observed with this thermally sprayed amorphous metal coating, while substantial attack

of the 1018 carbon steel was observed. Such amorphous metal coatings may therefore provide a good means for protecting less corrosion resistant surfaces.

As shown in Figure 7, reference samples of 1018 carbon steel after eight (8) full cycles in the GM salt fog test. These samples were tested at the same time as a half-scale spent nuclear fuel container that was coated with SAM2X5. Severe corrosion of the carbon steel was observed, while the SAM2X5 coating did not experience corrosion.

As shown in Figure 8, a half-scale model of a container for the storage of spent nuclear fuel was fabricated from Type 316L stainless steel, Schedule 10s pipe. A hydrogen-fueled HVOF process was used to coat the outer diameter of this container with SAM2X5, using powder Lot # 06-015. This coated container was then subjected to eight (8) full cycles in the GM salt fog test. As shown in this photograph, no significant corrosion of the coating was evident during this salt fog testing.

As shown in Figure 9, three sections of the SAM2X5-coated half-scale SNF container are shown after eight (8) full cycles in the GM salt fog test. As previously discussed, no significant corrosion was observed during this test. In the left frame, a single spot showed rust, which is an area where the coating appears to have been accidentally removed by gouging during handling. Slight discoloration was observed in a band of coating near the center of the container (center frame), and on a spot on the bottom edge of the container (right frame).

As shown in Figure 10, photographs of 1018 carbon steel reference specimens (Sample # A35), before (left) and after (right) 8 abbreviated cycles in GM salt fog test.

As shown in Figure 11, photographs of 1018 carbon steel reference specimens (Samples # A14), before (left) and after (right) 8 full cycles in GM salt fog test.

As shown in Figure 12, photographs showing of HVOF coating of 316 stainless steel on Type 316L stainless steel substrate (Sample # 316-170), before (left) and after (right) 8 abbreviated cycles in GM salt fog test.

As shown in Figure 13, photographs of HVOF coating of Alloy C-22 on Type 316L stainless steel substrate, (Sample # 316-238), before (left) and after (right) 8 abbreviated cycles in GM salt fog test.

As shown in Figure 14, photographs of early HVOF SAM40 coating on Type 316L stainless steel substrate (Sample # 316-041), before (left) and after (right) 8 abbreviated cycles in GM salt fog test.

As shown in Figure 15, photographs of early HVOF coating of SAM40X3 on Type 316L stainless steel substrate (Sample # 316-095), before (left) and after (right) 8 abbreviated cycles in GM salt fog test.

As shown in Figure 16, photograph of HVOF coating of SAM2X5 on Type 316L stainless steel substrate (Sample # 316L-W9), before (left) and after (right) 8 full cycles in GM salt-fog test. The arrows were added to the image to pinpoint small suspected rust spots.

As shown in Figure 17, photograph of HVOF coating of SAM2X5 on nickel-based Alloy C-22 substrate (Sample # C22-W21), before (left) and after (right) 8 full cycles in GM salt-fog test. There were no suspected rust spots observed on this specimen.

F. Electrochemical Behavior – Cyclic Polarization Measurements

As shown in Figure 18, this figure shows CP data for a melt-spun ribbon (MSR) and for a high-velocity oxy-fuel (HVOF) coating of SAM2X5 in 3.5-molal solution of NaCl at 90°C. The SAM2X5 coating was prepared by depositing Lot # 06-015 powder on a Type 316L stainless steel substrate, using a hydrogen-fueled thermal spray process. CP data are also shown for two

austenitic neutron-absorbing steel, the first being a Ni-Cr-Mo-Gd alloy and the second being a borated stainless steel. All potentials were measured relative to the standard Ag/AgCl reference electrode.

By a very large margin, the greatest passive film stability was observed with the SAM2X5 melt-spun ribbon. A very low passive current density (≤ 1 μA cm^{-2}) was maintained during the anodic potential scan, from the OCP of approximately –0.2 V, to the passive film breakdown potential of ~ 0.9 V. After scan reversal at a relatively high potential of ~ 1.1 V, a relatively small hyseresis loop was observed, with a repassivation potential found between 0.8 and 0.7 V.

In the case of the borated stainless steel, passivity was maintained during the anodic potential scan, from the OCP of approximately –0.6 V to a level of approximately –0.3 V, where passive film breakdown occurred. Following potential reversal at approximately –0.2 V, a large hysteresis loop was observed, with no subsequent repassivation observed, which indicates that this alloy could experience spontaneous passive film breakdown in this type of environment.

In the case of the Ni-Cr-Mo-Gd alloy, a broad oxidation peak was observed during the anodic potential scan, from the OCP which was between –0.5 and –0.6 V, and the reversal potential, which was approximately 0.2 V. This oxidation peak may have resulted in the formation of a relatively conductive surface oxide. Following voltage reversal, a small hysteresis loop was observed, with intersection of the forward and reverse scans at 0 V, which may be the repassivation potential.

In the case of the SAM2X5 coating, which was also prepared with Lot # 06-015 powder and a hydrogen-fueled HVOF process, the current density increased steadily during the anodic potential scan from approximately 10 μA cm^{-2} at the OCP of approximately –0.4 V to almost 5,000 μA cm^{-2} at the reversal potential, which was between 0.9 and 1.0 V. This steady rise in current density indicates that this coating has relatively poor passive film stability in concentrated chloride solutions near their boiling point. The forward and reverse scans intersected at approximately –0.3 V, which may define the repassivation potential.

Figure 19 shows CP data for high-velocity oxy-fuel (HVOF) coatings of SAM2X5 in 3.5-molal NaCl solution at 30 and 90°C, and for HVOF coating of SAM2X5 in 3.5-molal NaCl solution at 90°C after the addition of 0.525-molal KNO_3. The inhibitory effects of nitrate, which would be expected in actual electrolytes, is significant.

Figure 20 shows CP data for a high-velocity oxy-fuel (HVOF) coating of SAM2X5 in four concentrated bicarbonate-type brines at 30°C. The four brines are known as simulated dilute water (SDW), simulated concentrated water (SCW), simulated acidified water (SAW), and basic saturated water (BSW). All are based upon the composition of well J-13 water at Yucca Mountain. The SAM2X5 coating was prepared by depositing Lot # 06-015 powder on a Type 316L stainless steel substrate, using a hydrogen-fueled thermal spray process. All potentials were measured relative to the standard Ag/AgCl reference electrode.

In the case of SDW, the potential was scanned from the OCP of approximately –0.3 V to a reversal potential of 1.2 V. The passive current density increased from ~ 0.5 μA cm^{-2} near the OCP to ~ 5 μA cm^{-2} at ~ 0.9 V. As the potential continued to increase from 0.9 V to the reversal potential, the current density increased to a plateau, with the appearance of small-amplitude electrochemical noise, which may be attributed to the onset of passive film breakdown at this high applied potential. After scan reversal, very little hysteresis was observed, which indicates that the passive film was left virtually intact, even after applying a potential as high as 1.2 V. The passive current density was about one order-of-magnitude lower during the reverse scan, which

may be due to the depletion of available charge carriers within the intact passive film during anodic polarization. Such depletion would lower conductivity and current density.

Observations in the more concentrated bicarbonate-type brine, known as SCW, were qualitatively similar to those in the SDW electrolyte. However, in the more concentrated electrolyte, the current densities were substantially higher, ranging from 50 μA cm^{-2} near the OCP to 500 μA cm^{-2} at ~ 1.0 V, prior to scan reversal. During the anodic potential scan, the anodic oxidation peak at ~ 0.4 volts is observed which is believed to be associated with the oxidation of molybdenum species within the oxide film, or at the surface. There appears to be a corresponding reduction process (possible cathodic peak) during the reverse scan, which implies that the oxidation process is reversible.

Observations in the concentrated and acidified bicarbonate-type brine, known as SAW, were qualitatively similar to those in the SDW electrolyte. However, in this concentrated and acidified electrolyte at ~ 1.0 V, prior to scan reversal, the current density was 5 mA cm^{-2}, which is higher than that observed in SDW and SCW at similar potentials. During the anodic potential scan, the anodic oxidation peak at ~ 0.4 volts is observed which is believed to be associated with the oxidation of molybdenum species within the oxide film, or at the surface. A corresponding reduction process (cathodic peak) is clearly visible during the reverse scan, which implies that the oxidation process is reversible.

In basic concentrated water, known as BSW, the current density increased from 5 μA cm^{-2} near the OCP to 50 μA cm^{-2} at 0.9 V. As the scan continued to the reversal potential, the current density increased substantially, which indicated passive film breakdown, with a large hysteresis loop appearing during the reverse scan. The forward and reverse scans intersect at approximately –0.1 V, approximately 0.1 V above the observed OCP, which could be interpreted as the repassivation potential.

Figure 21 shows CP data for a high-velocity oxy-fuel (HVOF) coating of SAM2X5 in four concentrated bicarbonate-type brines at 90°C. The four brines are known as simulated dilute water (SDW), simulated concentrated water (SCW), simulated acidified water (SAW), and basic saturated water (BSW). All are based upon the composition of well J-13 water at Yucca Mountain. The SAM2X5 coating was prepared by depositing Lot # 06-015 powder on a Type 316L stainless steel substrate, using a hydrogen-fueled thermal spray process. All potentials were measured relative to the standard Ag/AgCl reference electrode.

In the case of SDW, the potential was scanned from the OCP of approximately –0.6 V to a reversal potential of 1.2 V, both relative to the Ag/AgCl reference electrode. The passive current density increased from ~ 5 μA cm^{-2} near the OCP to ~ 50 μA cm^{-2} at ~ 0.9 V. As the potential continued to increase from 0.9 V to the reversal potential, the current density increased to a plateau, with the appearance of small-amplitude electrochemical noise, which may be attributed to the onset of passive film breakdown at this high applied potential. After scan reversal, a small hysteresis loop was observed, which indicated that the passive film was degraded relatively little, even after applying a potential as high as 1.2 V. The forward and reverse scans intersected at a potential of approximately 0.6 V, which formally defines the repassivation potential in this environment. As the scan continued below the repassivation potential, the observed passive current density was lower than it was during the forward scan, which may be due to the depletion of available charge carriers within the intact passive film during anodic polarization. Such depletion would lower conductivity and current density.

In the case of the concentrated and acidified bicarbonate-type brine, known as SAW, the current density observed during the forward potential scan was relatively high, indicating

substantial electrochemical activity in this acidic electrolyte. A broad peak in current density extends from the OCP to a potential of approximately 0.6 V. As the scan continues, the current density first decreased to ~ 100 μA cm^{-2}, and then increased to 10,000 μA cm^{-2} at the reversal potential of 1.1 V. After scan revsersal, the forward and reverse scans intersected at a potential between 0.7 and 0.8 V, and continued to drop to a passive current density of ~ 10 μA cm^{-2} at ~ 0.5 V. As the scan continued below the point of repassivation, passivity appears to have once again been lost between 0.4 and –0.1 V, which is in the range of electrochemical activity observed during the forward scan. As the OCP was approached, the current density once again dropped to a level indicative of passivity.

In basic concentrated water, known as BSW, the passive current density increased from ~ 10 μA cm^{-2} near the OCP to ~ 50 μA cm^{-2} at a potential between 0.7 to 0.8 V. As the scan continued to the reversal potential of ~ 0.95 V, the current density increased substantially, forming a plateau with overlying electrochemical noise, which indicated the onset of passive film breakdown. A large hysteresis loop was observed during the reverse scan, which indicated that polarization near the reversal potential induced a loss of passivity. The forward and reverse scans intersect at approximately 0 V, approximately 0.3 V above the observed OCP, which is interpreted as the formal repassivation potential. All potentials were measured relative to the standard Ag/AgCl reference electrode.

As shown in Figure 22, cyclic polarization (CP) of two SAM2X5 coatings on Type 316L stainless steel substrates compared in natural seawater at 30°C, identified as E316L510 and E316L512, with reference data for two samples of wrought Ni-based Alloy C-22, identified as 4002 and 4006. These SAM2X5 coatings were prepared with powder Lot #06-015 using a hydrogen-fueled HVOF process. All potentials were measured relative to the standard silver/silver-chloride (Ag/AgCl) reference electrode.

The passive current density for the thermal spray coating of SAM2X5 was higher than that observed with Alloy C-22, which indicates that these particular samples of the Fe-based amorphous metal had less passive film stability than the wrought Ni-based alloy. In the case of the thermal spray coatings of SAM2X5, electrochemical noise was observed during the anodic branch of the polarization curve, between 0.8 V and the reversal potential, which is indicative of the onset of passive film breakdown and possible localized corrosion. After scan reversal, a complete loss of passivity is evident from the large hysteresis loops. The repassivation potential (E_{rp}), defined as the intersection of the forward and reverse scans, occurred between –0.2 and –0.4 V. The difference between the OCP and E_{rp} appears to approximately 0.1 V.

As shown in Figure 23, CP of two SAM2X5 coatings on Type 316L stainless steel substrates compared in natural seawater at 90°C, identified as E316L517 and E316L518, with reference data a sample of wrought Ni-based Alloy C-22, identified as JE1594. These SAM2X5 coatings were prepared with powder Lot #06-015 using a hydrogen-fueled HVOF process. All potentials were measured relative to the standard Ag/AgCl reference electrode.

In the case of the thermal spray coatings of SAM2X5, broad peaks in current density were observed during the anodic potential scan, between the OCP values and approximately 0.4 V. These broad peaks are due to anodic oxidation of the surface over this potential range, though it is unresolved whether the oxidation resulted in the formation of an oxide layer on the surface, dissolution of the metal, or both. Some degree of passivation appears to have been established at approximately 0.4 V. Electrochemical noise was also observed during the anodic potential scan, between 0.8 V and the reversal potential, and is indicative of the onset of passive film breakdown and possible localized corrosion. After scan reversal, a complete loss of passivity is evident from

the large hysteresis loops. The repassivation potential (E_{rp}), defined as the intersection of the forward and reverse scans, occurred between 0.4 and 0.6 V. The difference between the OCP and E_{rp} appears to approximately 0.6 V.

G. Electrochemical Behavior – Corrosion Potential & Linear Polarization Measurements

Linear polarization was used to determine the approximate corrosion rates of the thermal spray coatings of amorphous metals of interest (HVOF SAM2X5 and other coatings) and the reference material (wrought nickel-based Alloy C-22) in three relevant environments, natural seawater at two temperature levels, and in hot concentrated calcium chloride (5M $CaCl_2$ at 105°C). Linear polarization data for reference alloys and the Fe-based amorphous metals were converted to corrosion rates with the conversion factors given in Table IX. The penetration rates in this table are for an assumed current density of one microamp per square centimeter (1 μA cm^{-2}). If the corrosion rate is 2 μA cm^{-2} instead of the assumed 1 μA cm^{-2}, the penetration rate is simply doubled. The value of Faraday's constant (F) is 96,484.6 C $equiv^{-1}$.

Figure 24 shows values of the corrosion rate determined with linear polarization during long-term open circuit corrosion testing of SAM2X5 coating samples prepared with lots of powder produced in 2004, 2005 and 2006. As discussed in regard to the previous figure, the lots of powder produced in 2004 and 2006 are known to be amorphous, whereas the powder produced in 2005 contained substantial crystalline structure due to problems encountered with the gas atomization process during that period of time. By using the completely amorphous SAM2X5 powder produced in 2006, and known as Lot # 06-015, samples were produced that exhibited relatively low linear-polarization corrosion rate (LPCR) values in seawater at 90°C (~ 5 μm/yr), in comparison to those samples produced in 2005 with the SAM2X5 powder known as Lot # 05-079 (~ 5 μm/yr). Similarly, SAM2X5 coating samples produced with Lot # 06-015 powder exhibited relatively low LPCR values in 3.5-molal NaCl solution at 90°C (~ 100 μm/yr), in comparison to those samples with Lot # 05-079 powder (~ 20 μm/yr). Measurements of linear-polarization corrosion rate in 3.5-molal NaCl solution at 30°C were very similar for SAM2X5 coating samples produced with Lots # 06-015 and # 05-079 (~ 2 to 4 μm/yr). In general, the samples produced with the fully amorphous powder (Lot # 06-015) had lower LPCR values, and therefore greater corrosion resistance, in aggressive high-temperature brines than those produced with the powder that was substantially devitrified (Lot # 05-079).

Figure 25 shows values of the OCP determined during long-term open circuit corrosion testing of SAM2X5 coating samples prepared with lots of powder produced in 2004, 2005 and 2006. The lots of powder produced in 2004 and 2006 are known to be amorphous, whereas the powder produced in 2005 contained substantial crystallinity due to problems encountered with the gas atomization process during that period of time. By using the completely amorphous SAM2X5 powder produced in 2006, and known as Lot # 06-015, samples were produced that exhibited relatively low OCP values in seawater at 90°C (–275 to –300 mV), in comparison to those samples produced in 2005 with the SAM2X5 powder known as Lot # 05-079 (–250 mV). Similarly, SAM2X5 coating samples produced with Lot # 06-015 powder exhibited relatively low OCP values in 3.5-molal NaCl solution at 90°C (–290 mV), in comparison to those samples with Lot # 05-079 powder (–260 mV). The trend reversed with OCP measurements made in in 3.5-molal NaCl solution at 30°C; OCP values for SAM2X5 samples produced with Lot # 06-015 were higher than OCP values for samples produced with Lot # 05-079. In general, the samples

produced with the fully amorphous powder (Lot # 06-015) were more noble than those produced with the powder that was substantially devitrified (Lot # 05-079).

Figure 26 shows values of the LPCR values for SAM2X5 coating samples during immersion in seven different brines over period of approximately 135 days (the last linear polarization measurement made after 133 days). These samples were produced by depositing Lot #06-015 powder on Ni-based Alloy C-22 substrates with a hydrogen-fueled high-velocity oxy-fuel (HVOF) process. In the case of the LPCR and OCP measurements, the Alloy C-22 substrates were cylindrical rods, each having one hemispherical tip, with SAM2X5 deposited on the outer diameters of the rods, as well as over the entire surface of the hemispherical tip. The nominal length and diameter of each rod were 8 and 5/8 inches, respectively. The coating thickness was approximately 17 ± 2 mils. Test environments were: (1) natural seawater at 90°C; (2) 3.5-molal NaCl solution at 30°C; (3) 3.5-molal NaCl solution at 90°C; (4) 3.5-molal NaCl and 0.525-molal KNO_3 solution at 90°C; (5) simulated dilute water, referred to as SDW, at 90°C; (6) simulated concentrated water, referred to as SCW, at 90°C; and (7) simulated acidic water, referred to as SAW, at 90°C. After more than four months exposure, the LPCR values for these coatings in the seven test solutions were: (1) 12.3 μm/yr; (2) 2.91 μm/yr; (3) 176 μm/yr; (4) 2.83 μm/yr; (5) 2.61 μm/yr; (6) 12.4 μm/yr; and (7) 81.1 μm/yr, respectively. Clearly, the greatest electrochemical activities, which were quantified in terms of the measured LPCR values, were observed in 3.5-molal NaCl solution and SAW, both at 90°C, with the SAW having an acidic pH. The next highest LPCR values were observed in natural seawater and SCW, both at 90°C with near-neutral pH. Not surprisingly, the lowest LPCR values were observed in 3.5-molal NaCl solution and SDW, both at 30°C with near-neutral pH, as well as in 3.5-molal NaCl and 0.525-molal KNO_3 solution at 90°C. The nitrate inhibitor reduced the LPCR value observed in 3.5-molal NaCl solution from 176 to 2.83 μm/yr, nearly two orders-of-magnitude. The bar chart shown in the following figure summarizes these trends in corrosion rate graphically.

As shown in Figure 27, after 133 days immersion, LPCR values for SAM2X5 coatings were determined to be (1) 12.3 μm/yr in natural seawater at 90°C; (2) 2.91 μm/yr in 3.5-molal NaCl solution at 30°C; (3) 176 μm/yr in 3.5-molal NaCl solution at 90°C; (4) 2.83 μm/yr in 3.5-molal NaCl and 0.525-molal KNO_3 solution at 90°C; (5) 2.61 μm/yr in SDW at 90°C; (6) 12.4 μm/yr in SCW at 90°C; and (7) 81.1 μm/yr in SAW at 90°C.

Figure 28 shows values of the OCP for SAM2X5 coating samples during immersion in seven different brines over period of approximately 135 days. These samples were produced by depositing Lot #06-015 powder on Ni-based Alloy C-22 substrates with a hydrogen-fueled high-velocity oxy-fuel (HVOF) process. In the case of the OCP and LPCR measurements, the Alloy C-22 substrates were cylindrical rods, each having one hemispherical tip, with SAM2X5 deposited on the outer diameters of the rods, as well as over the entire surface of the hemispherical tip. The nominal length and diameter of each rod were 8 and 5/8 inches, respectively. The coating thickness was approximately 17 ± 2 mils. Test environments were: (1) natural seawater at 90°C; (2) 3.5-molal NaCl solution at 30°C; (3) 3.5-molal NaCl solution at 90°C; (4) 3.5-molal NaCl and 0.525-molal KNO_3 solution at 90°C; (5) simulated dilute water, referred to as SDW, at 90°C; (6) simulated concentrated water, referred to as SAW, at 90°C; and (7) simulated acidic water, referred to as SAW, at 90°C.

As shown in Figure 29, after 133 days immersion, OCP values for SAM2X5 coatings were determined to be (1) –322 mV in natural seawater at 90°C; (2) –138 mV in 3.5-molal NaCl solution at 30°C; (3) –296 mV in 3.5-molal NaCl solution at 90°C; (4) –219 mV in 3.5-molal

NaCl and 0.525-molal KNO_3 solution at 90°C; (5) –295 mV in SDW at 90°C; (6) –265 mV in SCW at 90°C; and (7) –188 mV in SAW at 90°C. All values were measured relative to a standard Ag/AgCl reference electrode.

Linear polarization was used to determine that the apparent corrosion rate of this SAM2X5 coating was approximately 12.3 μm/yr in natural seawater at 90°C after 133 days immersion with the sample shown in Figure 30. While there was relatively little corrosive attack of much of the coated surface, discrete nodules of corrosion product formed at several sites on the exposed coated cylinder. The insulating sheath covering the coated cylinder formed a crevice, with dark brown corrosion products formed at its mouth (left-hand side of the cylinder). The epoxy used to mask the hemispherical tip of the rod, and to seal the insulating sheath turned black in color during the test (right-hand end of cylinder).

Linear polarization was used to determine that the apparent corrosion rate of this SAM2X5 coating was approximately 2.91 μm/yr in 3.5-molal NaCl solution at 30°C after 133 days immersion with the sample shown in Figure 31. While there was relatively little corrosive attack of much of the coated surface, discrete nodules of corrosion product formed at several sites on the exposed coated cylinder. Here too the insulating sheath covering the coated cylinder formed a crevice, with dark brown corrosion products formed at its mouth (left-hand side of the cylinder). The epoxy used to mask the hemispherical tip of the rod, and to seal the insulating sheath turned black in color during the test (right-hand end of cylinder).

Linear polarization was used to determine that the apparent corrosion rate of this SAM2X5 coating was approximately 176 μm/yr in 3.5-molal NaCl solution at 90°C after 133 days immersion with the sample shown in Figure 32. In this case, there was substantial localized corrosion on the surface of the coated cylinder, with the prolific formation of corrosion product nodules over much of the surface. There may have been some corrosion within the crevice formed by the insulating sheath covering the cylinder, and shown on the left side of the photograph.

Linear polarization was used to determine that the apparent corrosion rate of this SAM2X5 coating was approximately 2.83 μm/yr in 3.5-molal NaCl and 0.525-molal KNO_3 solution at 90°C after 133 days immersion with the sample shown in Figure 33. While there is discoloration on the right end of the rod due to slight corrosion, the benefits of nitrate inhibitor in such near-boiling concentrated chloride electrolytes are easily seen by comparing this photograph to the previous figure.

Linear polarization was used to determine that the apparent corrosion rate of this SAM2X5 coating was approximately 2.61 μm/yr in SDW at 90°C after 133 days immersion with the sample shown in Figure 34. There is no visible evidence of corrosion in this case, and the sample was in pristine condition after this exposure.

Linear polarization was used to determine that the apparent corrosion rate of this SAM2X5 coating was approximately 12.4 μm/yr in SCW at 90°C after 133 days immersion with the sample shown in Figure 35. There was relatively little corrosion on the barrel of the coated cylinder, though there was slight discoloration which may be due to corrosion. The white deposited covering the metallic coating has been identified as precipitated salt from the test solution. Once again, the insulating sheath covering the coated cylinder formed a crevice, with dark brown corrosion products formed at its mouth (left-hand side of the cylinder). The epoxy used to mask the hemispherical tip of the rod, and to seal the insulating sheath turned black in color during the test (right-hand end of cylinder).

Linear polarization was used to determine that the apparent corrosion rate of this SAM2X5 coating was approximately 81.1 μm/yr in SAW at 90°C after 133 days immersion with the sample shown in Figure 36. Despite the relatively high electrochemical activity, which is reflected in the high apparent corrosion rate as determined with linear polarization, there is no visible evidence of corrosion in this case, and the sample was in pristine condition after this exposure. The epoxy used to mask the hemispherical tip of the rod, and to seal the insulating sheath turned black in color during the test (right-hand end of cylinder).

H. Corrosion Rates – Based on Weight-Loss & Dimensional Measurements

Weight and dimensional measurements of SAM2X5-coated standard crevice-corrosion samples, before and after long-term immersion testing in seven environments, are summarized in Table X. These SAM2X5 coatings were produced with powder lot 06-015, and deposited on the nickel-based Alloy C-22 substrates with the high-velocity oxy-fuel (HVOF) process, using hydrogen as the fuel.

Weight and dimensional measurements of SAM2X5-coated standard weight-loss samples, before and after long-term immersion testing in seven environments, are summarized Table XI. These SAM2X5 coatings were produced with powder lot 06-015, and deposited on the nickel-based Alloy C-22 substrates with the high-velocity oxy-fuel (HVOF) process, using hydrogen as the fuel.

Corrosion rates calculated from the weight and dimensional measurements of SAM2X5-coated crevice-corrosion samples are summarized in Table XII, along with the final values of corrosion rate determined with linear polarization. The corrosion rates based on weight loss were calculated with two possible values of the SAM2X5 density: Basis 1 used the density values calculated from the weights and dimensions of the applied coatings, which may indicate that these coatings were not fully dense; Basis 2 used the density for the fully-dense alloy.

Corrosion rates calculated from the weight and dimensional measurements of SAM2X5-coated weight-loss samples are summarized in Table XIII, along with the final values of corrosion rate determined with linear polarization. The corrosion rates based on weight loss were calculated with two possible values of the SAM2X5 density: Basis 1 used the density values calculated from the weights and dimensions of the applied coatings, which may indicate that these coatings were not fully dense; Basis 2 used the density for the fully-dense alloy.

After 135 days immersion, weight loss and dimensional measurements were used to determine the corrosion rates of SAM2X5 coatings on *Alloy C-22 weight-loss samples*, as shown in Figure 37. Depending upon the assumed coating density, these rates were determined to be: (1) 14.3-15.9 μm/yr in natural seawater at 90°C; (2) 8.4-9.3 μm/yr in 3.5-molal NaCl solution at 30°C; (3) 26.1-29.7 μm/yr in 3.5-molal NaCl solution at 90°C; (4) 4.6-5.1 μm/yr in 3.5-molal NaCl and 0.525-molal KNO_3 solution at 90°C; (5) 8.3-9.4 μm/yr in SDW at 90°C; (6) 2.8-3.0 μm/yr in SCW at 90°C; and (7) 16.5-18.1 μm/yr in SAW at 90°C. In the case of 3.5-molal NaCl solution at 90°C, the electrochemical measurement over predicted the actual corrosion rate determined with weight loss and dimensional measurements by a factor of about six (×6). In the case of SAW at 90°C, the electrochemical measurement also over predicted the actual corrosion rate determined with weight loss and dimensional measurements, this time by a factor of about five (×5). While electrochemical measurements such as linear polarization could be used to determine qualitative trends in corrosion rates during these long-term immersion tests, absolute values in the most aggressive electrolytes were over predicted by a factor of five-to-six (×5 to ×6). In contrast, the corrosion rates determined with linear polarization proved to be non-conservative in

the more benign electrolytes, and under predicted the actual corrosion rates by a factor of about two-to-three (×2 to ×3). Linear polarization is a beneficial method for determining qualitative trends in corrosion rate in real time, but cannot measure corrosion rates accurately enough for reliable long-term prediction.

After 135 days immersion, weight loss and dimensional measurements were used to determine the corrosion rates of SAM2X5 coatings on Alloy C-22 crevice-corrosion samples, as shown in Figure 38. Depending upon the assumed coating density, these rates were determined to be: (1) 14.7-17.3 μm/yr in natural seawater at 90°C; (2) 8.8-9.9 μm/yr in 3.5-molal NaCl solution at 30°C; (3) 28.8-32.5 μm/yr in 3.5-molal NaCl solution at 90°C; (4) 4.2-4.3 μm/yr in 3.5-molal NaCl and 0.525-molal KNO_3 solution at 90°C; (5) 8.2-9.5 μm/yr in SDW at 90°C; (6) 2.7-3.2 μm/yr in SCW at 90°C; and (7) 19.7-22.5 μm/yr in SAW at 90°C. In the case of 3.5-molal NaCl solution at 90°C, the electrochemical measurement over predicted the actual corrosion rate determined with weight loss and dimensional measurements by a factor of about six (×6). In the case of SAW at 90°C, the electrochemical measurement also over predicted the actual corrosion rate determined with weight loss and dimensional measurements, this time by a factor of about five (×5). While electrochemical measurements such as linear polarization could be used to determine qualitative trends in corrosion rates during these long-term immersion tests, absolute values in the most aggressive electrolytes were over predicted by a factor of five-to-six (×5 to ×6). In contrast, the corrosion rates determined with linear polarization proved to be non-conservative in the more benign electrolytes, and under predicted the actual corrosion rates by a factor of about two-to-three (×2 to ×3). Linear polarization is a beneficial method for determining qualitative trends in corrosion rate in real time, but cannot measure corrosion rates accurately enough for reliable long-term prediction.

As shown in Figure 39, corrosion rates of the weight-loss samples (no holes) were determined to be 14.3-15.9 μm/yr in natural seawater at 90°C; corrosion rates of the crevice-corrosion samples (with bolt holes) were determined to be 14.7-17.3 μm/yr. These samples, , identified as C22-W1, C22-W2, C22-C1 and C22-C2, showed reddish-brown corrosion products on the surface of the coating due to corrosion. There is a scalloped crevice corrosion pattern on both the SAM2X5-coated front side of the crevice samples, as well as on the Alloy C-22 back side of the crevice samples. There was also some corrosion on the edge of the samples, at the coating-substrate interface.

As shown in Figure 40, corrosion rates of the weight-loss samples (no holes) were determined to be 8.4-9.3 μm/yr in 3.5-molal NaCl solution at 30°C; corrosion rates of the crevice-corrosion samples (with bolt holes) were determined to be 8.8-9.9 μm/yr. These samples, identified as C22-W3, C22-W4, C22-C3 and C22-C4, showed had reddish-brown stain on the surface, with some sparse pitting corrosion.

As shown in Figure 41, corrosion rates of the weight-loss samples (no holes) were determined to be 26.1-29.7 μm/yr in 3.5-molal NaCl solution at 90°C; corrosion rates of the crevice-corrosion samples (with bolt holes) were determined to be 28.8-32.5 μm/yr. In contrast to the samples tested at 30°C, these samples had heavier reddish-brown stain, and heavier pitting corrosion.

As shown in Figure 42, corrosion rates of the weight-loss samples (no holes) were determined to be 4.6-5.1 μm/yr in 3.5-molal NaCl and 0.525-molal KNO_3 solution at 90°C; corrosion rates of the crevice-corrosion samples (with bolt holes) were determined to be 4.2-4.3 μm/yr. These samples, identified as C22-W7, C22-W8, C22-C7 and C22-C8. The weight-loss samples showed

reddish-brown stain on the surface, while the crevice-corrosion samples showed sparse pitting corrosion around the perimeter of the samples.

As shown in Figure 43, corrosion rates of the weight-loss samples (no holes) were determined to be 8.3-9.4 μm/yr in SDW at 90°C; corrosion rates of the crevice-corrosion samples (with bolt holes) were determined to be 8.2-9.5 μm/yr in SDW. These samples, identified as C22-W9, C22-W10, C22-C9 and C22-C10. These samples had showed slight discoloration, but no significant corrosion.

As shown in Figure 44, corrosion rates of the weight-loss samples (no holes) were determined to be 2.8-3.0 μm/yr in SCW at 90°C; corrosion rates of the crevice-corrosion samples (with bolt holes) were determined to be 2.7-3.2 μm/yr. These samples, identified as C22-W11, C22-W12, C22-C11 and C22-C12 showed slight discoloration, but no significant corrosion.

As shown in Figure 45, corrosion rates of the weight-loss samples (no holes) were determined to be 16.5-18.1 μm/yr in SAW at 90°C; corrosion rates of the crevice-corrosion samples (with bolt holes) were determined to be 19.7-22.5 μm/yr. These samples, identified as C22-W13, C22-W14, C22-C13 and C22-C14 showed slight discoloration, but no significant corrosion. An area stained with corrosion product was observed neat the bolt hole in crevice sample C22-13. An array of cracks is observed in the center of the weight-loss samples, with corrosion products inside the crack. Since this type of cracking was only observed with electrolytes having acidic pH, it is believed that this cracking may be due to the coating's absorption of hydrogen near the cracks. The galvanic coupling of the anodic oxidation of metal within the crack could drive cathodic hydrogen reduction near the cracks. The cracking observed in low-pH weight loss samples could therefore be due to hydrogen-induced cracking.

IV. DISCUSSION

It has been recognized that the corrosion resistance of both iron- and nickel based crystalline alloys can be enhanced through the additions of Cr, Mo and W for many years.[39-40] These alloying elements are also enhance the corrosion resistance of iron-based amorphous metals. While the pitting resistance equivalence number (PREN) was developed for crystalline alloys, it was effectively used as a general guidance in determining maximum beneficial elemental concentrations of Cr, Mo and W used in the materials studied here.[41-46] Initial calculations of the PREN for these amorphous alloys were done using formulae from the published literature.[45]

As pointed out in the literature, an estimate of the relative pitting resistance of alloys can be made using the pitting resistance equivalence number (PREN), which is calculated using the elemental composition of the alloy. The calculated PREN values for the nickel-based reference alloys and the Fe-based amorphous metals discussed here are presented in Table XIV, to serve as the basis of this discussion. For example, one possible equation used for estimating the PREN for nickel-based alloys is: [47]

$$PREN = [\%Cr] + 1.5 \times ([\%Mo] + [\%W] + [\%Nb]) \tag{8}$$

Another equation used for estimating the PREN of austenitic and duplex stainless steels is: [48]

$$PREN = [\%Cr] + 3.3 \times ([\%Mo] + 0.5 \times [\%W]) + 16 \times [\%N] \tag{9}$$

Based on these equations, it was concluded that the resistance of the SAM2X5 and SAM1651 amorphous metal formulations should be more resistant to localized corrosion than Type 316L

stainless steel or Ni-based Alloy C-22. As in the case of crystalline Fe-based and Ni-based alloys, it was found experimentally that the addition of Cr, Mo, and W substantially increased the corrosion resistance of these amorphous alloys. However, there was additional passive film stability, which could not be attributed to composition alone, and may be attributable to the glassy structure. Additional work is required to further understand the relative roles of composition and crystalline structure in high-performance amorphous metal coatings, such as the ones discussed here.

The effect of powder size on the corrosion performance of Fe-based amorphous metal coatings was studied. Coatings produced with relatively large (-53/+30 micron) powders may have surface features more like fully dense, melt spun ribbons than did coatings produced with finer (+30/+15 micron) powders. In potential-step experiments with the application of 900, 1000, 1100, 1200, 1300 and 1400 mV vs. OCP, the passive film on coatings produced with fine (+30/+15 micron) powders exhibited current density transients, which indicated periodic losses of passivity, with intervening periods of repassivation. Such transient were not observed with coatings prepared with coarser (-53/+30 micron) powders. The passive film on nickel-based Alloy C-22 started to destabilize at 900 mV vs. OCP, whereas passive film stability on melt-spun ribbons of SAM2X5 was maintained at an applied potential of 1500 mV vs. OCP, and lost at 1600 mV vs. OCP. In the case of the thermal spray coatings of SAM2X5 produced with relatively coarse powder, the passive film maintained stability at 1400 mV vs. OCP, but lost stability at 1500 mV vs. OCP. In the case of the thermal spray coatings of SAM2X5 produced with the finer powder, the onset of passive film de-stabilization was observed at 900 mV vs. OCP.

The passive film stability observed with coatings produced with finer particles could be due to any number of phenomena, and deserves further investigation in the future. For example, residual porosity in the coatings might behave like the occluded regions of a pit or crevice, with lowered pH due to the combined effects of differential aeration, anion transport into the pores, and hydrolysis reactions involving dissolved metal species within the pores, with the production of hydrogen ions. Furthermore, these finer particles may generate a surface topography within pores, with a smaller radius of curvature, which could alter the surface free energy due to the Kelvin effect. The oxide film covering these occluded surfaces could be more highly defected.

V. CONCLUSIONS

An iron-based amorphous metal, $Fe_{49.7}Cr_{17.7}Mn_{1.9}Mo_{7.4}W_{1.6}B_{15.2}C_{3.8}Si_{2.4}$ (SAM2X5), with very good corrosion resistance was developed. This material was produced as a melt-spun ribbon, as well as gas atomized powder and a thermal-spray coating. Chromium (Cr), molybdenum (Mo) and tungsten (W) provided corrosion resistance, and boron (B) enabled glass formation. The high boron content of this particular amorphous metal made it an effective neutron absorber, and suitable for criticality control applications. Earlier studies have shown that ingots and melt-spun ribbons of these materials have good passive film stability in these environments. Thermal spray coatings of these materials have now been produced, and have undergone a variety of corrosion testing, including both atomospheric and long-term immersion testing. The modes and rates of corrosion have been determined in the various environments, and are reported here.

ACKNOWLEDGMENTS

This work was performed by Lawrence Livermore National Laboratory under Contract Number W-7405-Eng-48 and under the auspices of the United States Department of Energy. Work was co-sponsored by the Office of Civilian and Radioactive Waste Management (OCRWM) of the United States Department of Energy (DOE), and the Defense Science Office (DSO) of the Defense Advanced Research Projects Agency (DARPA). The guidance of Jeffrey Walker at DOE OCRWM and Leo Christodoulou at DARPA DSO is gratefully acknowledged. The preparation of thermal spray coatings by Plasma Technology Incorporated (PTI) in Torrence, California, under the direction of Andy D'Amato is gratefully acknowledged. Salt fog testing by E-Labs in Fredericksburg, Virginia, under the direction of Ken Maloy, is also gratefully acknowledged. Thermal analyses of the amorphous metals, quoted in the paper, are attributed to John Perepezko and his research group at the University of Wisconsin, Madison (UWM). Neutron transmission measurements, used as the basis of neutron absorption cross-sections, were made by the University of California's McClellan Nuclear Radiation Center (MNRC). Measurements made by PTI, E-Labs, UWM, and MNRC were made under contract to LLNL.

REFERENCES

1. M. Telford: The case for bulk metallic glass. *Materials Today*, **3,** 36-43 (2004).
2. N. R. Sorensen and R. B. Diegle: Corrosion of amorphous metals. In *Corrosion, Metals Handbook*, 9th Ed., Vol. 13, edited by J. R. Davis and J. D. Destefani (American Society of Metals International, Metals Park, OH, 1987), pp. 864-870.
3. R. M. Latanison: Corrosion resistance of metastable alloys processed by rapid solidification. *Workshop on Amorphous Metals and Semiconductors*, May 12-18, 1985 (Electric Power Research Institute, 1985).
4. D. E. Polk and B. C. Giessen: Overview of principles and applications. Chapter 1, In *Metallic Glasses*, edited by J. J. Gilman and H. J. Leamy (American Society of Metals International, Metals Park, OH, 1978), pp. 2-35.
5. K. Kishitake, H. Era, and F. Otsubo: Characterization of plasma sprayed Fe-10Cr-10Mo-(C,B) amorphous coatings. *J. Thermal Spray Technology*, **5** (2), 145-153 (1996).
6. S. Pang, T. Zhang, K. Asami, and A. Inoue: Effects of chromium on the glass formation and corrosion behavior of bulk glassy Fe-Cr-Mo-C-B alloys. *Materials Transactions*, **43** (8), 2137-2142 (2002).
7. S. J. Pang, T. Zhang, K. Asami, and A. Inoue: Synthesis of Fe-Cr-Mo-C-B-P bulk metallic glasses with high corrosion resistance. *Acta Materialia*, **50**, 489-497 (2002).
8. F. Guo, S. J. Poon, and G. J. Shiflet: Metallic glass ingots based on yttrium. *Metallic Applied Physics Letters*, **83** (13), 2575-2577 (2003).
9. Z. P. Lu, C. T. Liu, and W. D. Porter: Role of yttrium in glass formation of Fe-based bulk metallic glasses. *Metallic Applied Physics Letters*, **83** (13), 2581-2583 (2003).
10. V. Ponnambalam, S. J. Poon, and G. Shiflet: *J. Materials Research*, **19** (5), 1320, 2004.
11. J. C. Farmer, J. J. Haslam, S. D. Day, D. J. Branagan, C. A. Blue, J. D. K. Rivard, L. F. Aprigliano, N. Yang, J. H. Perepezko, and M. B. Beardsley: Paper PVP2005-71664, Pressure Vessels and Piping Division Conference, Denver, CO, July 17-21, 2005 (American Society of Mechanical Engineers, Three Park Avenue, New York, NY, 2005).

12. J. C. Farmer, J. J. Haslam, S. D. Day, T. Lian, R. Rebak, N. Yang, and L. Aprigliano: Corrosion resistance of iron-based amorphous metal coatings. Paper PVP2006-ICPVT11-93835, *Pressure Vessels and Piping Division Conference*, Vancouver, BC, July 23-27, 2006 (American Society of Mechanical Engineers, Three Park Avenue, New York, NY, 2006).
13. H. Shinimiya, A. Nakazawa, Z. Kato, A. A. El Moneium, Y. Niizeki, K. Asami, and K. Hashimoto: Corrosion resistant bulk amorphous Ni-Cr-Ta-Mo-Nb-5P alloys in concentrated hydrochloric acids. Paper 319, *Session on Corrosion and Electrochemistry of Advanced Materials in Honor of Koji Hashimoto*, 208th Meeting of the Electrochemical Society, Westing Bonaventure Hotel, Los Angeles, California, October 16-21, 2005 (Electrochemical Society, Pennington, NJ, 2005).
14. D. Chidambaram, C. R. Clayton, and M. R. Dorfman: Evaluation of the electrochemical behavior of HVOF-sprayed alloy coatings. *Surface and Coatings Technology*, **176**, 307-317 (2004).
15. D. J. Branagan, Method of modifying iron-based glasses to increase crystallization temperature without changing melting temperature. U.S. Patent Application No. 20040250929, Filed Dec. 16, 2004.
16. D. J. Branagan: Properties of amorphous/partially crystalline coatings. U.S. Patent Application No. 20040253381, Filed Dec. 16, 2004.
17. J. Farmer, J. Haslam, S. Day, T. Lian, C. Saw, P. Hailey, J-S. Choi, R. Rebak, N. Yang, R. Bayles, L. Aprigliano, J. Payer, J. Perepezko, K. Hildal, E. Lavernia, L. Ajdelsztajn, D. J. Branagan, and M. B. Beardsely: A high-performance corrosion-resistant iron-based amorphous metal – the effects of composition, structure and environment on corrosion resistance. *Scientific Basis for Nuclear Waste Management XXX*, Symposium NN, Boston, MA, Nov. 27 – Dec. 1, 2006 (Materials Research Society, 2006).
18. T. Lian, D. Day, P. Hailey, J-S. Choi, and J. Farmer: Comparative study on the corrosion resistance of Fe-based amorphous metal, borated stainless steel and Ni-Cr-Mo-Gd alloy. Scientific Basis for Nuclear Waste Management XXX, Symposium NN, Boston, MA, Nov. 27 – Dec. 1, 2006 (Materials Research Society, 2006).
19. J-S. Choi, C. Lee, J. Farmer, D. Day, M. Wall, C. Saw, M. Boussoufi, B. Liu, H. Egbert, D. Branagan, and A. D'Amato: Application of neutron-absorbing structural amorphous metal coatings for spent nuclear fuel container to enhance criticality safety controls. Scientific Basis for Nuclear Waste Management XXX, Symposium NN, Boston, MA, Nov. 27 – Dec. 1, 2006 (Materials Research Society, 2006).
20. C. K. Saw: In *X-ray Scattering Techniques for Characterization Tools in the Life Sciences, Nanotechnologies for the Life Science*, edited by Challa Kumar (Wiley-VCH Verlag GmbH and Company, KGaA, Weinheim, 2006).
21. C. K. Saw and R. B. Schwarz: Chemical short-range order in dense random-packed models. *J. Less-Common Metals*, **140**, 385-393 (1988).
22. Harrar, J.E.; Carley, J.F.; Isherwood, W.F.; and Raber, E. 1990. *Report of the Committee to Review the Use of J-13 Well Water in Nevada Nuclear Waste Storage Investigations*, Yucca Mountain Project, Lawrence Livermore National Laboratory, Livermore, CA, UCID-21867, 111 p.
23. Gdowski, G.E. 1991. "Survey of Degradation Modes of Four Nickel-Chromium-Molybdenum Alloys," UCRL-ID-108330, Lawrence Livermore National Laboratory, Livermore, CA, pp. 30–31, Tables 22 and 23.

24. Gdowski, G.E. 1997a. "Formulation and Make-up of Simulated Dilute Water (SDW), Low Ionic Content Aqueous Solution," Yucca Mountain Project, Lawrence Livermore National Laboratory, Livermore, CA, TIP-CM-06, Revision CN TIP-CM-06-0-2, Table 1, p. 3.
25. Gdowski, G.E. 1997b. "Formulation and Make-up of Simulated Concentrated Water (SCW), High Ionic Content Aqueous Solution," Yucca Mountain Project, Lawrence Livermore National Laboratory, Livermore, CA, TIP-CM-07, Revision CN TIP-CM-07-0-2, Table 1, pp. 3–4.
26. Gdowski, G.E. 1997c. "Formulation and Make-up of Simulated Acidic Concentrated Water (SAW), High Ionic Content Aqueous Solution," Yucca Mountain Project, Lawrence Livermore National Laboratory, Livermore, CA, TIP-CM-08, Revision CN TIP-CM-08-0-2, Table 1, p. 3.
27. Wang, F. 1999. "Summary on the Modification of BSW Solutions for SCC Tests." Memorandum, LLNL.
28. CRWMS M&O, *Input Transmittal for Environment on the Surface of Drip Shield and Waste Package Outer Barrier*, Civilian Radioactive Waste Management System Management and Operating Contractor (CRWMS M&O), AP-3.14Q Input Tracking Number WP-LNL-00017T, Las Vegas, Nevada, 2000.
29. J. Farmer, S. Lu, D. McCright, G. Gdowski, F. Wang, T. Summers, P. Bedrossian, J. Horn, T. Lian, J. Estill, A. Lingenfelter, and W. Halsey: General and localized corrosion of high-level waste container in Yucca Mountain. Pressure Vessel and Piping Conference, Seattle, WA, July 23-27, 2000, In *Transportation, Storage, and Disposal of Radioactive Materials*, PVP Vol. 408 (American Society of Mechanical Engineers, Three Park Avenue, New York, NY, 2000), pp. 53-70.
30. J. R. Scully, J. L. Hudson, T. Lunt, G. Ilevbare, and B. Kehler: Localized corrosion initiation and transition to stabilization in alloys 625 and C-22. Final Report, TRW/DOE Yucca Mountain Project Purchase Order No. A10762JM8A (University of Virginia, Charlottesville, VA, Sep. 30, 1999).
31. K. A. Gruss, G. A. Cragnolino, D. S. Dunn, and N. Sridar: Repassivation potential for localized corrosion of alloys 625 and C22 in simulated repository environments. Paper 149, Corrosion 98 (National Association of Corrosion Engineers, Houston, TX, 1998).
32. Standard reference test method for making potentiostatic and potentiodynamic anodic polarization measurements. Designation G 5-94, In *1997 Annual Book of American Society for Testing and Materials Standards,* Section 3, Vol. 3.02 (American Society for Testing and Materials, 1997), pp. 54–57.
33. Standard reference test method for making potentiostatic and potentiodynamic anodic polarization measurements. Designation G 5-87, In *1989 Annual Book of American Society for Testing and Materials Standards*, Section 3, Vol. 3.02 (American Society for Testing and Materials, 1989), pp. 79–85.
34. Standard practice for conventions applicable to electrochemical measurements in corrosion testing. Designation G 3-89, In *1997 Annual Book of American Society for Testing and Materials Standards*, Section 3, Vol. 3.02, (American Society for Testing and Materials, 1997), pp. 36–44.
35. Standard test method for conducting cyclic potentiodynamic polarization measurements for localized corrosion susceptibility of iron-, nickel-, or cobalt-based alloys. Designation G 61-86, In 1997 Annual Book of American Society for Testing and Materials Standards, Section 3, Vol. 3.02 (American Society for Testing and Materials, 1997), pp. 231–235.

36. R. S. Treseder, R. Baboian, and C. G. Munger: Polarization resistance method for determining corrosion rates. In *Corrosion Engineer's Reference Book*, 2nd Ed. (National Association of Corrosion Engineers, Houston, TX, 1991), pp. 65-66.
37. D. A. Jones: Electrochemical kinetics of corrosion – Faraday's law. In *Principles and Prevention of Corrosion*, 2nd Ed., Chapter 3, Section 3.1.1, Equations 3-5 (Prentice Hall, Upper Saddle River, NJ, 1996), pp. 75–76.
38. A. J. Bard and L. R. Faulkner: Potentials and thermodynamics of cells – liquid junction potentials. In *Electrochemical Methods, Fundamentals and Applications*, Chapter 2, Section 2.3, Table 2.3.2, Equation 2.3.39 (John Wiley and Sons, New York, NY, 1980), p. 67, 71.
39. H. P. Hack: Crevice corrosion behavior of molybdenum-containing stainless steel in seawater. *Materials Performance*, **22** (6) 24–30 (1983).
40. A. I. Asphahani: Corrosion resistance of high performance alloys. *Materials Performance*, **19** (12) 33–43 (1980).
41. J. C. Farmer et al.: High-performance corrosion-resistant amorphous metals. *Global 2003*, New Orleans, LA, 2003 (American Nuclear Society, 2003).
42. D. J. Branagan, M. C. Marshall, and B. E. Meacham: High performance corrosion resistant materials for naval warfighting and safe long-term storage/disposal of spent nuclear fuel. *Final Report*, LLNL Subcontract, LLNL-RFP-B550033 (Institute of Nanomaterials Research and Development, The NanoSteel Company, Idaho Falls, ID, 2005) 84 pages.
43. J. Farmer, C. Earl, C. Doty, D. Spence, J. Walker, F. Wong, J. Payer, G-Q. Lu, D. E. Clark, D. C. Folz, A. Heuer, O. Graeve, D. Branagan, C. Blue, J. Rivard, J. Perepezko, L. Kaufman, N. Yang, E. Lavernia, J. Haslam, E. Lemieux, L. Aprigliano, B. Beardsley, T. Weaver, B. Edwards, B. Brown, A. Halter, B Bayles and J. Lewandowski: *DARPA-DOE High Performance Corrosion-Resistant Materials Principal Investigator's Meeting*, Turtle Bay Resort, Oahu, Hawaii, January 10-13, 2005, UCRL-PRES-214672 (Lawrence Livermore National Laboratory, Livermore, CA, 2005), 407 pages.
44. J. C. Farmer, J. J. Haslam and S. D. Day: High-performance corrosion-resistant iron-based amorphous-metal coatings – evaluation of corrosion resistance. *HPCRM Annual Report*, UCRL-SR-218144 (Lawrence Livermore National Laboratory, Livermore, CA, 2006), 68 pages.
45. J. C. Farmer, J-S. Choi, J. J. Haslam, S. D. Day, N. Yang, T. Headley, G. Lucadamo, J. L Yio, J. Chames, A. Gardea, M. Clift, C. A. Blue, W. H. Peters, J. D. K. Rivard, D. C. Harper, D. Swank, R. Bayles & E. J. Lemieux, Robert Brown & Theresa M. Wolejsza, L. F. Aprigliano, D. J. Branagan, M. C. Marshall, Brian E. Meacham, E. Joseph Buffa, M. Brad Beardsley, E. J. Lavernia, J. Schoenung, L. Ajdelsztajn, J. Dannenberg, O. A. Graeve, J. J. Lewandowski, John H. Perepezko, Kjetil Hildal, L. P. Kaufman, J. Boudreau: High-performance corrosion-resistant iron-based amorphous metal coatings. *Team FY05 HPCRM Annual Report*, UCRL-SR-219257 (Lawrence Livermore National Laboratory, Livermore, CA, 2006), 138 pages.
46. J. Farmer, J. Haslam, S. Day, T. Lian, C. Saw, P. Hailey, J-S. Choi, N. Yang, C. Blue, W. Peter, R. Bayles, R. Brown, J. Payer, J. Perepezko, K. Hildal, E. Lavernia, L. Ajdelsztajn, D. J. Branagan, J. Buffa, M. Beardsley, L. Aprigliano and J. Boudreau: Corrosion resistance of iron-based amorphous metals in hot concentrated calcium chloride and seawater: $Fe_{48}Mo_{714}Cr_{15}Y_2C_{15}B_6$. UCRL-TM-224159 (Lawrence Livermore National Laboratory, Livermore, CA, Aug. 30, 2006), 47 pages.

47. C. Thornton and C. Cooper: Overmatching superalloy consumable Inco-weld, 686CPT broadens its applications to include welding super austenitic and super duplex stainless steels, In *Stainless Steel World* (KCI Publishing BV 1, 2004).
48. Pitting corrosion. (www.corrosion-doctors.org/localized/pitting.htm, Dec. 23, 2006).

TABLES

Table I– Neutron absorption cross-sections for HVOF coating of Alloy C-22.

Plate ID	Transmission Cross Section Σ_t (cm^{-1})
Type 316L Stainless Steel	**1.07**
Nickel-Based Alloy C-22	**1.29**
Borated Stainless Steel (182193)	1.67
Borated Stainless Steel (182194)	2.21
Borated Stainless Steel (182196)	2.6
Borated Stainless Steel (03180)	2.65
Borated Stainless Steel Average	**2.28**
Borated Stainless Steel Standard Deviation	**0.45**
Ni-Cr-Mo-Gd (NiGd)	3.77
Ni-Cr-Mo-Gd (NiGd)	3.79
Ni-Cr-Mo-Gd (NiGd)	3.91
Ni-Cr-Mo-Gd (NiGd)	3.89
Ni-Cr-Mo-Gd (NiGd) Average	**3.84**
Ni-Cr-Mo-Gd (NiGd) Standard Deviation	**0.07**
HVOF SAM2X5 with Powder Lot # 05-079 (M18W3)	6.52
HVOF SAM2X5 with Powder Lot # 05-079 (M10S14)	7.65
HVOF SAM2X5 with Powder Lot # 06-015 (316LC1)	5.82
HVOF SAM2X5 with Powder Lot # 06-015 (316LC2)	6.73
HVOF SAM2X5 with Powder Lot # 06-015 (316LW1)	7.18
HVOF SAM2X5 with Powder Lot # 06-015 (316LW2)	7.01
HVOF SAM2X5 with Powder Lot # 06-015 (C22C15)	6.34
HVOF SAM2X5 with Powder Lot # 06-015 (C22C16)	8.3
HVOF SAM2X5 with Powder Lot # 06-015 (C22W15)	8.37
HVOF SAM2X5 with Powder Lot # 06-015 (C22W16)	7.43
HVOF SAM2X5 Average	**7.14**
HVOF SAM2X5 Standard Deviation	**0.83**
Metamic Al + B_4C	16.9
Boral Al + B_4C	22.7
Al + B_4C Average	**19.80**

Table II – A description of the standard GM9540P Salt Fog Test is summarized here. Note that the salt solution mists (denoted with asterisks) consisted of 1.25% solution containing 0.9% sodium chloride, 0.1% calcium chloride, and 0.25% sodium bicarbonate.

24-Hour Test Cycle for GM9540P Accelerated Corrosion Test		
Shift	Elapsed Time (hrs)	Event
Ambient Soak	0	Salt solution mist for 30 seconds, followed by ambient exposure at 13-28°C (55-82°F)
	1.5	Salt solution mist for 30 seconds, followed by ambient exposure at 13-28°C (55-82°F)
	3	Salt solution mist for 30 seconds, followed by ambient exposure at 13-28°C (55-82°F)
	4.5	Salt solution mist for 30 seconds, followed by ambient exposure at 13-28°C (55-82°F)
Wet Soak	8 to 16	High humidity exposure for 8 hours at 49 ± 0.5°C (120 ± 1°F) and 100% RH, including a 55-minute ramp to wet conditions
Dry Soak	16 to 24	Elevated dry exposure for 8 hours at 60 ± 0.5°C (140 ± 1°F) and less than 30% RH, including a 175-minute ramp to dry conditions

Table III – Composition of Standard Test Media Based Upon J-13 Well Water

Ion	SDW	SCW	SAW	SSW
	(mg/L^{-1})	(mg/L^{-1})	(mg/L^{-1})	(mg/L^{-1})
K^{+1}	34	3,400	3,400	141,600
Na^{+1}	409	40,900	40,900	48,700
Mg^{+2}	1	1	1,000	0
Ca^{+2}	1	1	1,000	0
F^{-1}	14	1,400	0	0
Cl^{-1}	67	6,700	6,700	128,400
NO_3^{-1}	64	6,400	6,400	1,310,000
SO_4^{-2}	167	16,700	16,700	0
HCO_3^{-1}	947	70,000	0	0
Si (60°C)	27	27	27	0
Si (90°C)	49	49	49	0
pH	8.1	8.1	2.7	7.0

Table IV – Initial BSW Solution Recipe (Wang 1999)

Chemical	Quantity (g)
Na_2CO_3 (anhydrous)	10.6
KCl	9.7
NaCl	8.8
NaF	0.2
$NaNO_3$	13.6
Na_2SO_4 (anhydrous)	1.4
H_2O	55.7
pH	11.3 (measured at room temperature)

Table V – The melt-spinning process was used to perform a systematic study of various elemental compositions, each based on the Fe-based DAR40 composition, with 1, 3, 5, and 7 atomic percent additions of specific elements believed to be beneficial to glass formation or corrosion resistance. Elemental additions investigated included nickel (Ni), molybdenum (Mo), yttrium (Y), titanium (Ti), zirconium (Zr) and chromium (Cr). The two formulations of greatest interest at the present time, based upon corrosion resistance and ease of processing are SAM2X5 ($Fe_{49.7}Cr_{17.7}Mn_{1.9}Mo_{7.4}W_{1.6}B_{15.2}C_{3.8}Si_{2.4}$), which has a relatively high CCR, and yttrium-containing SAM1651 ($Fe_{48.0}Cr_{15.0}Mo_{14.0}B_{6.0}C_{15.0}Y_{2.0}$), which has a relatively low CCR.

Target Compositions in Atomic Percent - Used to Prepare Samples														
Alloy	Specification / Formula	Fe	Cr	Mn	Mo	W	B*	C*	Si	Y	Ni	P*	Co	Total
Type 316L	UNS S31603	68.0	18.0	1.5	1.5	0.0	0.0	0.0	1.0	0.0	10.0	0.0	0.0	100
Alloy C-22	UNS N06022	4.0	25.0	0.1	8.0	1.4	0.0	0.0	1.0	0.0	60.0	0.0	0.5	100
SAM40	$Fe_{52.3}Mn_2Cr_{19}Mo_{2.5}W_{1.7}B_{16}C_4Si_{2.5}$	52.3	19.0	2.0	2.5	1.7	16.0	4.0	2.5	0.0	0.0	0.0	0.0	100
SAM2X1	$(SAM40)_{99} + Mo_1$	51.8	18.8	2.0	3.5	1.7	15.8	4.0	2.5	0.0	0.0	0.0	0.0	100
SAM2X3	$(SAM40)_{97} + Mo_3$	50.7	18.4	1.9	5.4	1.6	15.5	3.9	2.4	0.0	0.0	0.0	0.0	100
SAM2X5	$(SAM40)_{95} + Mo_5$	49.7	18.1	1.9	7.4	1.6	15.2	3.8	2.4	0.0	0.0	0.0	0.0	100
SAM2X7	$(SAM40)_{93} + Mo_7$	48.6	17.7	1.9	9.3	1.6	14.9	3.7	2.3	0.0	0.0	0.0	0.0	100

Table VI – The concentrations of heavy elements used in samples of Type 316L stainless steel, Alloy C-22, SAM40, SAM2X1, SAM2X3, SAM2X5, SAM2X7 and SAM1651 used in this study were verified with energy dispersive X-ray spectroscopy (EDS). Data for melt-spun ribbons of SAM2X40, SAM40, SAM2X1, SAM2X3, SAM2X5 and SAM2X7 and a drop-cast ingot of SAM1651 are presented in this table.

Actual Compositions in Atomic Percent - Determined by Energy Dispersive X-Ray Spectroscopy														
Alloy	Sample	Fe	Cr	Mn	Mo	W	B*	C*	Si	Y	Ni	P*	Co	Total
Type 316L	MSR	67.6	18.7	1.3	1.2	0.0	0.0	0.0	1.2	0.0	10.0	0.0	0.0	100
Alloy C-22	MSR	3.9	25.2	0.1	7.8	1.4	0.0	0.0	1.1	0.0	60.0	0.0	0.5	100
SAM40	MSR	51.9	19.2	2.6	2.5	1.5	16.0	4.0	2.2	0.0	0.0	0.0	0.0	100
SAM2X1	MSR	52.0	19.1	2.7	2.9	1.6	15.8	4.0	1.9	0.0	0.0	0.0	0.0	100
SAM2X3	MSR	49.3	17.9	2.6	5.3	2.5	15.5	3.8	3.1	0.0	0.0	0.0	0.0	100
SAM2X5	MSR	48.8	17.6	2.4	7.2	2.5	15.0	3.7	2.7	0.0	0.0	0.0	0.0	100
SAM2X7	MSR	46.9	16.9	2.3	10.0	2.5	14.9	3.7	2.9	0.0	0.0	0.0	0.0	100

* The concentrations of relatively light elements such as B and C could not be determined with EDS, and were therefore estimated with a simple difference calculation, so that the sum of concentrations for all elements totaled one hundred percent.

Table VII – Thermal analysis data (DTA or DSC) for Fe-based glass forming alloys suitable for thermal spray deposition as summarized in this table. The two formulations of greatest interest at the present time are SAM2X5 ($Fe_{49.7}Cr_{17.7}Mn_{1.9}Mo_{7.4}W_{1.6}B_{15.2}C_{3.8}Si_{2.4}$), which has a relatively high CCR, and yttrium-containing SAM1651 ($Fe_{48.0}Cr_{15.0}Mo_{14.0}B_{6.0}C_{15.0}Y_{2.0}$), which has a relatively low CCR. These selections are based upon their good corrosion resistance and relative ease or processing.

Alloy	T_g (°C)	T_x (°C)	T_m (°C)	T_L (°C)	T_{rg}
SAM40	568-574	623	1110	1338	0.53
SAM2X1	575	620	1124	1190-1210	0.57
SAM2X3	578	626	1131	1190-1210	0.57
SAM2X5	579	628	1133	1190-1210	0.57
SAM2X7	573	630	1137	1190-1210	0.57

Table VIII – Measurements of the micro-hardness of Fe-based amorphous HVOF coatings.

	Measured Vickers Micro-Hardness (kg mm^{-2})	
Loading Conditions	As-Sprayed HVOF-Coating	Devitrified at 700°C for 10 Minutes
HV100 (100-gram load)	1050-1200	1300-1500
HV300 (300-gram load)	1000-1100	1200-1350

Table IX – The conversion of the corrosion current density to penetration rate (corrosion rate) requires the parameters summarized in this table. These penetration rates are for an assumed current density of one microamp per square centimeter (1 μA cm^{-2}). If the corrosion rate is 2 μA cm^{-2} instead of the assumed 1 μA cm^{-2}, the penetration rate is simply doubled. The value of Faraday's constant (F) is 96,484.6 C $equiv^{-1}$.

Alloy	ρ_{alloy}	$n_{alloy} = (f_j n_j / a_j)/100$		$(dp/dt) = (i_{corr})/(\rho_{alloy} \times n_{alloy} \times F)$			
	g cm^{-3}			cm sec^{-1}		μm $year^{-1}$	
		Low	High	Low	High	Low	High
Type 316L	7.85	3.90×10^{-2}	6.53×10^{-2}	2.02×10^{-11}	3.38×10^{-11}	6.38	10.7
Alloy C-22	8.69	3.80×10^{-2}	6.75×10^{-2}	1.77×10^{-11}	3.14×10^{-11}	5.57	9.89
SAM2X5	7.65	5.41×10^{-2}	7.93×10^{-2}	1.71×10^{-11}	2.50×10^{-11}	5.39	7.89

Table X – Weight and dimensional measurements of SAM2X5-coated standard crevice-corrosion samples, before and after long-term immersion testing in seven environments. These SAM2X5 coatings were produced with powder lot 06-015, and deposited on the nickel-based Alloy C-22 substrates with the high-velocity oxy-fuel (HVOF) process, using hydrogen as the fuel.

Weight & Dimensional Measurements of HVOF SAM2X5 Coatings on Alloy C-22 Crevice Samples																	
Environment	Sample ID	Uncoated				Coated				Tested				Pre-Test Coating Based on Measurements			
		Weight	Thickness	Length	Width	Weight	Thickness	Length	Width	Weight	Thickness	Length	Width	Weight	Thickness	Area	Density
		grams	mm	mm	mm	grams	mm	mm	mm	grams	mm	mm	mm	grams	mm	cm^2	$grams/cm^3$
Seawater 90°C	C22-C1	618.41	7.00	101.67	101.67	642.20	7.35	102.14	101.69	641.77	7.38	102.12	101.70	23.79	0.35	103.86	6.59
Seawater 90°C	C22-C2	627.54	7.09	101.66	101.66	648.67	7.40	104.70	101.66	648.22	7.40	104.72	101.66	21.13	0.31	106.43	6.35
Seawater 90°C	**Average**			**101.67**	**101.67**	**645.43**	**7.37**	**103.42**	**101.67**	**645.00**	**7.39**	**103.42**	**101.68**	**22.46**	**0.33**	**105.14**	**6.47**
3.5 m NaCl 30°C	C22-C3	616.61	6.97	101.67	101.67	637.35	7.27	101.77	101.70	637.09	7.29	101.77	101.68	20.75	0.30	103.50	6.63
3.5 m NaCl 30°C	C22-C4	617.05	6.99	101.67	101.67	637.49	7.27	101.78	101.69	637.23	7.27	101.78	101.68	20.44	0.28	103.49	6.99
3.5 m NaCl 30°C	**Average**			**101.67**	**101.67**	**637.42**	**7.27**	**101.77**	**101.70**	**637.16**	**7.28**	**101.77**	**101.68**	**20.59**	**0.29**	**103.50**	**6.81**
3.5 m NaCl 90°C	C22-C5	617.65	6.99	101.67	101.67	640.32	7.31	101.80	101.68	639.44	7.33	101.80	101.68	22.67	0.32	103.51	6.79
3.5 m NaCl 90°C	C22-C6	616.27	6.97	101.67	101.67	642.10	7.34	101.63	101.65	641.30	7.37	101.66	101.65	25.84	0.37	103.31	6.76
3.5 m NaCl 90°C	**Average**			**101.67**	**101.67**	**641.21**	**7.33**	**101.72**	**101.66**	**640.37**	**7.35**	**101.73**	**101.67**	**24.25**	**0.35**	**103.41**	**6.78**
3.5 m NaCl + 0.525 m KNO_3 90ºC	C22-C7	619.76	7.09	101.67	101.67	650.29	7.43	101.70	101.63	650.15	7.43	101.70	101.67	30.52	0.34	103.35	8.75
3.5 m NaCl + 0.525 m KNO_3 90ºC	C22-C8	612.72	6.93	101.67	101.68	635.89	7.26	101.78	101.65	635.77	7.26	101.78	101.66	23.17	0.33	103.45	6.89
3.5 m NaCl + 0.525 m KNO_3 90ºC	**Average**			**101.67**	**101.67**	**643.09**	**7.34**	**101.74**	**101.64**	**642.96**	**7.35**	**101.74**	**101.66**	**26.85**	**0.33**	**103.40**	**7.82**
SDW 90°C	C22-C9	616.01	6.97	101.66	101.67	639.59	7.30	101.65	101.65	639.35	7.30	101.66	101.66	23.59	0.33	103.32	6.87
SDW 90°C	C22-C10	614.39	6.94	101.68	101.67	635.72	7.26	101.67	101.65	635.49	7.26	101.66	101.66	21.33	0.33	103.34	6.35
SDW 90°C	**Average**			**101.67**	**101.67**	**637.66**	**7.28**	**101.66**	**101.65**	**637.42**	**7.28**	**101.66**	**101.66**	**22.46**	**0.33**	**103.33**	**6.61**
SCW 90°C	C22-C11	616.95	6.98	101.67	101.67	638.58	7.29	101.67	101.74	638.52	7.29	101.67	101.71	21.63	0.32	103.43	6.64
SCW 90°C	C22-C12	614.24	6.94	101.67	101.67	634.31	7.25	101.67	101.66	634.21	7.24	101.71	101.66	20.07	0.31	103.35	6.37
SCW 90°C	**Average**			**101.67**	**101.67**	**636.44**	**7.27**	**101.67**	**101.70**	**636.36**	**7.26**	**101.69**	**101.68**	**20.85**	**0.31**	**103.39**	**6.50**
SAW 90°C	C22-C13	614.94	6.96	101.66	101.68	635.15	7.25	101.69	101.67	634.60	7.24	101.71	101.67	20.22	0.29	103.38	6.74
SAW 90°C	C22-C14	615.96	6.96	101.66	101.67	636.42	7.26	101.72	101.66	635.82	7.26	101.69	101.68	20.46	0.30	103.40	6.65
SAW 90°C	**Average**			**101.66**	**101.67**	**635.79**	**7.25**	**101.70**	**101.66**	**635.21**	**7.25**	**101.70**	**101.68**	**20.34**	**0.29**	**103.39**	**6.70**

Table XI – Weight and dimensional measurements of SAM2X5-coated standard weight-loss samples, before and after long-term immersion testing in seven environments. These SAM2X5 coatings were produced with powder lot 06-015, and deposited on the nickel-based Alloy C-22 substrates with the high-velocity oxy-fuel (HVOF) process, using hydrogen as the fuel.

Weight & Dimensional Measurements of HVOF SAM2X5 Coatings on Alloy C-22 Weight-Loss Samples																	
Environment	Sample ID	Uncoated				Coated				Tested				Pre-Test Coating Based on Measurements			
		Weight	Thickness	Length	Width	Weight	Thickness	Length	Width	Weight	Thickness	Length	Width	Weight	Thickness	Area	Density
		grams	mm	mm	mm	grams	mm	mm	mm	grams	mm	mm	mm	grams	mm	cm^2	$grams/cm^3$
Seawater 90°C	C22-W1	625.73	7.04	101.67	101.66	654.53	7.44	101.72	101.70	654.10	7.46	101.70	101.74	28.80	0.41	103.44	6.87
Seawater 90°C	C22-W2	626.42	7.05	101.67	101.68	651.37	7.40	101.70	101.77	650.96	7.45	101.71	101.77	24.95	0.35	103.50	6.84
Seawater 90°C	**Average**			**101.67**	**101.67**	**652.95**	**7.42**	**101.71**	**101.73**	**652.53**	**7.45**	**101.70**	**101.76**	**26.88**	**0.38**	**103.47**	**6.86**
3.5 m NaCl 30°C	C22-W3	624.54	7.03	101.67	101.68	649.64	7.38	101.65	101.64	649.39	7.40	101.67	101.66	25.10	0.36	103.31	6.84
3.5 m NaCl 30°C	C22-W4	622.67	7.01	101.68	101.67	647.62	7.36	101.63	101.66	647.38	7.37	101.67	101.66	24.94	0.35	103.31	6.90
3.5 m NaCl 30°C	**Average**			**101.67**	**101.67**	**648.63**	**7.37**	**101.64**	**101.65**	**648.39**	**7.38**	**101.67**	**101.66**	**25.02**	**0.35**	**103.31**	**6.87**
3.5 m NaCl 90°C	C22-W5	621.49	7.00	101.68	101.67	648.93	7.38	101.71	101.71	648.11	7.40	101.69	101.74	27.44	0.39	103.44	6.89
3.5 m NaCl 90°C	C22-W6	628.73	7.07	101.68	101.67	649.13	7.37	101.71	101.69	648.43	7.40	101.72	101.69	20.40	0.30	103.42	6.52
3.5 m NaCl 90°C	**Average**			**101.68**	**101.67**	**649.03**	**7.38**	**101.71**	**101.70**	**648.27**	**7.40**	**101.71**	**101.71**	**23.92**	**0.34**	**103.43**	**6.71**
3.5 m NaCl + 0.525 m KNO_3 90ºC	C22-W7	620.69	7.00	101.67	101.67	644.50	7.33	101.74	101.75	644.38	7.33	101.72	101.77	23.81	0.32	103.52	7.08
3.5 m NaCl + 0.525 m KNO_3 90ºC	C22-W8	625.27	7.04	101.67	101.67	645.65	7.33	101.70	101.72	645.50	7.34	101.72	101.69	20.39	0.29	103.44	6.74
3.5 m NaCl + 0.525 m KNO_3 90ºC	**Average**			**101.67**	**101.67**	**645.08**	**7.33**	**101.72**	**101.73**	**644.94**	**7.33**	**101.72**	**101.73**	**22.10**	**0.31**	**103.48**	**6.91**
SDW 90°C	C22-W9	625.17	7.03	101.68	101.68	645.55	7.33	101.63	101.65	645.30	7.32	101.68	101.68	20.38	0.29	103.30	6.74
SDW 90°C	C22-W10	619.16	6.97	101.66	101.66	641.06	7.28	101.67	101.64	640.82	7.29	101.65	101.66	21.90	0.31	103.33	6.78
SDW 90°C	**Average**			**101.67**	**101.67**	**643.31**	**7.30**	**101.65**	**101.64**	**643.06**	**7.30**	**101.66**	**101.67**	**21.14**	**0.30**	**103.32**	**6.76**
SCW 90°C	C22-W11	620.77	6.99	101.66	101.66	653.91	7.44	101.62	101.63	653.84	7.43	101.67	101.64	33.14	0.45	103.28	7.09
SCW 90°C	C22-W12	623.87	7.01	101.71	101.71	652.63	7.41	101.70	101.75	652.54	7.40	101.72	101.72	28.76	0.40	103.47	6.99
SCW 90°C	**Average**			**101.69**	**101.68**	**653.27**	**7.42**	**101.66**	**101.69**	**653.19**	**7.42**	**101.70**	**101.68**	**30.95**	**0.43**	**103.37**	**7.04**
SAW 90°C	C22-W13	621.72	7.00	101.66	101.67	649.87	7.39	101.68	101.64	649.40	7.39	101.67	101.66	28.16	0.39	103.34	6.94
SAW 90°C	C22-W14	622.52	7.01	101.67	101.67	650.59	7.39	101.64	101.67	650.09	7.39	101.65	101.66	28.07	0.39	103.33	7.06
SAW 90°C	**Average**			**101.66**	**101.67**	**650.23**	**7.39**	**101.66**	**101.65**	**649.75**	**7.39**	**101.66**	**101.66**	**28.11**	**0.39**	**103.33**	**7.00**

Table XII – Corrosion rates calculated from the weight and dimensional measurements of SAM2X5-coated crevice-corrosion samples are summarized here, along with the final values of corrosion rate determined with linear polarization. The corrosion rates based on weight loss were calculated with two possible values of the SAM2X5 density: Basis 1 used the density values calculated from the weights and dimensions of the applied coatings, which may indicate that these coatings were not fully dense; Basis 2 used the density for the fully-dense alloy.

		Corrosion Rate Calculations for HVOF SAM2X5 Coatings on Alloy C-22 Crevice Samples								
Environment	Sample ID	Exposure Time	Difference	Basis 1: Assume Porous Coating			Basis 2: Assume Full-Density Alloy			Linear Polarization
		Test Duration	Wt. Loss	Density	Penetration	Rate	Density	Penetration	Rate	Rate
		days	grams	grams/cm^3	microns	microns/yr	grams/cm^3	microns	microns/yr	microns/yr
Seawater 90°C	C22-C1	135	0.42	6.59	6.20	16.76	7.65	5.34	14.44	
Seawater 90°C	C22-C2	135	0.45	6.35	6.63	17.94	7.65	5.51	14.89	
Seawater 90°C	**Average**		**0.44**	**6.47**	**6.42**	**17.35**	**7.65**	**5.42**	**14.67**	**12.27**
3.5 m NaCl 30°C	C22-C3	135	0.26	6.63	3.81	10.29	7.65	3.30	8.91	
3.5 m NaCl 30°C	C22-C4	135	0.26	6.99	3.55	9.59	7.65	3.24	8.76	
3.5 m NaCl 30°C	**Average**		**0.26**	**6.81**	**3.68**	**9.94**	**7.65**	**3.27**	**8.84**	**2.91**
3.5 m NaCl 90°C	C22-C5	135	0.88	6.79	12.50	33.79	7.65	11.10	30.00	
3.5 m NaCl 90°C	C22-C6	135	0.81	6.76	11.55	31.21	7.65	10.20	27.58	
3.5 m NaCl 90°C	**Average**		**0.84**	**6.78**	**12.02**	**32.50**	**7.65**	**10.65**	**28.79**	**175.71**
3.5 m NaCl + 0.525 m KNO_3 90ºC	C22-C7	135	0.13	8.75	1.47	3.96	7.65	1.68	4.53	
3.5 m NaCl + 0.525 m KNO_3 90ºC	C22-C8	135	0.12	6.89	1.70	4.60	7.65	1.53	4.15	
3.5 m NaCl + 0.525 m KNO_3 90ºC	**Average**		**0.13**	**7.82**	**1.58**	**4.28**	**7.65**	**1.60**	**4.34**	**2.83**
SDW 90°C	C22-C9	135	0.25	6.87	3.46	9.35	7.65	3.10	8.39	
SDW 90°C	C22-C10	135	0.23	6.35	3.58	9.67	7.65	2.97	8.03	
SDW 90°C	**Average**		**0.24**	**6.61**	**3.52**	**9.51**	**7.65**	**3.04**	**8.21**	**2.61**
SCW 90°C	C22-C11	135	0.06	6.64	0.84	2.28	7.65	0.73	1.98	
SCW 90°C	C22-C12	135	0.10	6.37	1.54	4.16	7.65	1.28	3.47	
SCW 90°C	**Average**		**0.08**	**6.50**	**1.19**	**3.22**	**7.65**	**1.01**	**2.72**	**12.38**
SAW 90°C	C22-C13	135	0.56	6.74	7.98	21.58	7.65	7.04	19.03	
SAW 90°C	C22-C14	135	0.60	6.65	8.70	23.51	7.65	7.56	20.44	
SAW 90°C	**Average**		**0.58**	**6.70**	**8.34**	**22.55**	**7.65**	**7.30**	**19.73**	**81.05**

Table XIII – Corrosion rates calculated from the weight and dimensional measurements of SAM2X5-coated weight-loss samples are summarized here, along with the final values of corrosion rate determined with linear polarization. The corrosion rates based on weight loss were calculated with two possible values of the SAM2X5 density: Basis 1 used the density values calculated from the weights and dimensions of the applied coatings, which may indicate that these coatings were not fully dense; Basis 2 used the density for the fully-dense alloy.

		Corrosion Rate Calculations for HVOF SAM2X5 Coatings on Alloy C-22 Weight-Loss Samples								
Environment	Sample ID	Exposure Time	Difference	Basis 1: Assume Porous Coating			Basis 2: Assume Full-Density Alloy			Linear Polarization
		Test Duration	Wt. Loss	Density	Penetration	Rate	Density	Penetration	Rate	Rate
		days	grams	grams/cm^3	microns	microns/yr	grams/cm^3	microns	microns/yr	microns/yr
Seawater 90°C	C22-W1	135	0.42	6.87	5.97	16.14	7.65	5.36	14.50	
Seawater 90°C	C22-W2	135	0.41	6.84	5.79	15.67	7.65	5.18	14.01	
Seawater 90°C	**Average**		**0.42**	**6.86**	**5.88**	**15.90**	**7.65**	**5.27**	**14.26**	**12.27**
3.5 m NaCl 30°C	C22-W3	135	0.25	6.84	3.48	9.41	7.65	3.11	8.42	
3.5 m NaCl 30°C	C22-W4	135	0.24	6.90	3.40	9.21	7.65	3.07	8.30	
3.5 m NaCl 30°C	**Average**		**0.24**	**6.87**	**3.44**	**9.31**	**7.65**	**3.09**	**8.36**	**2.91**
3.5 m NaCl 90°C	C22-W5	135	0.83	6.89	11.62	31.40	7.65	10.46	28.29	
3.5 m NaCl 90°C	C22-W6	135	0.70	6.52	10.38	28.05	7.65	8.85	23.92	
3.5 m NaCl 90°C	**Average**		**0.76**	**6.71**	**11.00**	**29.73**	**7.65**	**9.65**	**26.10**	**175.71**
3.5 m NaCl + 0.525 m KNO_3 90ºC	C22-W7	135	0.12	7.08	1.64	4.43	7.65	1.52	4.10	
3.5 m NaCl + 0.525 m KNO_3 90ºC	C22-W8	135	0.15	6.74	2.14	5.78	7.65	1.88	5.09	
3.5 m NaCl + 0.525 m KNO_3 90ºC	**Average**		**0.13**	**6.91**	**1.89**	**5.10**	**7.65**	**1.70**	**4.59**	**2.83**
SDW 90°C	C22-W9	135	0.25	6.74	3.56	9.63	7.65	3.14	8.49	
SDW 90°C	C22-W10	135	0.24	6.78	3.37	9.12	7.65	2.99	8.09	
SDW 90°C	**Average**		**0.24**	**6.76**	**3.47**	**9.38**	**7.65**	**3.07**	**8.29**	**2.61**
SCW 90°C	C22-W11	135	0.07	7.09	0.96	2.61	7.65	0.89	2.42	
SCW 90°C	C22-W12	135	0.09	6.99	1.28	3.45	7.65	1.17	3.15	
SCW 90°C	**Average**		**0.08**	**7.04**	**1.12**	**3.03**	**7.65**	**1.03**	**2.79**	**12.38**
SAW 90°C	C22-W13	135	0.48	6.94	6.63	17.92	7.65	6.01	16.26	
SAW 90°C	C22-W14	135	0.49	7.06	6.74	18.23	7.65	6.22	16.82	
SAW 90°C	**Average**		**0.48**	**7.00**	**6.69**	**18.08**	**7.65**	**6.12**	**16.54**	**81.05**

Table XIV – Values of the pitting resistance equivalence number (PREN) for reference alloys and Fe-based amorphous metals.

Alloy	Low	Ave	High
316L	23	26	30
C-22	65	71	76
SAM2X5	66	74	90

FIGURES

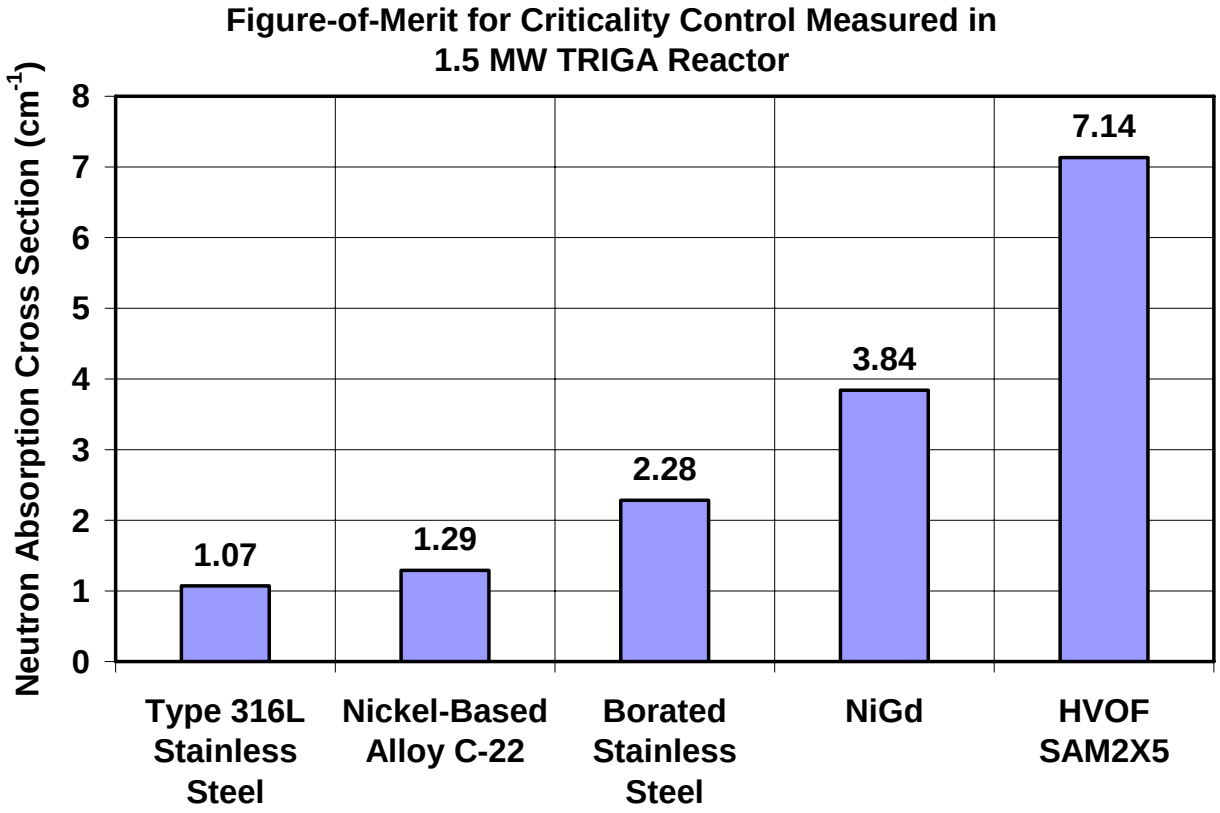

Figure 1 – Average values of the neutron absorption cross sections for several baseline criticality control (neutron absorbing) materials, all compared to the average value for SAM2X5 ($Fe_{49.7}Cr_{17.7}Mn_{1.9}Mo_{7.4}W_{1.6}B_{15.2}C_{3.8}Si_{2.4}$) thermal-spray coatings.

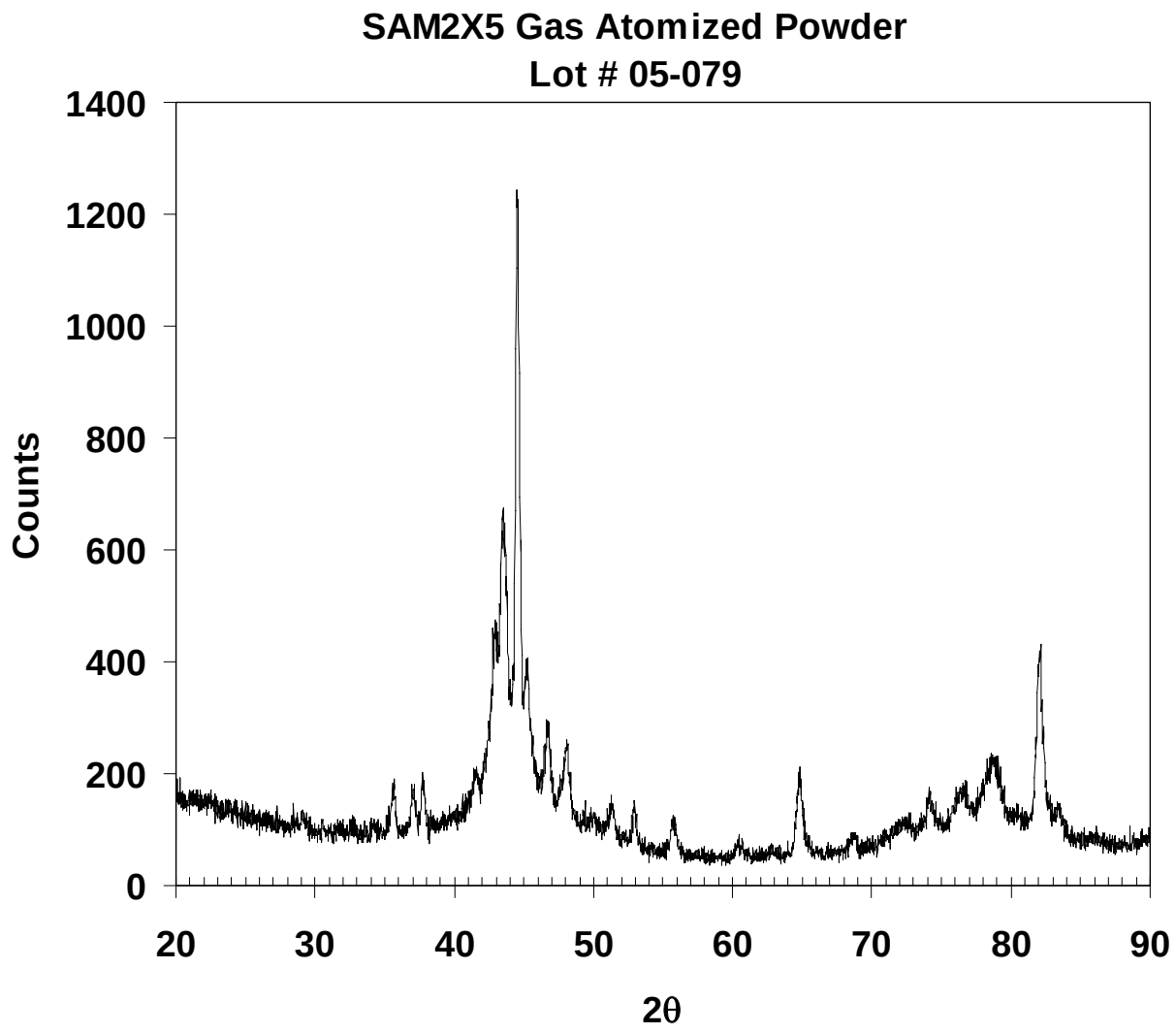

Figure 2 – X-ray diffraction (XRD) data for SAM2X5 ($Fe_{49.7}Cr_{17.7}Mn_{1.9}Mo_{7.4}W_{1.6}B_{15.2}C_{3.8}Si_{2.4}$) powder identified as Lot # 05-079.

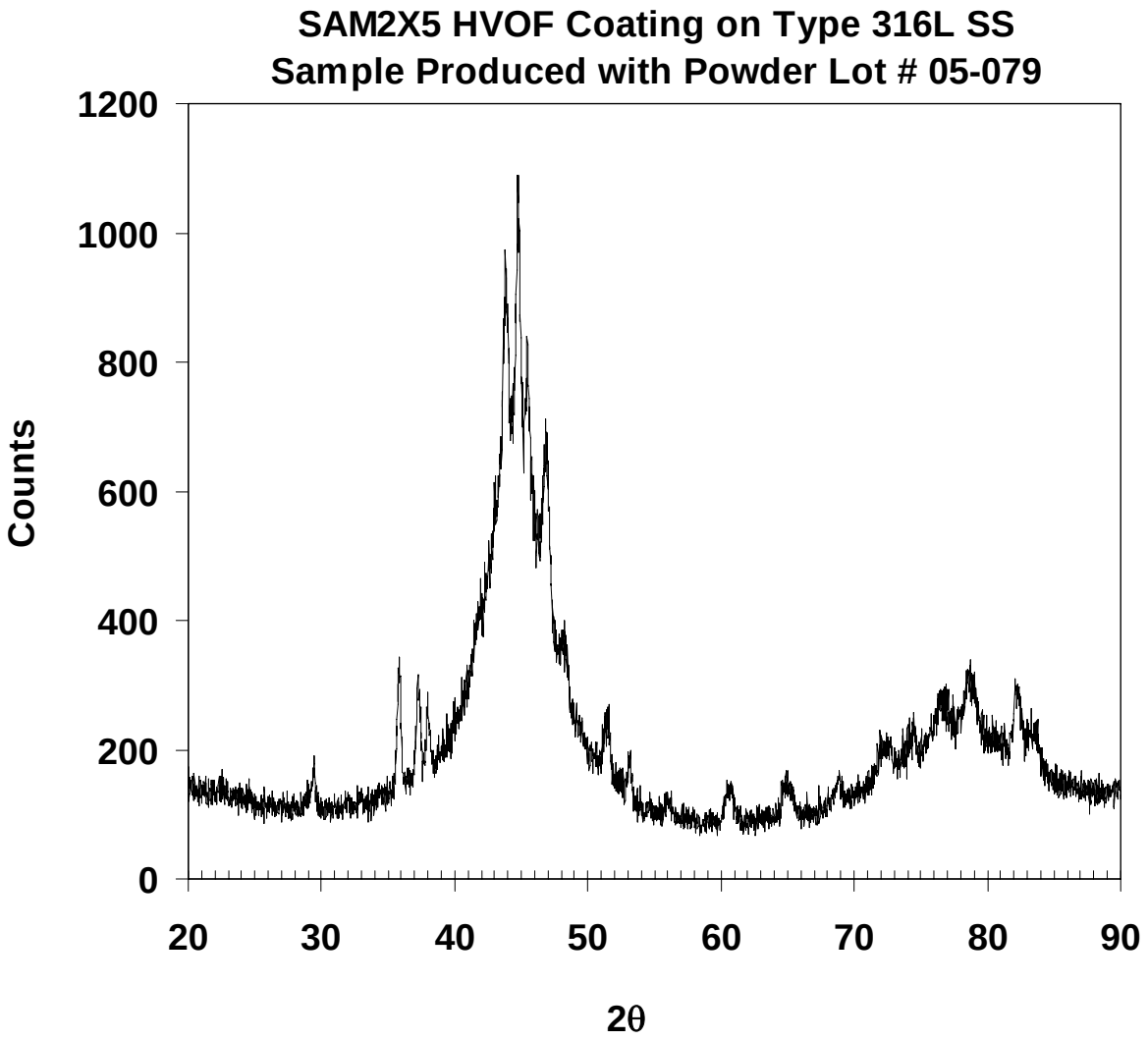

Figure 3 – X-ray diffraction (XRD) data for SAM2X5 coating (powder lot # 05-079) on Type 316L stainless steel substrate.

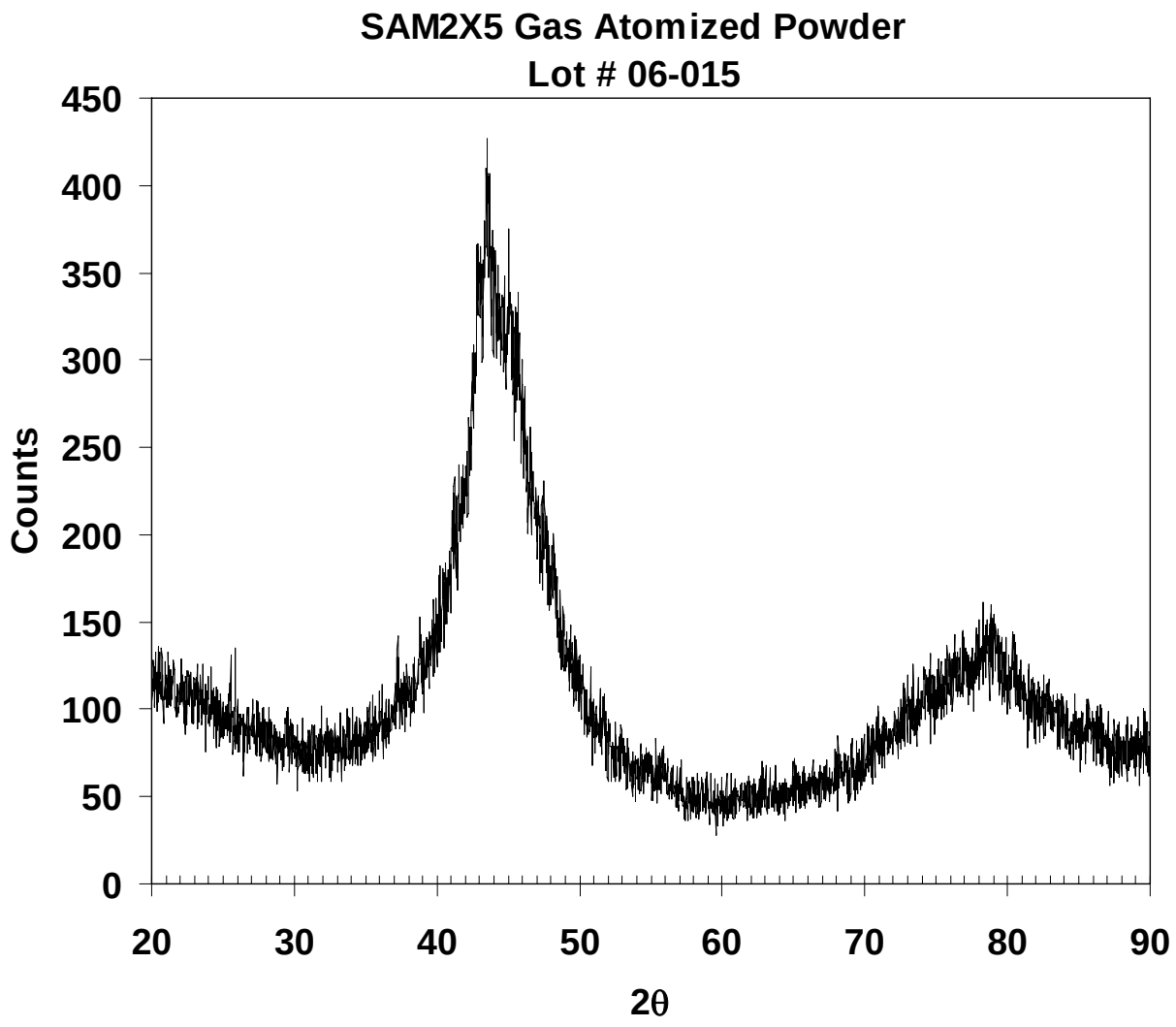

Figure 4 – X-ray diffraction (XRD) data for SAM2X5 ($Fe_{49.7}Cr_{17.7}Mn_{1.9}Mo_{7.4}W_{1.6}B_{15.2}C_{3.8}Si_{2.4}$) powder identified as Lot # 06-015.

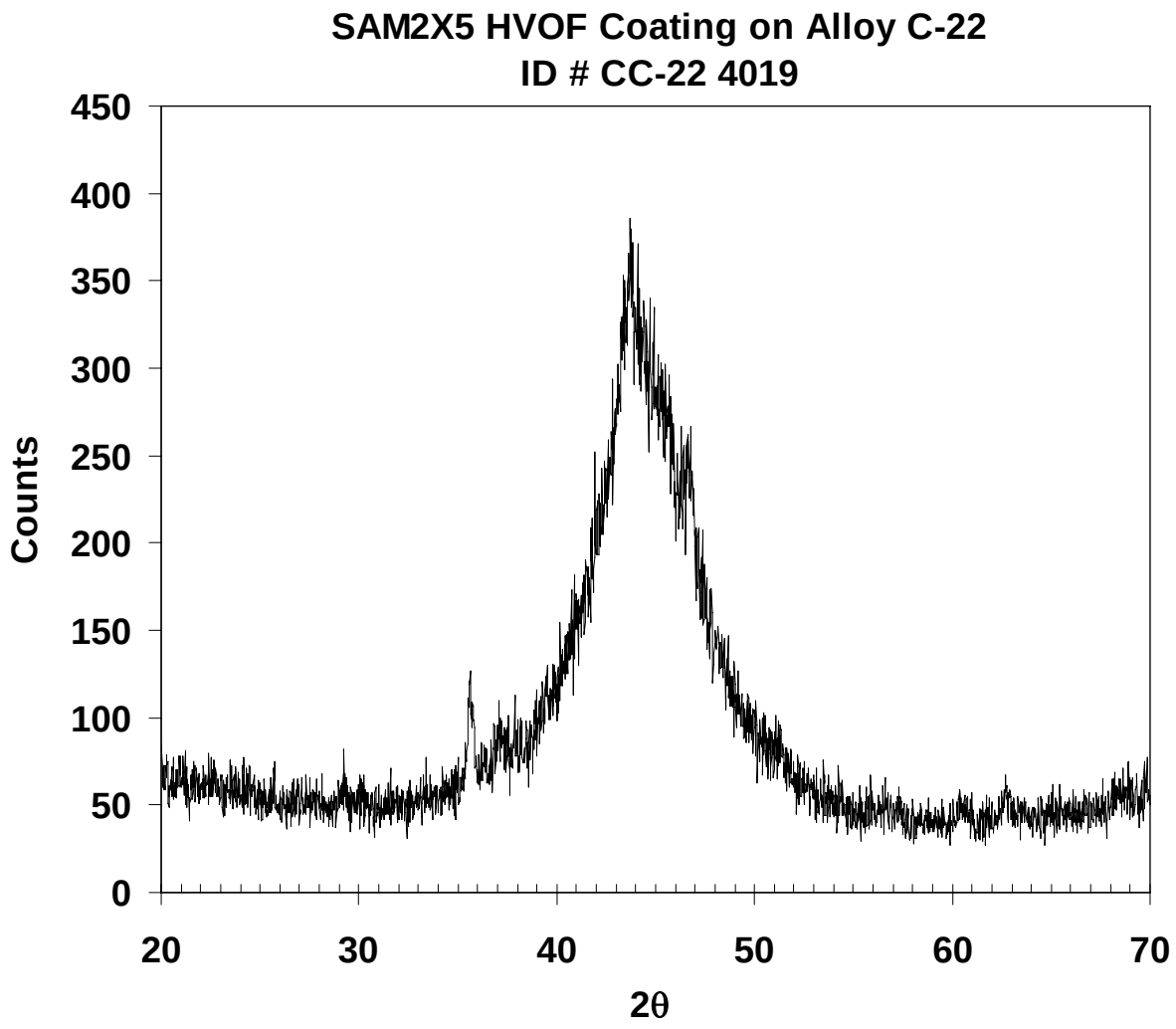

Figure 5 – X-ray diffraction (XRD) data for SAM2X5 coating (powder lot # 06-015) on Alloy C-22 substrate (# CC-22 4019).

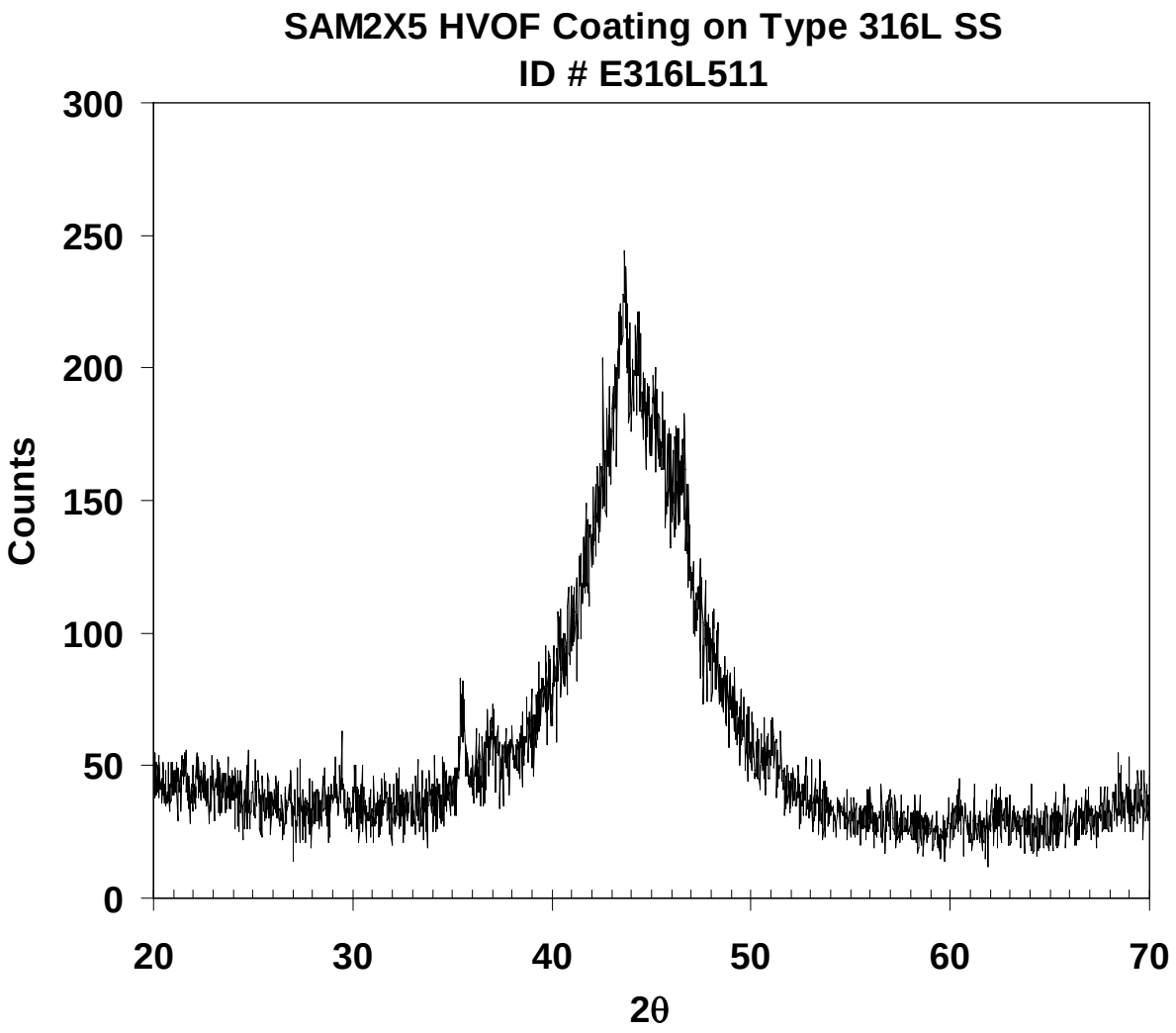

Figure 6 – X-ray diffraction (XRD) data for SAM2X5 coating (powder lot # 06-015) on Type 316L stainless steel substrate (sample # E316L511).

Figure 7 – Reference samples of 1018 carbon steel after eight (8) full cycles in the GM salt fog test.

Figure 8 – Half-scale model of spent-nuclear-fuel (SNF) container fabricated from Type 316L stainless steel pipe (Schedule 10s) coated with SAM2X5 (powder lot # 06-015) after eight (8) full cycles in GM salt fog test.

Figure 9 – Side views SAM2X5-coated container shown in Figure 8 after eight (8) full cycles in salt fog test.

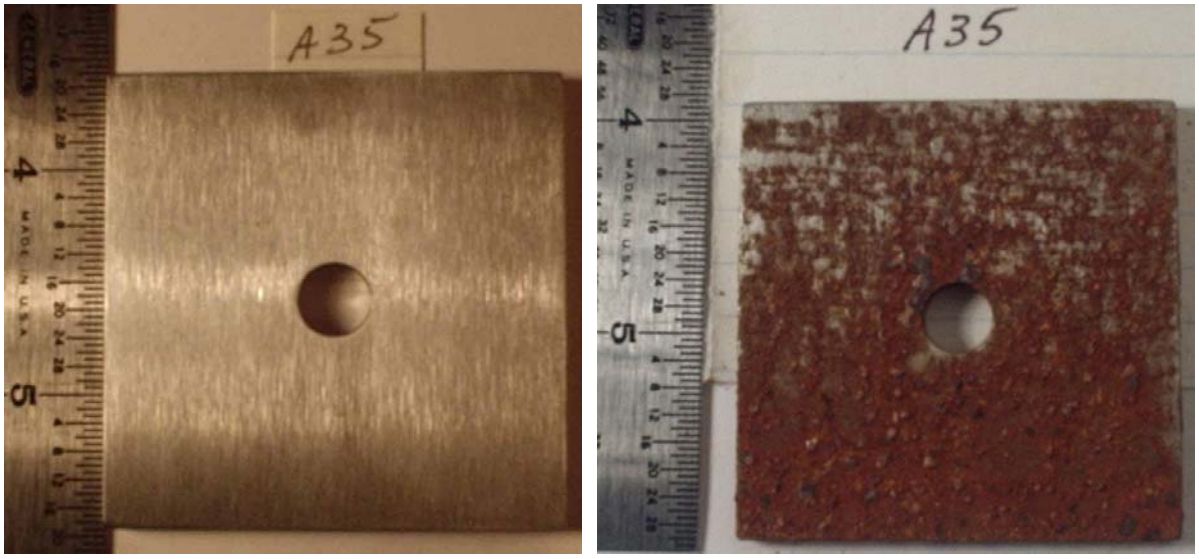

Figure 10 – Photographs of 1018 carbon steel reference specimens (Sample # A35), before (left) and after (right) 8 abbreviated cycles in GM salt fog test.

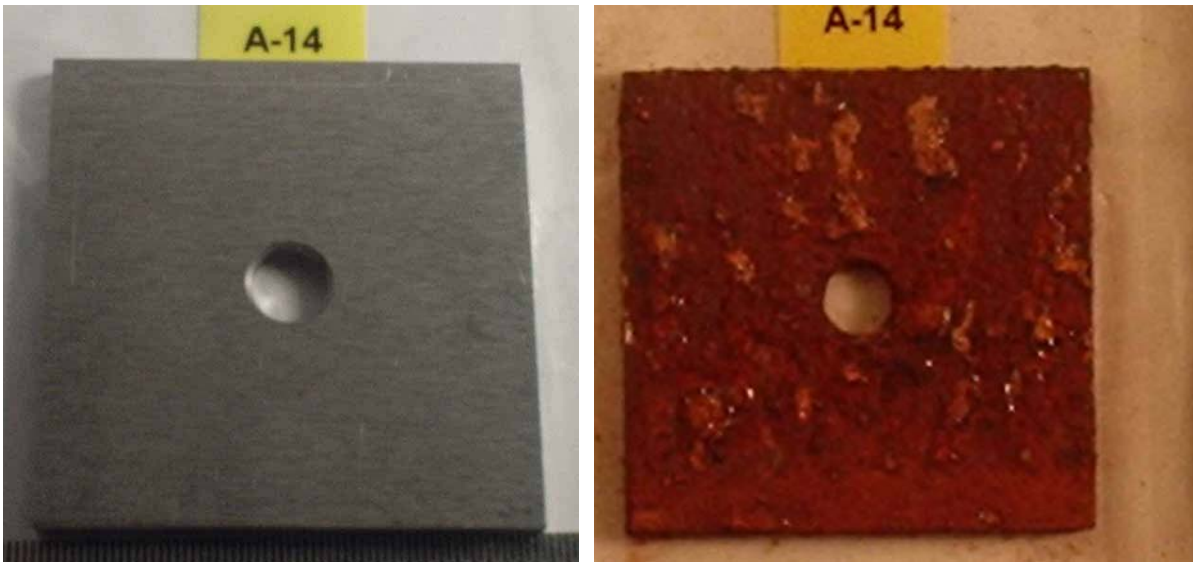

Figure 11 – Photographs of 1018 carbon steel reference specimens (Samples # A14), before (left) and after (right) 8 full cycles in GM salt fog test.

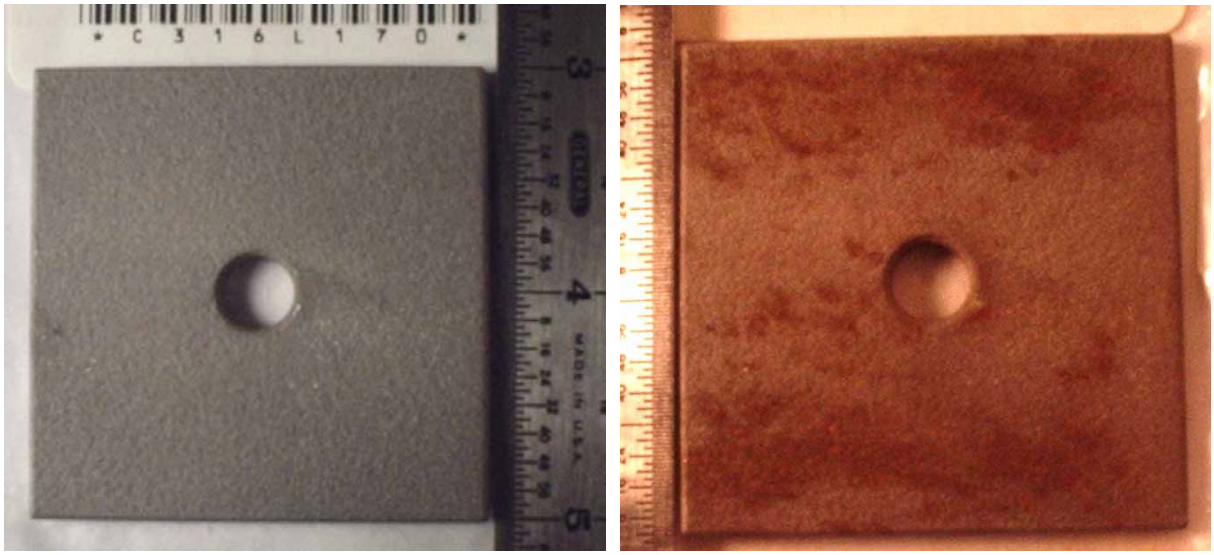

Figure 12 – Photographs showing of HVOF coating of 316 stainless steel on Type 316L stainless steel substrate (Sample # 316-170), before (left) and after (right) 8 abbreviated cycles in GM salt fog test.

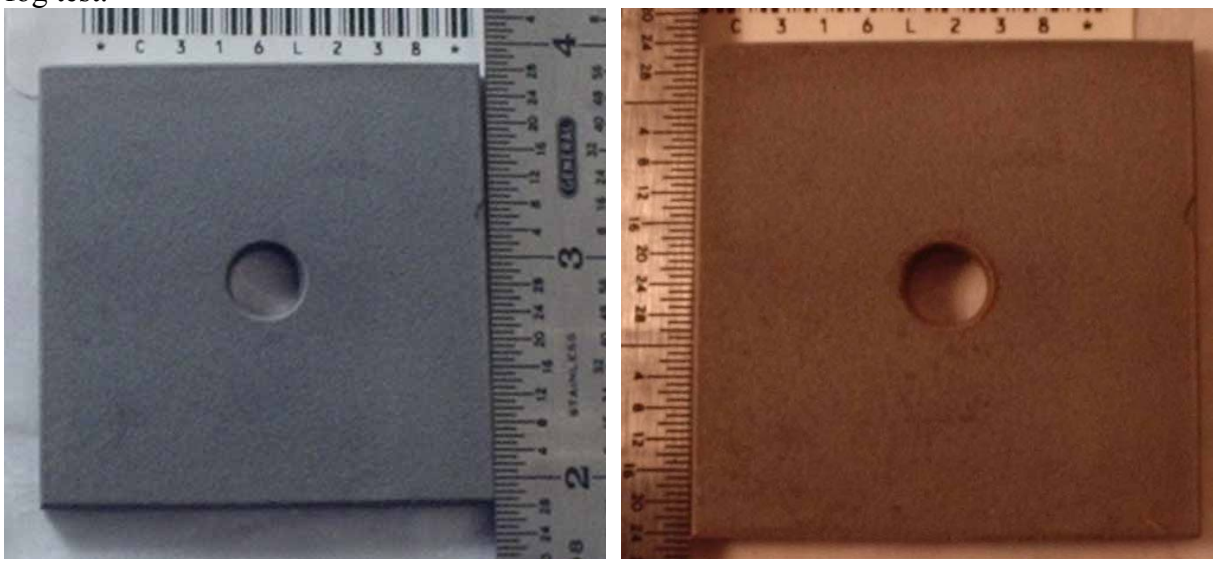

Figure 13 – Photographs of HVOF coating of Alloy C-22 on Type 316L stainless steel substrate, (Sample # 316-238), before (left) and after (right) 8 abbreviated cycles in GM salt fog test.

Figure 14 – Photographs of early HVOF SAM40 coating on Type 316L stainless steel substrate (Sample # 316-041), before (left) and after (right) 8 abbreviated cycles in GM salt fog test.

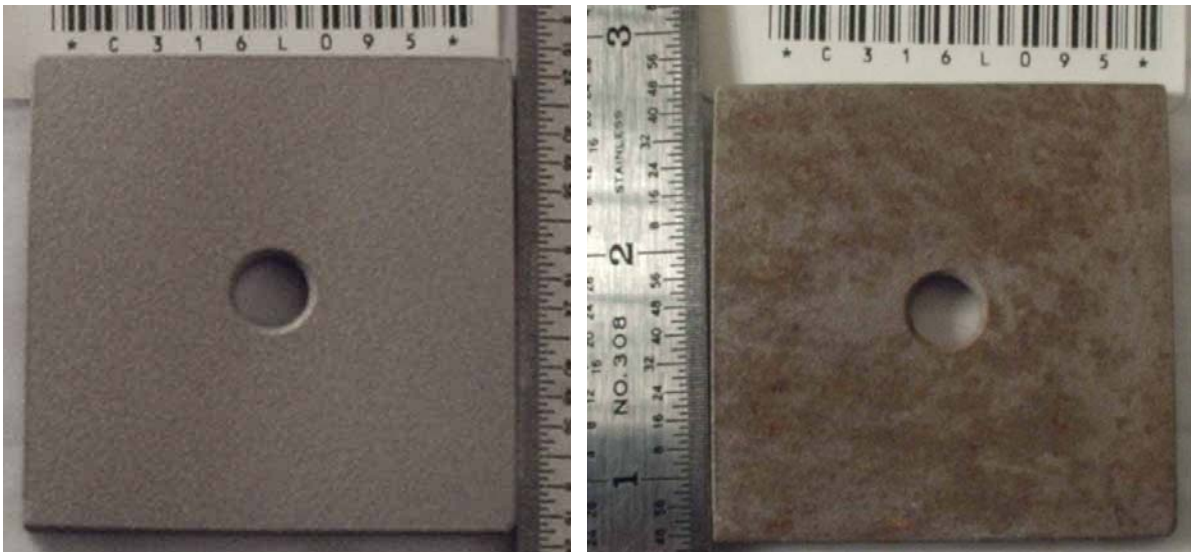

Figure 15 – Photographs of early HVOF coating of SAM40X3 on Type 316L stainless steel substrate (Sample # 316-095), before (left) and after (right) 8 abbreviated cycles in GM salt fog test.

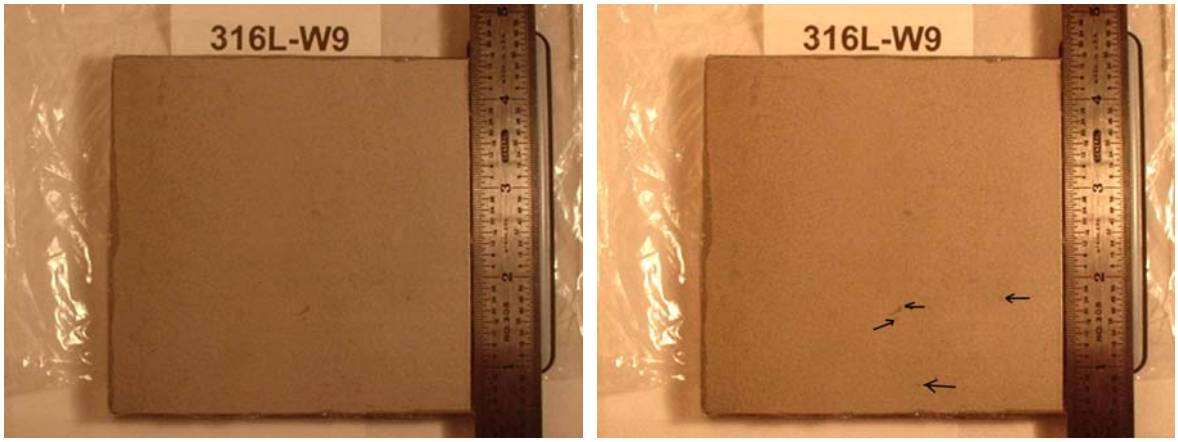

Figure 16 – Photograph of HVOF coating of SAM2X5 on Type 316L stainless steel substrate (Sample # 316L-W9), before (left) and after (right) 8 full cycles in GM salt-fog test. The arrows were added to the image to pinpoint small suspected rust spots.

Figure 17 – Photograph of HVOF coating of SAM2X5 on nickel-based Alloy C-22 substrate (Sample # C22-W21), before (left) and after (right) 8 full cycles in GM salt-fog test. There were no suspected rust spots observed on this specimen.

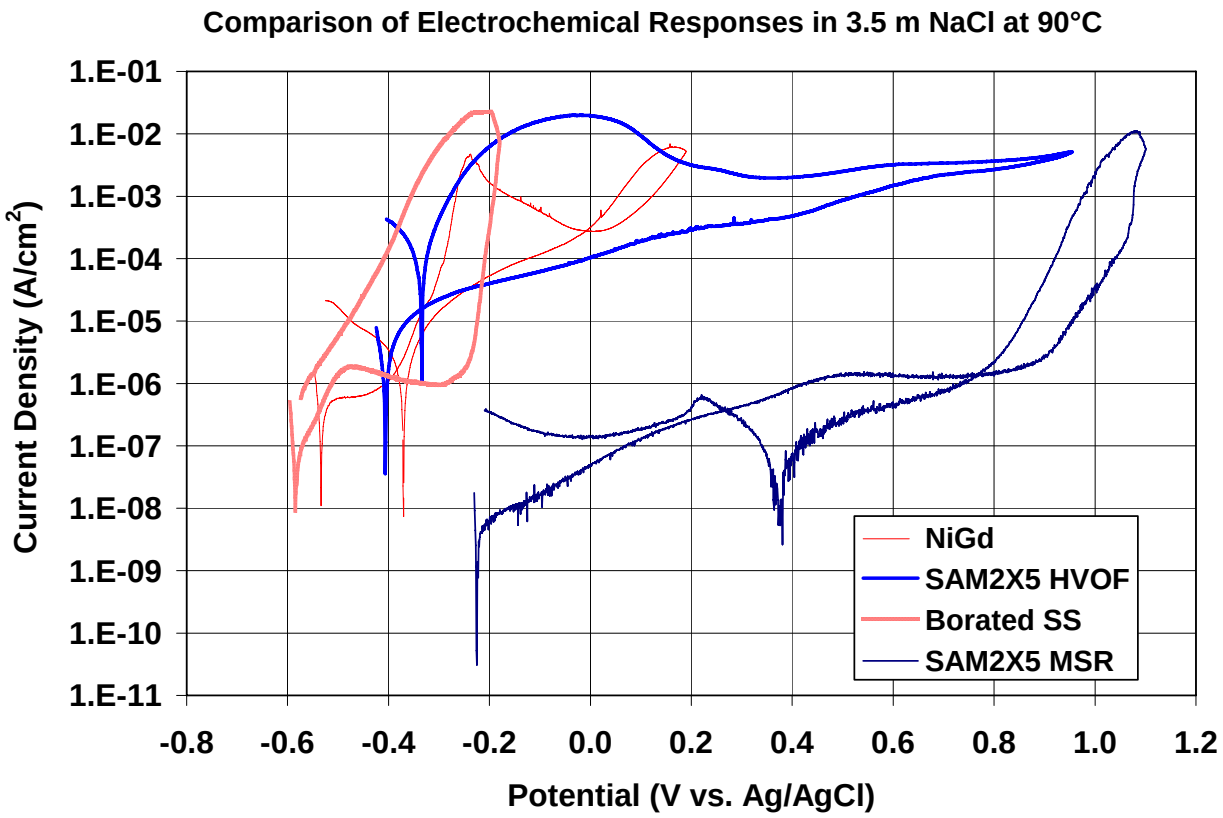

Figure 18 – Cyclic polarization of SAM2X5 melt-spun ribbon, SAM2X5 coating (powder lot # 06-015), borated stainless steel, and NiGd (Ni-Cr-Mo-Gd) in 3.5-molal solution of NaCl at 90°C.

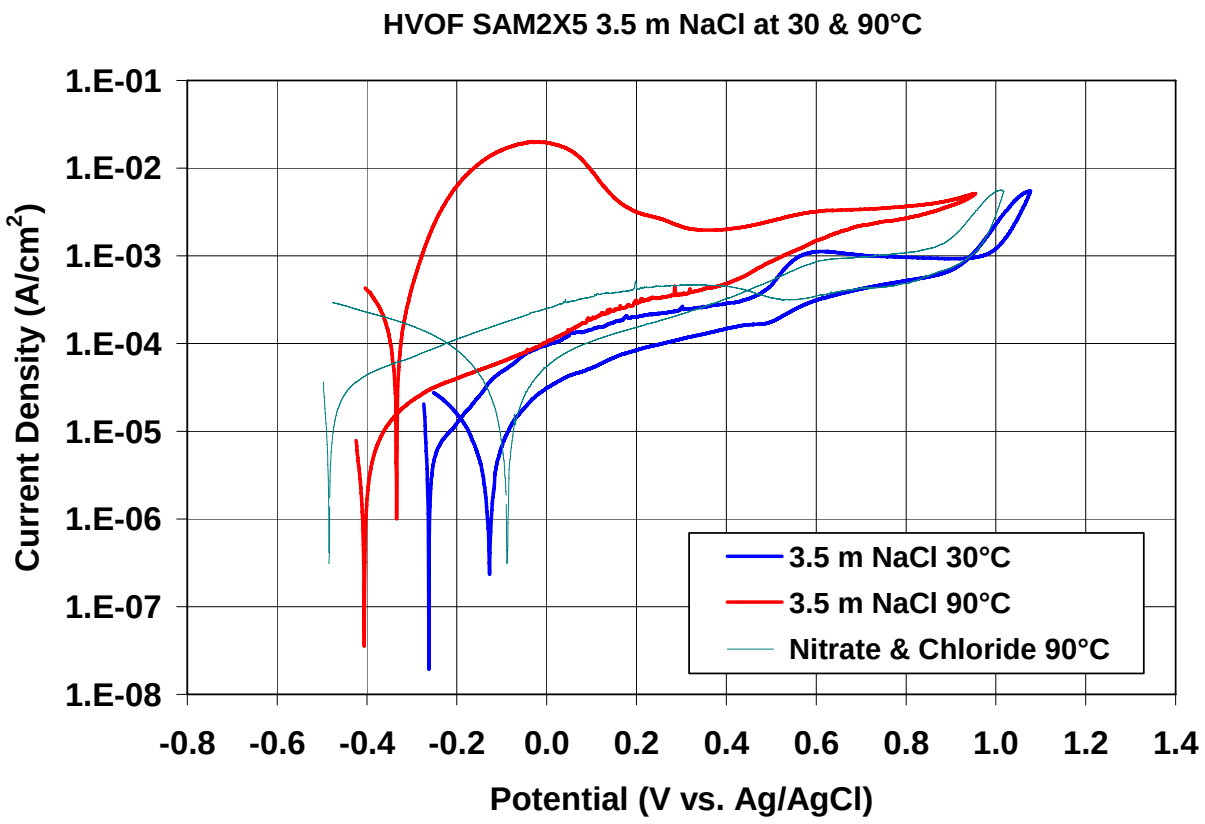

Figure 19 – Cyclic polarization of SAM2X5 coatings (powder lot # 06-015) on Type 316L stainless steel substrates in a 3.5-molal NaCl solution at 30 and 90°C, as well as in a more complex electrolyte with 3.5-molal NaCl and 0.525-molal KNO_3.

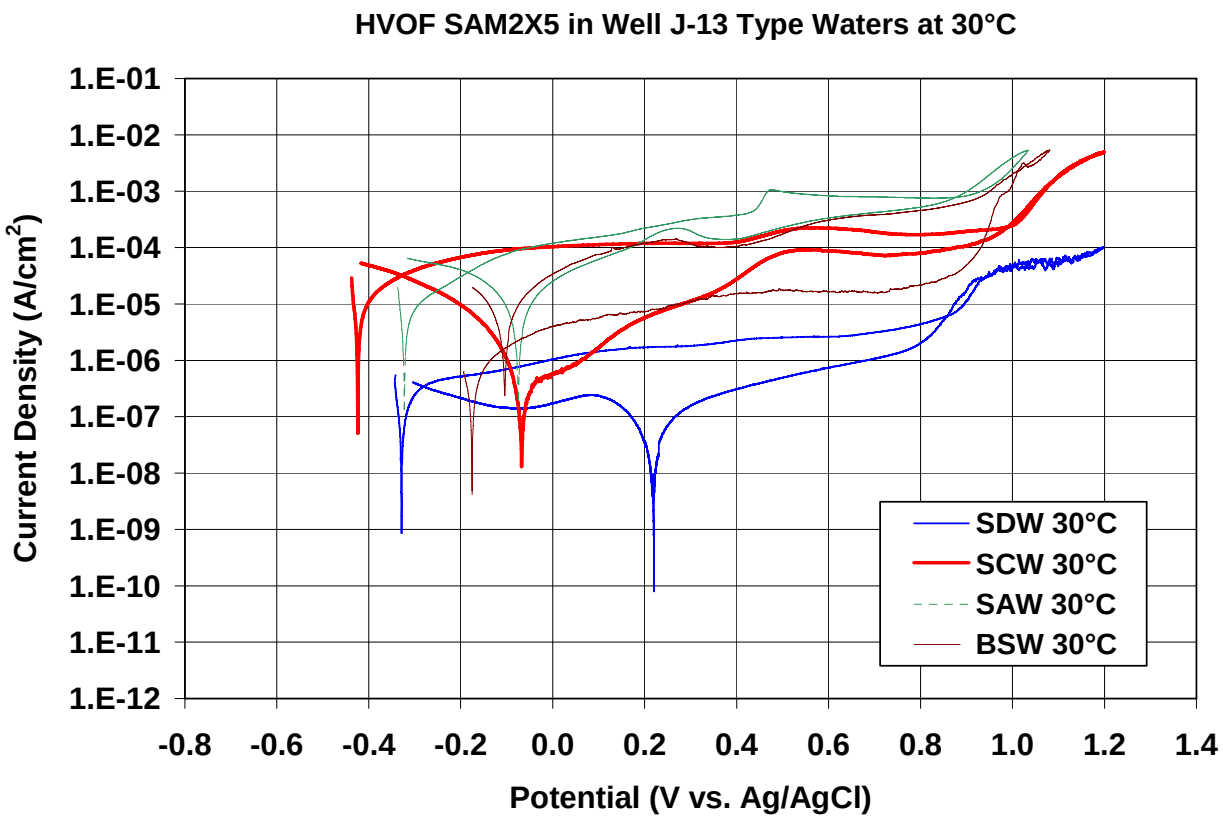

Figure 20 – Cyclic polarization of SAM2X5 coatings (powder lot # 06-015) on Type 316L stainless steel substrates in SDW, SCW, SAW and BSW at 30°C.

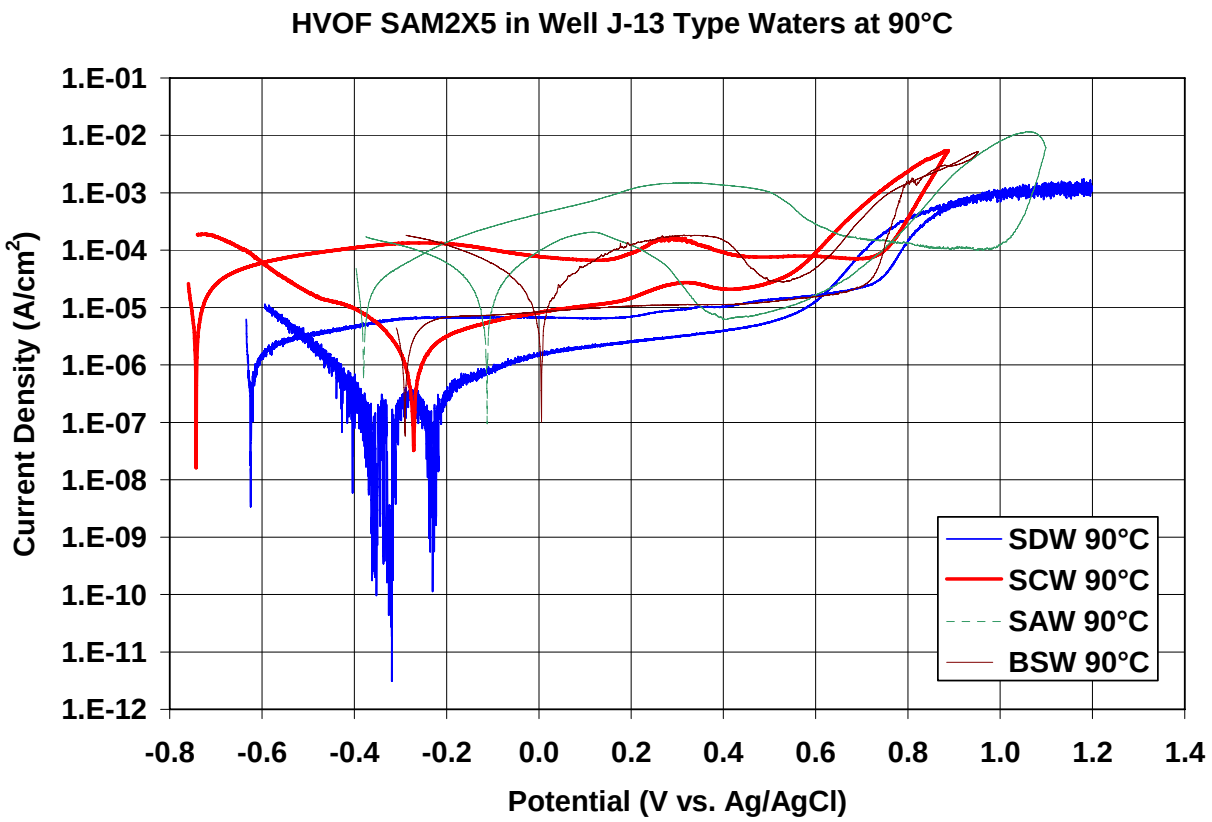

Figure 21 – Cyclic polarization of SAM2X5 coatings (powder lot # 06-015) on Type 316L stainless steel substrates in SDW, SCW, SAW and BSW at 90°C.

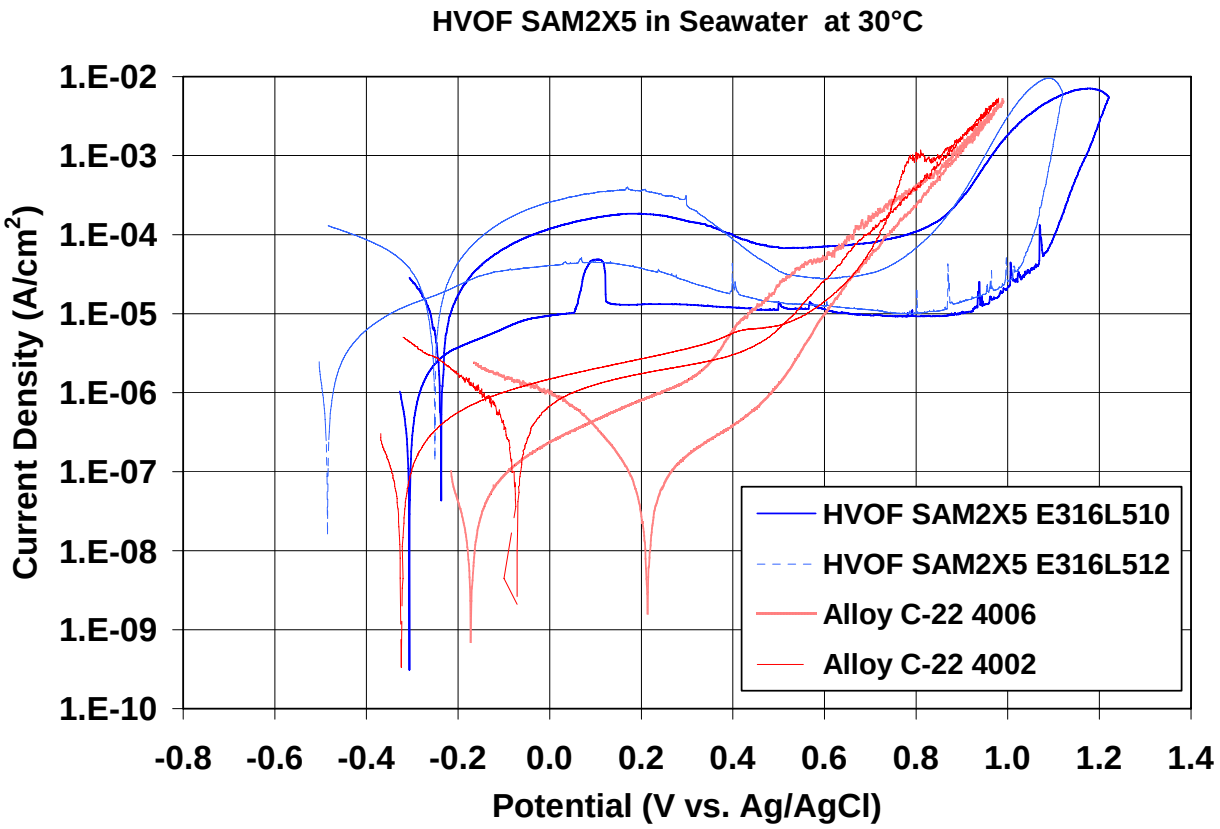

Figure 22 – Cyclic polarization of SAM2X5 coatings (powder lot # 06-015) on Type 316L stainless steel substrates (samples # E316L510 and # E316L512) in natural seawater at 30°C, with reference data a sample of wrought Ni-based Alloy C-22 (samples # 4002 and # 4006).

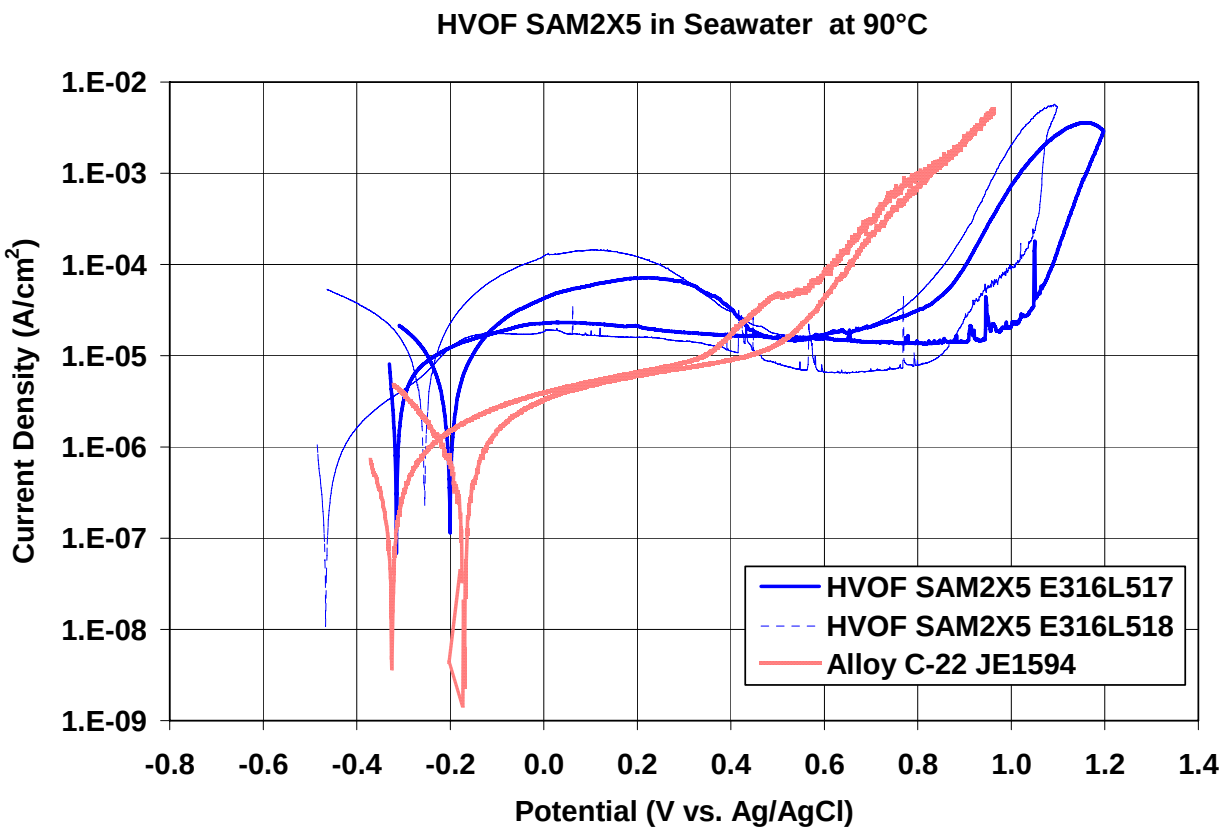

Figure 23 – Cyclic polarization of SAM2X5 coatings (powder lot # 06-015) on Type 316L stainless steel substrates (samples # E316L517 and # E316L518) in natural seawater at 90°C, with reference data a sample of wrought Ni-based Alloy C-22 (sample # JE1594).

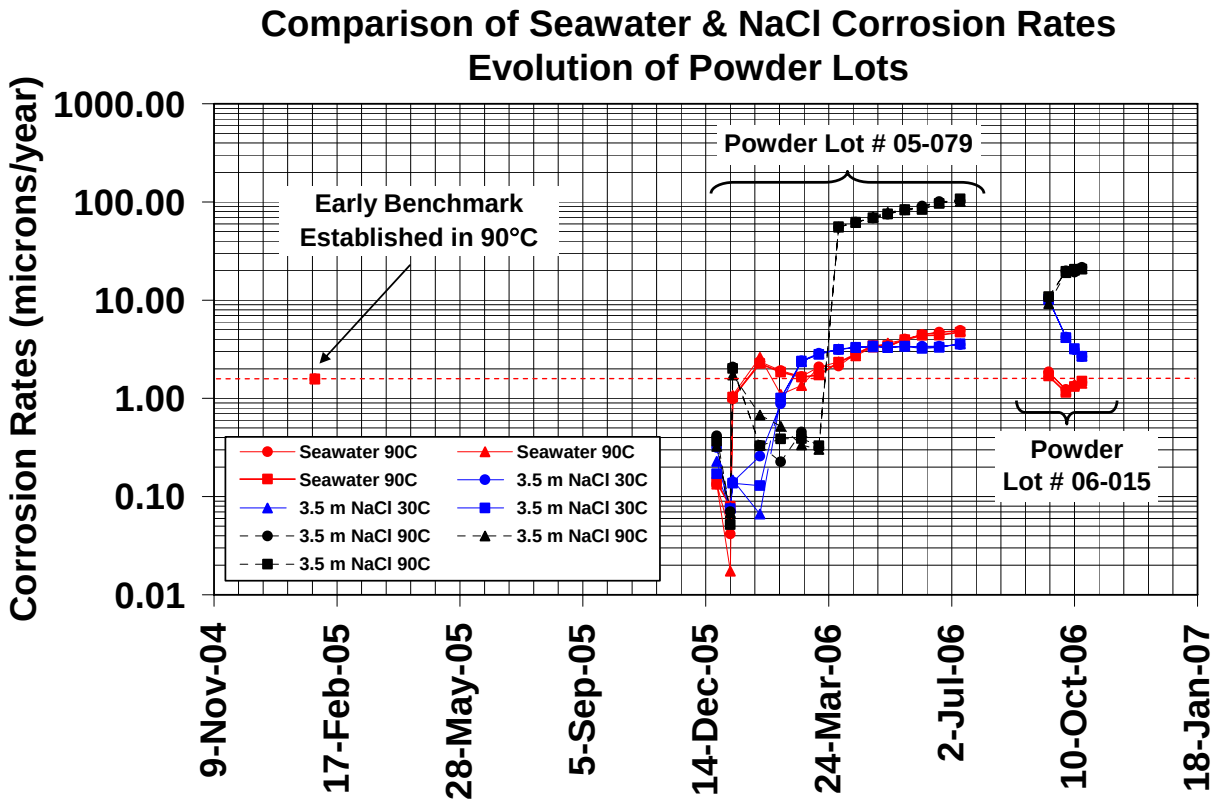

Figure 24 – Apparent corrosion rates determined with linear polarization during long-term open circuit corrosion testing of SAM2X5-coated samples prepared with lots of powder produced in 2004, 2005 (Lot #05-079) and 2006 (Lot #06-015).

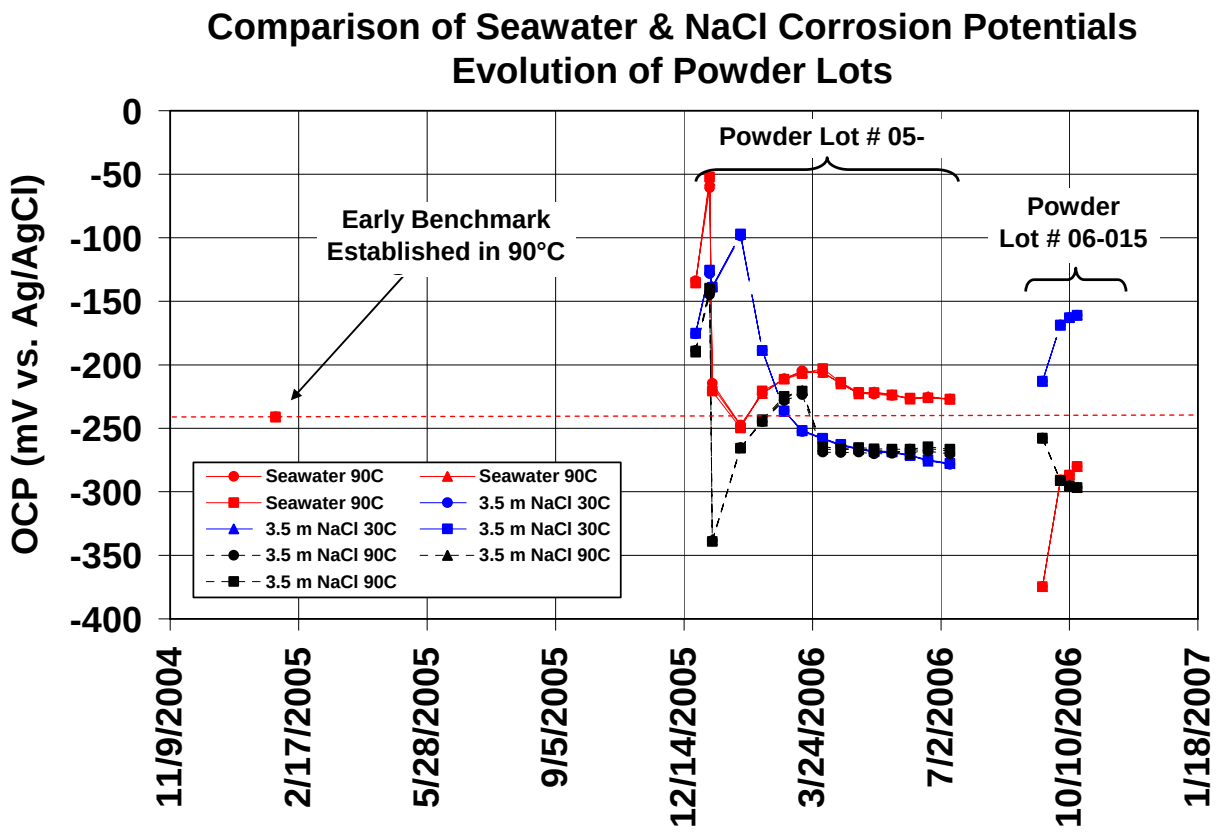

Figure 25 – OCP values during long-term open circuit corrosion testing of SAM2X5-coated samples prepared with lots of powder produced in 2004, 2005 (Lot #05-079) and 2006 (Lot #06-015).

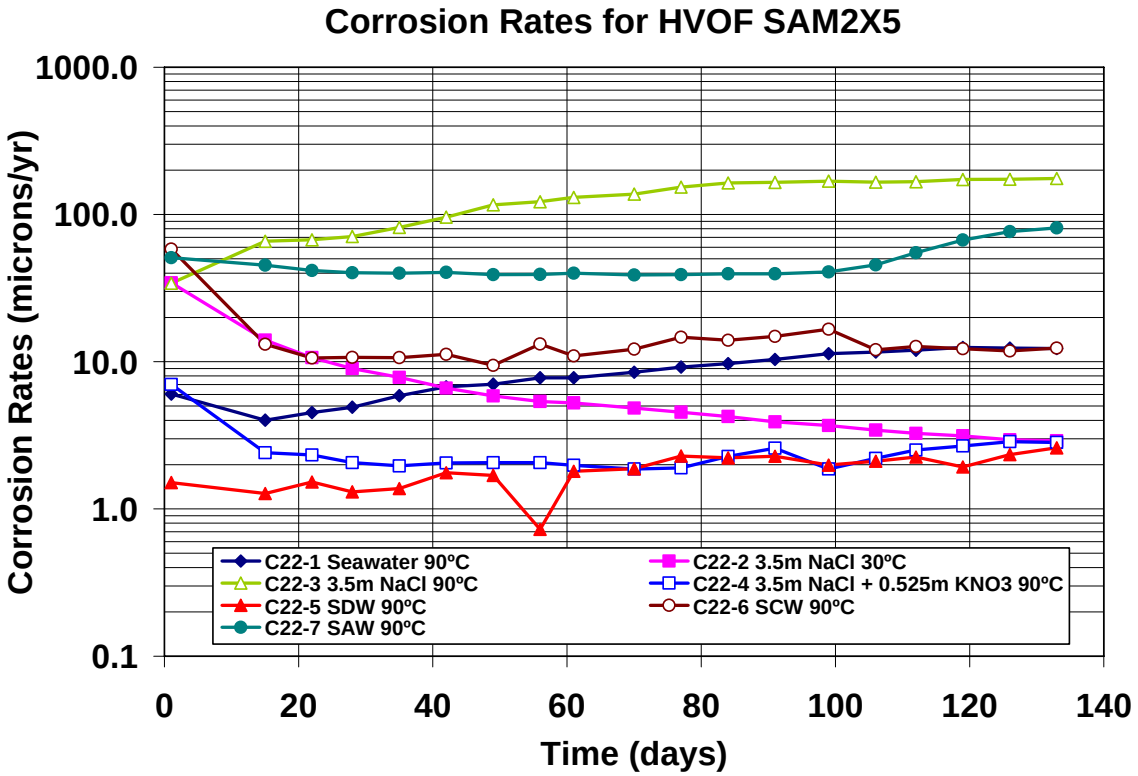

Figure 26 – Apparent corrosion rates of SAM2X5 coatings (powder lot # 06-015 powder) on Alloy C-22 rods during immersion in seven different brines over period of approximately 135 days, as determined with linear polarization.

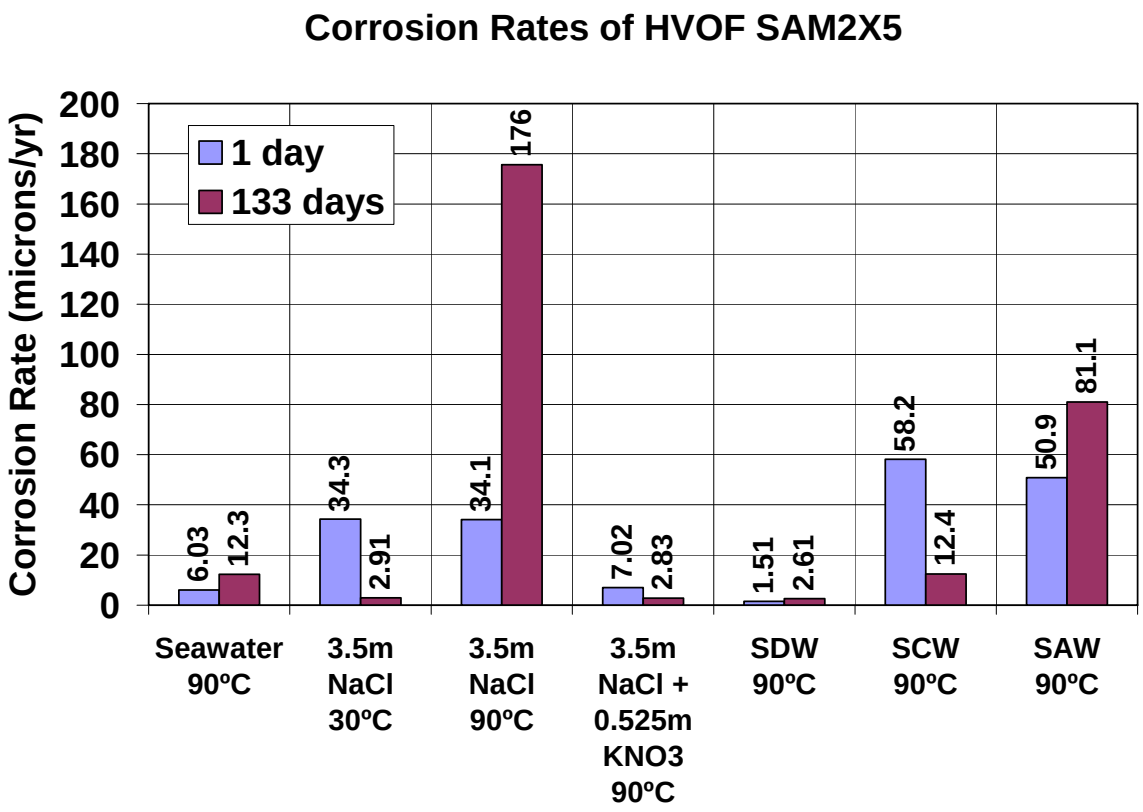

Figure 27 – Apparent corrosion rates of SAM2X5 coatings (powder lot # 06-015 powder) on Alloy C-22 rods after immersion in seven different brines for 1 day and 133 days, as determined with linear polarization.

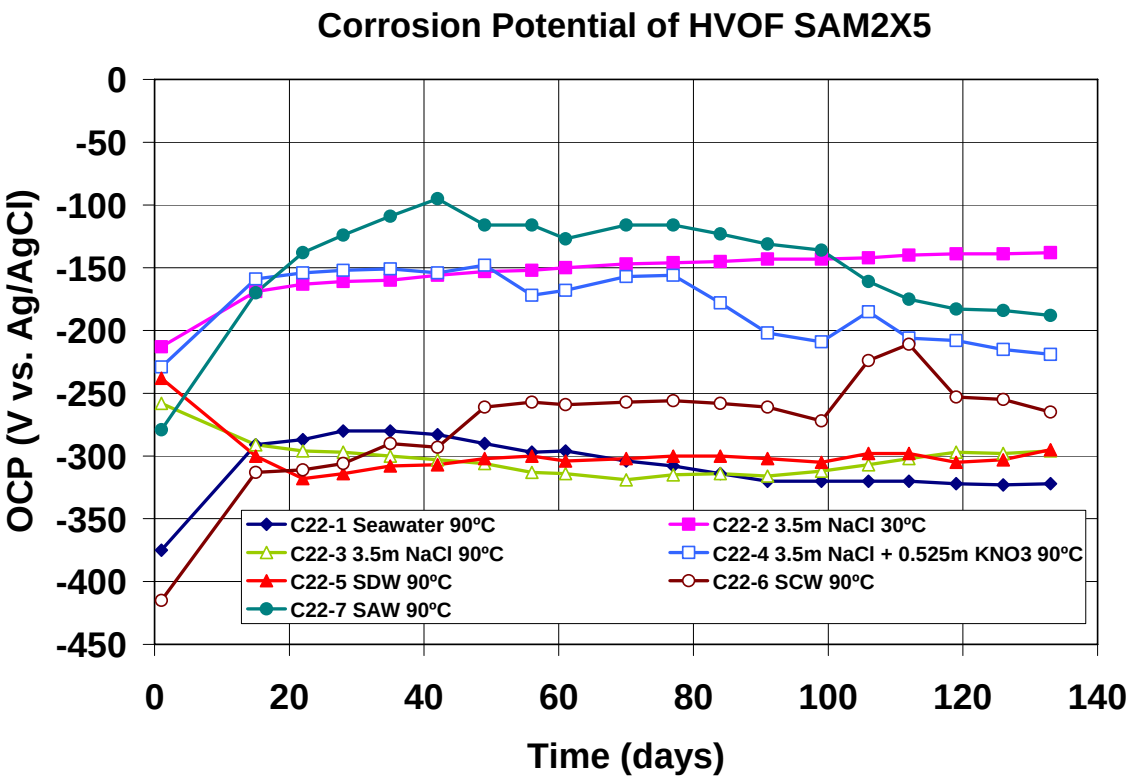

Figure 28 – OCP values of SAM2X5 coatings (powder lot # 06-015 powder) on Alloy C-22 rods during immersion in seven different brines over period of approximately 133 days.

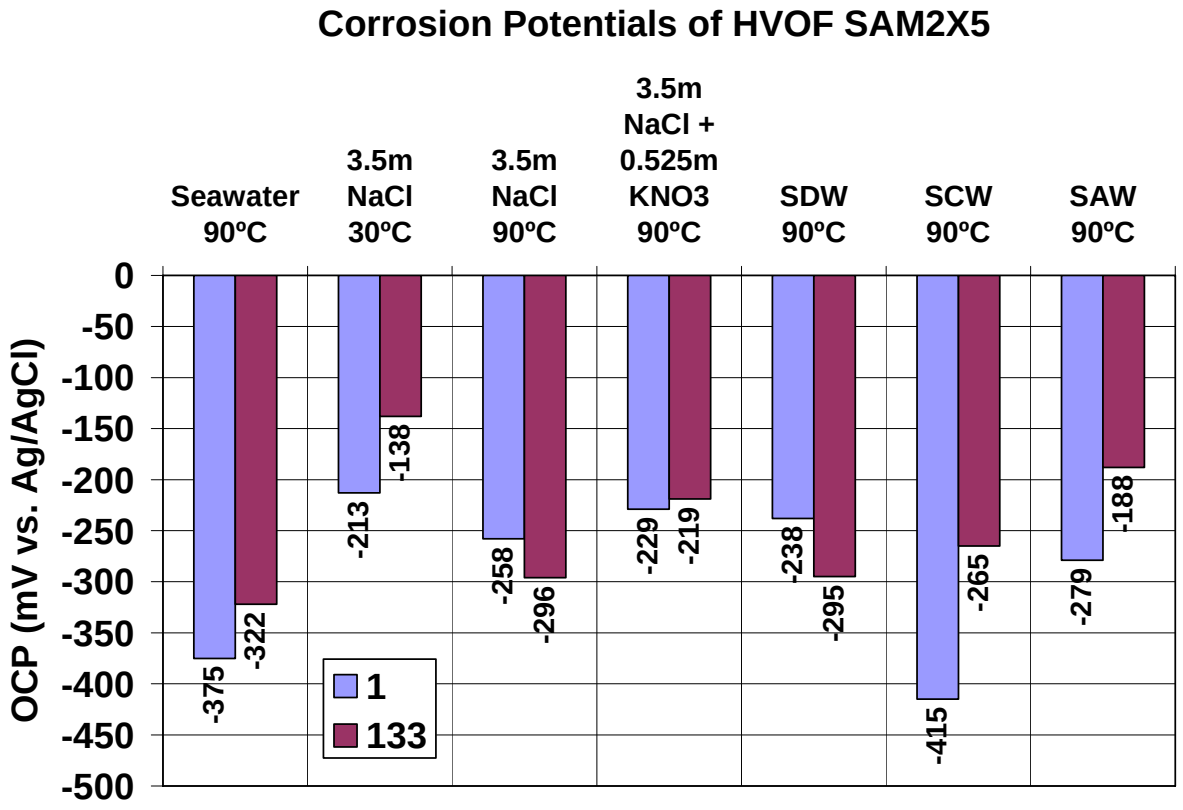

Figure 29 – OCP values for SAM2X5 coatings (powder lot # 06-015 powder) on Alloy C-22 rods after immersion in seven different brines for 1 day and 133 days, as determined with linear polarization.

Figure 30 – Alloy C-22 rod (Sample # C22-1) coated with SAM2X5 (Lot # 06-015 powder) after immersion in natural seawater at 90°C for 133 days immersion; apparent corrosion rate of 12.3 μm/yr determined with linear polarization.

Figure 31 – Alloy C-22 rod (Sample # C22-2) coated with SAM2X5 (Lot # 06-015 powder) after immersion in 3.5-molal NaCl solution at 30°C for 133 days immersion; apparent corrosion rate of 2.91μm/yr determined with linear polarization.

Figure 32 – Alloy C-22 rod (Sample # C22-3) coated with SAM2X5 (Lot # 06-015 powder) after immersion in 3.5-molal NaCl solution at 90°C for 133 days immersion; apparent corrosion rate of 176 μm/yr determined with linear polarization.

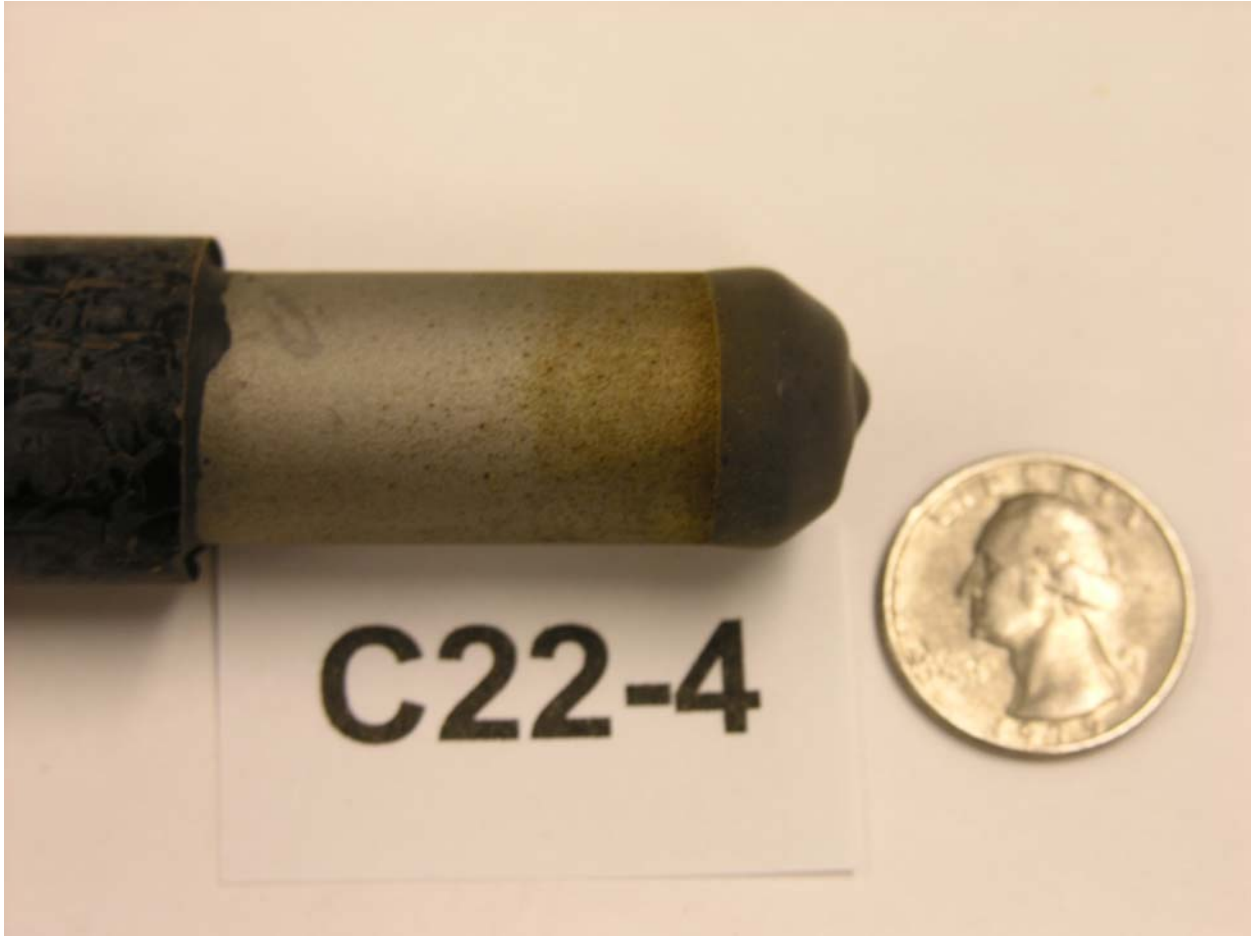

Figure 33 – Alloy C-22 rod (Sample # C22-4) coated with SAM2X5 (Lot # 06-015 powder) after immersion in 3.5-molal NaCl and 0.525-molal KNO_3 solution at 90°C for 133 days immersion; apparent corrosion rate of 2.83 μm/yr determined with linear polarization.

Figure 34 – Alloy C-22 rod (Sample # C22-5) coated with SAM2X5 (Lot # 06-015 powder) after immersion in SDW at 90°C for 133 days immersion; apparent corrosion rate of 2.61 μm/yr determined with linear polarization.

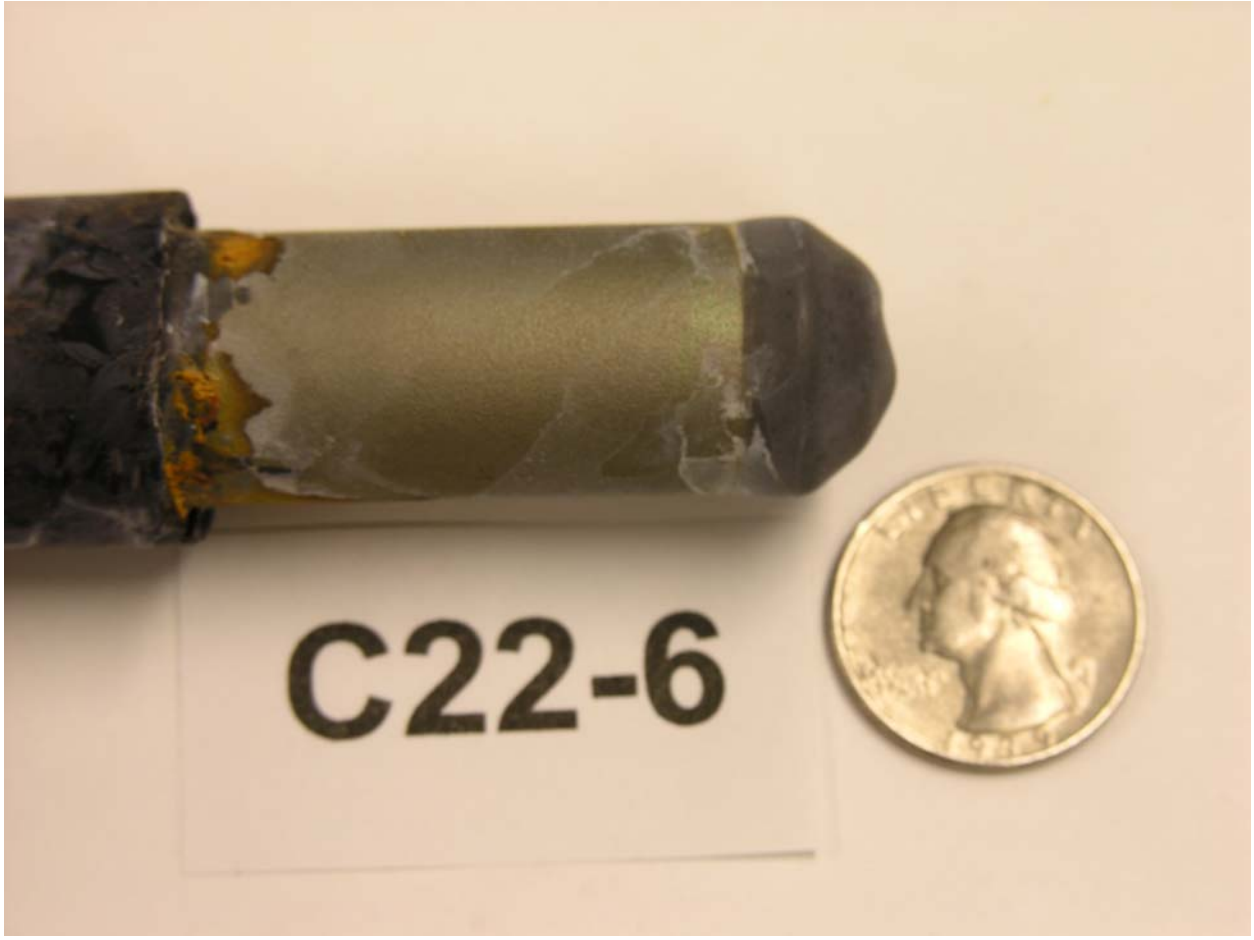

Figure 35 – Alloy C-22 rod (Sample # C22-6) coated with SAM2X5 (Lot # 06-015 powder) after immersion in SCW at 90°C for 133 days immersion; apparent corrosion rate of 12.4 μm/yr determined with linear polarization.

Figure 36 – Alloy C-22 rod (Sample # C22-7) coated with SAM2X5 (Lot # 06-015 powder) after immersion in SAW at 90°C for 133 days immersion; apparent corrosion rate of 81.1 μm/yr determined with linear polarization.

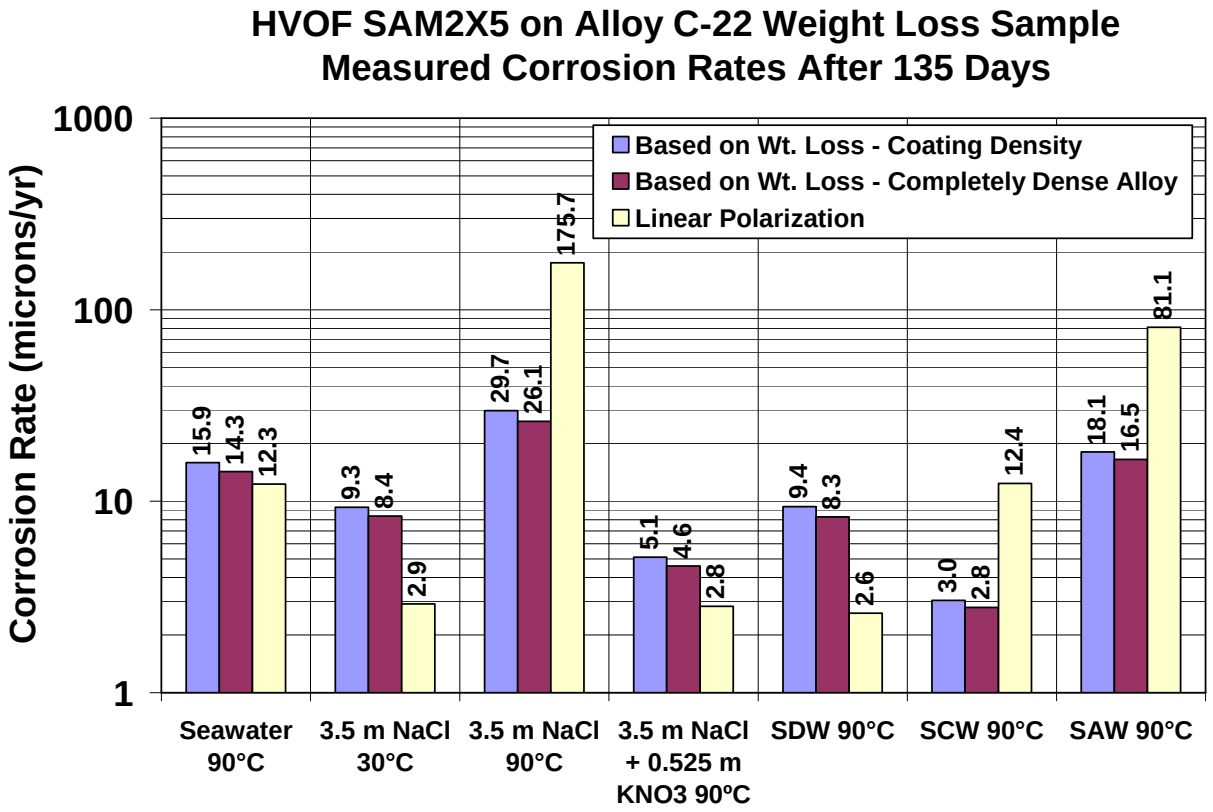

Figure 37 – After 135 days immersion, weight loss and dimensional measurements were used to determine the corrosion rates of SAM2X5 coatings on Alloy C-22 weight-loss samples. Depending upon the assumed coating density, these rates were determined to be: (1) 14.3-15.9 μm/yr in natural seawater at 90°C; (2) 8.4-9.3 μm/yr in 3.5-molal NaCl solution at 30°C; (3) 26.1-29.7 μm/yr in 3.5-molal NaCl solution at 90°C; (4) 4.6-5.1 μm/yr in 3.5-molal NaCl and 0.525-molal KNO_3 solution at 90°C; (5) 8.3-9.4 μm/yr in SDW at 90°C; (6) 2.8-3.0 μm/yr in SCW at 90°C; and (7) 16.5-18.1 μm/yr in SAW at 90°C.

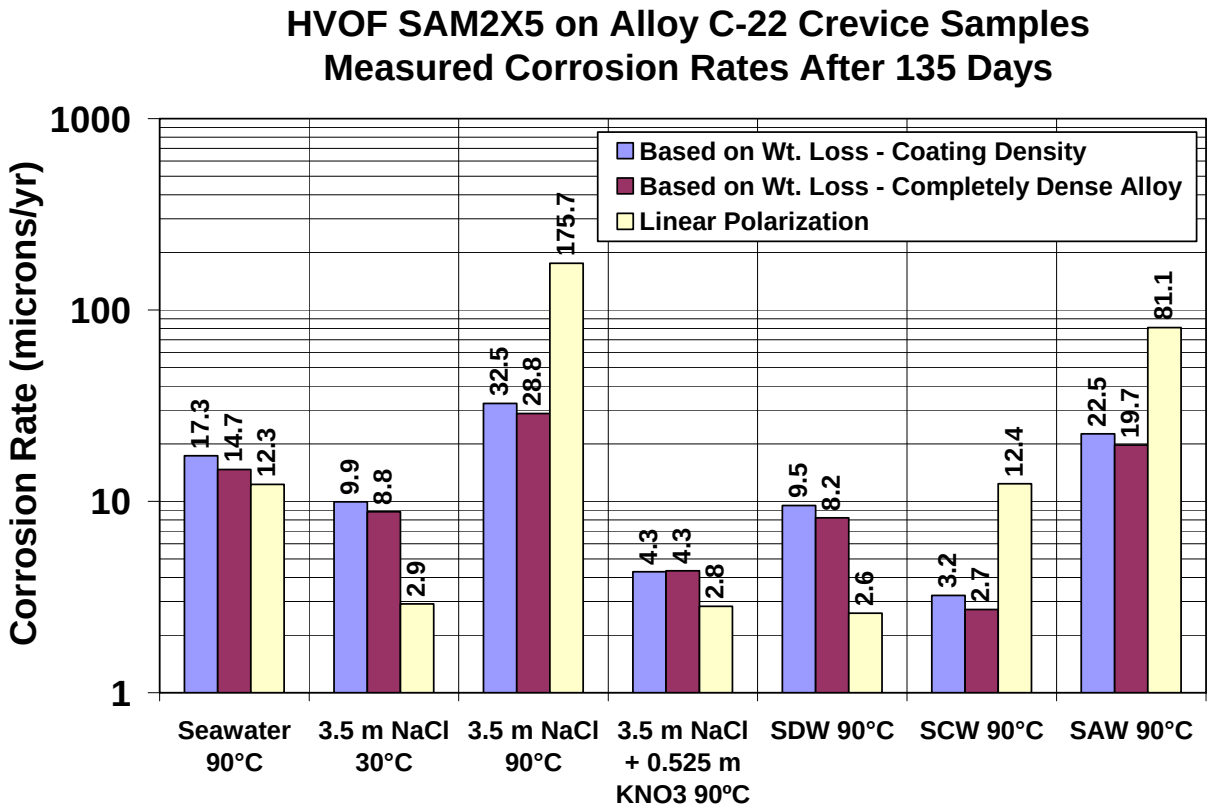

Figure 38 – After 135 days immersion, weight loss and dimensional measurements were used to determine the corrosion rates of SAM2X5 coatings on Alloy C-22 crevice-corrosion samples. Depending upon the assumed coating density, these rates were determined to be: (1) 14.7-17.3 μm/yr in natural seawater at 90°C; (2) 8.8-9.9 μm/yr in 3.5-molal NaCl solution at 30°C; (3) 28.8-32.5 μm/yr in 3.5-molal NaCl solution at 90°C; (4) 4.2-4.3 μm/yr in 3.5-molal NaCl and 0.525-molal KNO_3 solution at 90°C; (5) 8.2-9.5 μm/yr in SDW at 90°C; (6) 2.7-3.2 μm/yr in SCW at 90°C; and (7) 19.7-22.5 μm/yr in SAW at 90°C.

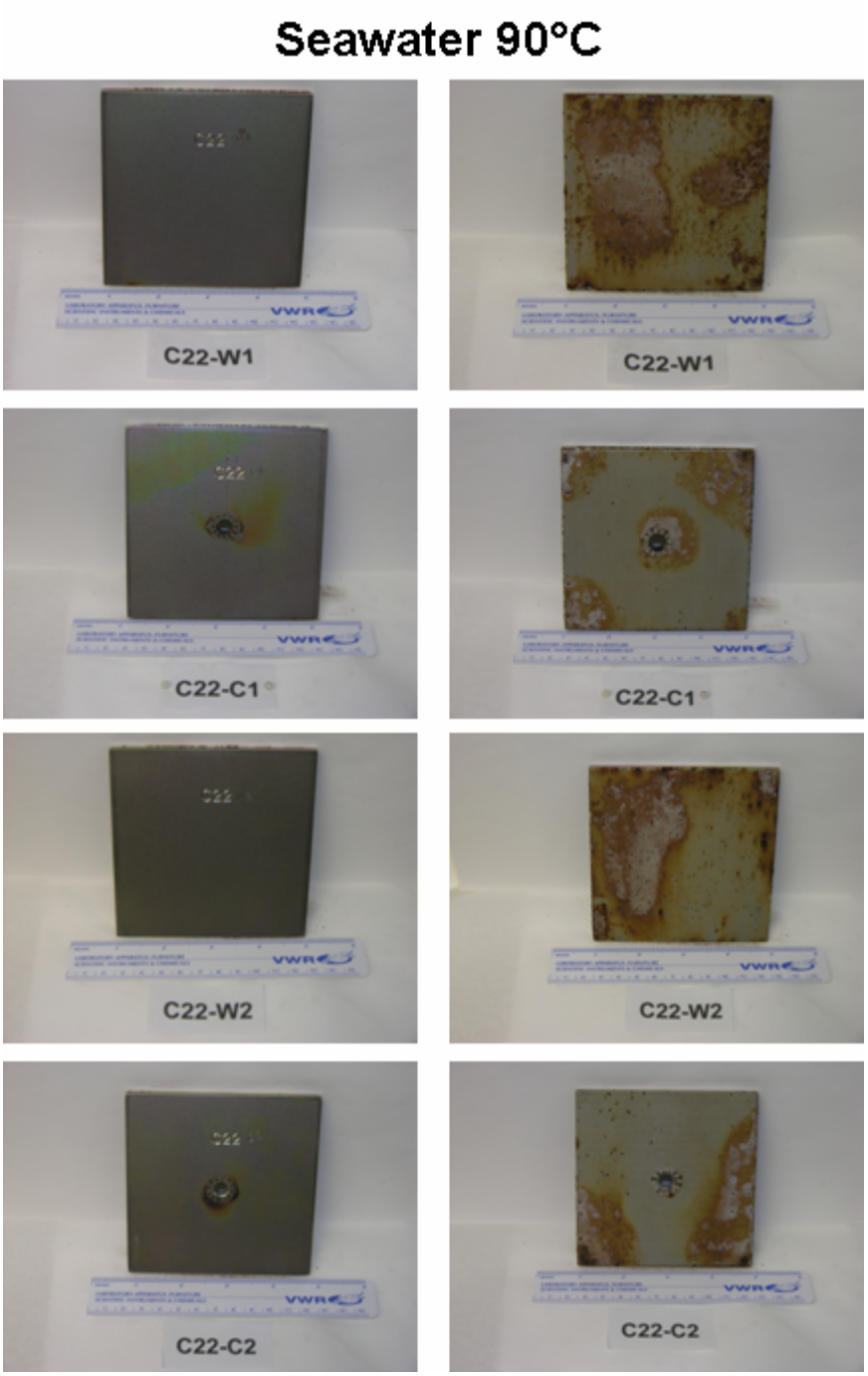

Figure 39 – Weight-loss samples identified as C22-W1 and C22-W2 were used to determine the corrosion rate of 14.3-15.9 μm/yr in natural seawater at 90°C; crevice-corrosion samples identified as C22-C1 and C22-C2 were used to determine the corrosion rate of 14.7-17.3 μm/yr in natural seawater at 90°C.

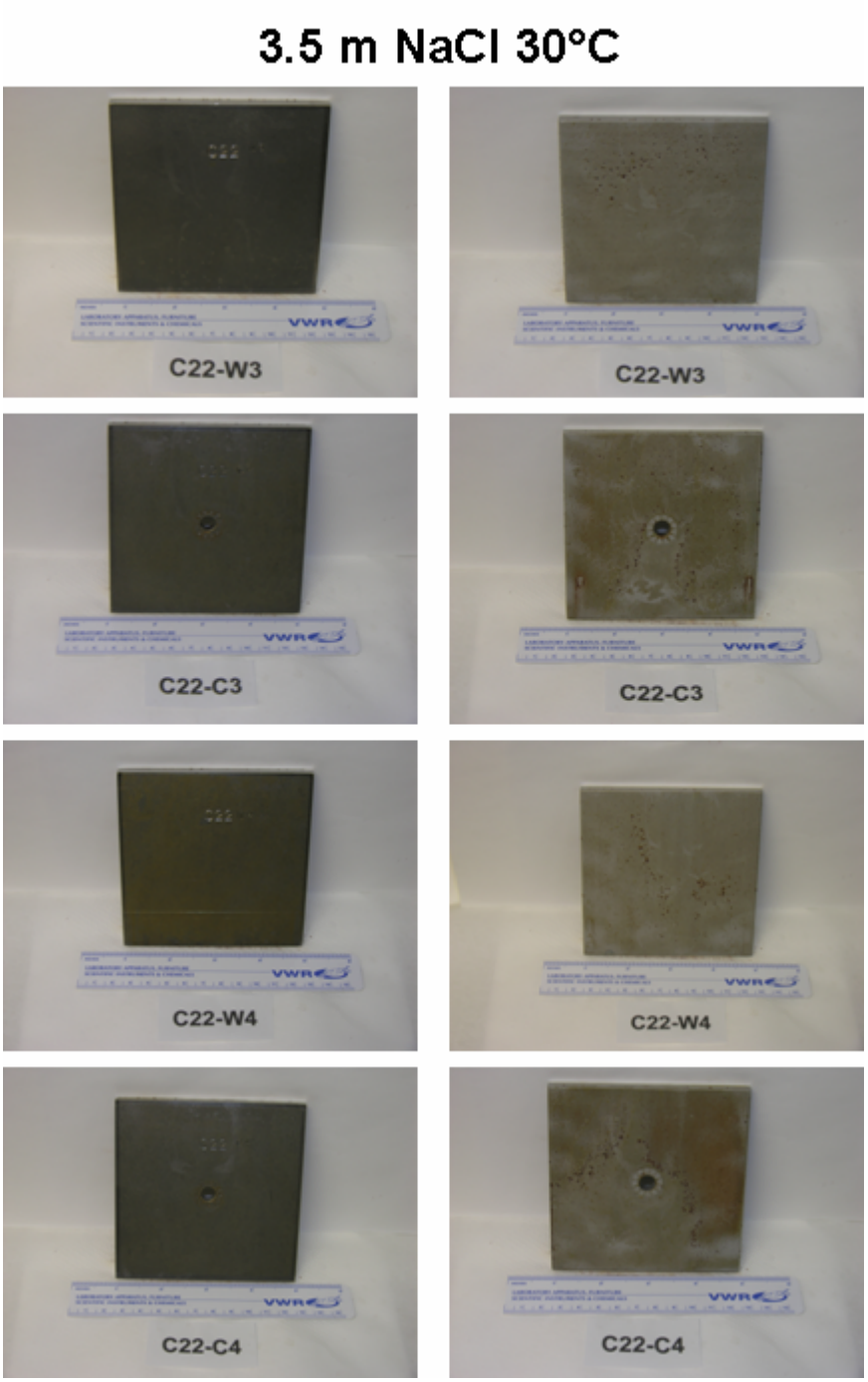

Figure 40 – Weight-loss samples identified as C22-W3 and C22-W4 were used to determine the corrosion rate of 8.4-9.3 μm/yr in 3.5-molal NaCl solution at 30°C; crevice-corrosion samples identified as C22-C3 and C22-C4 were used to determine the corrosion rate of 8.8-9.9 μm/yr in 3.5-molal NaCl solution at 30°C.

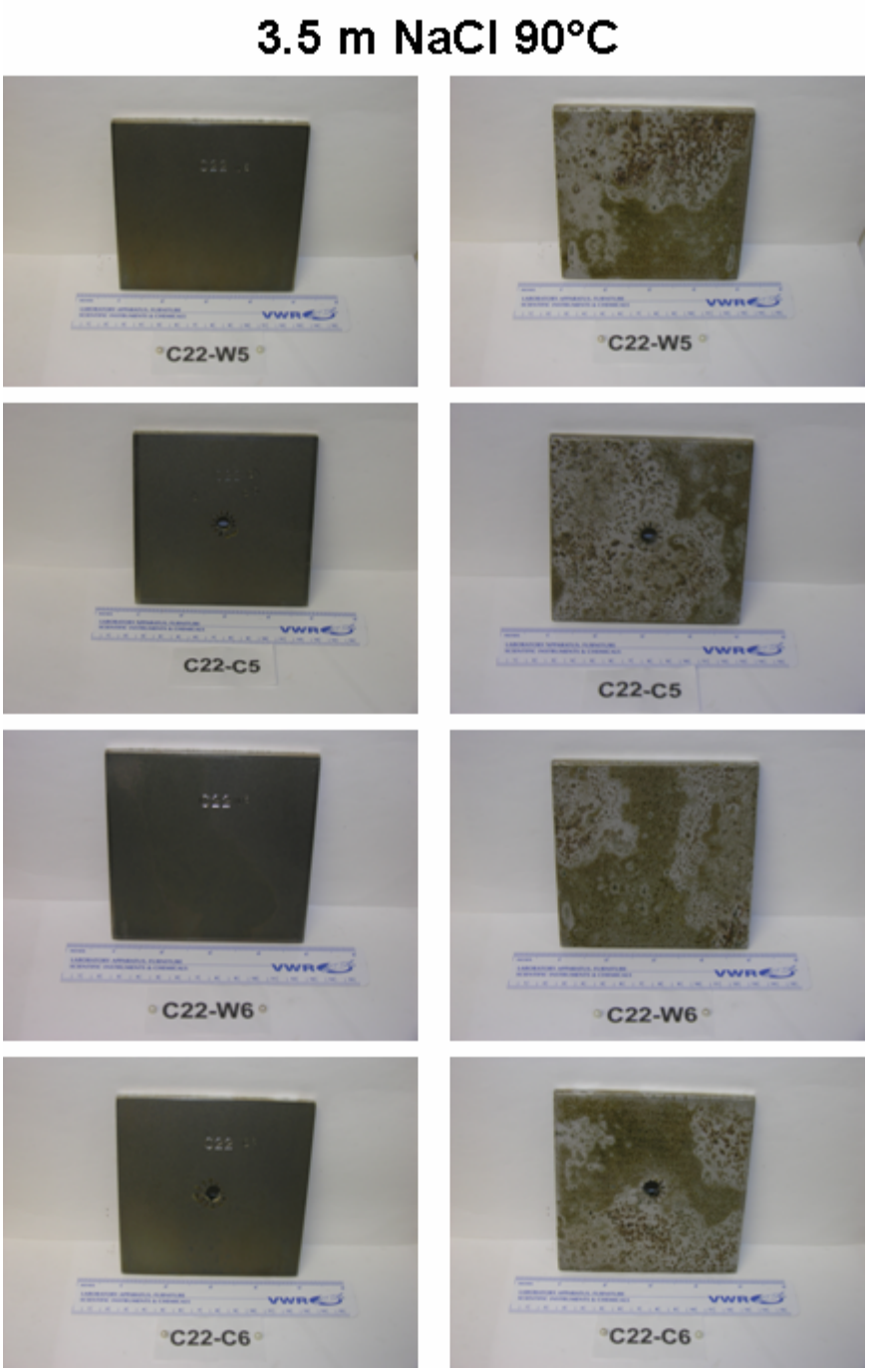

Figure 41 – Weight-loss samples identified as C22-W5 and C22-W6 were used to determine the corrosion rate of 26.1-29.7 µm/yr in 3.5-molal NaCl solution at 90°C; crevice-corrosion samples identified as C22-C5 and C22-C6 were used to determine the corrosion rate of 28.8-32.5 µm/yr in 3.5-molal NaCl solution at 90°C.

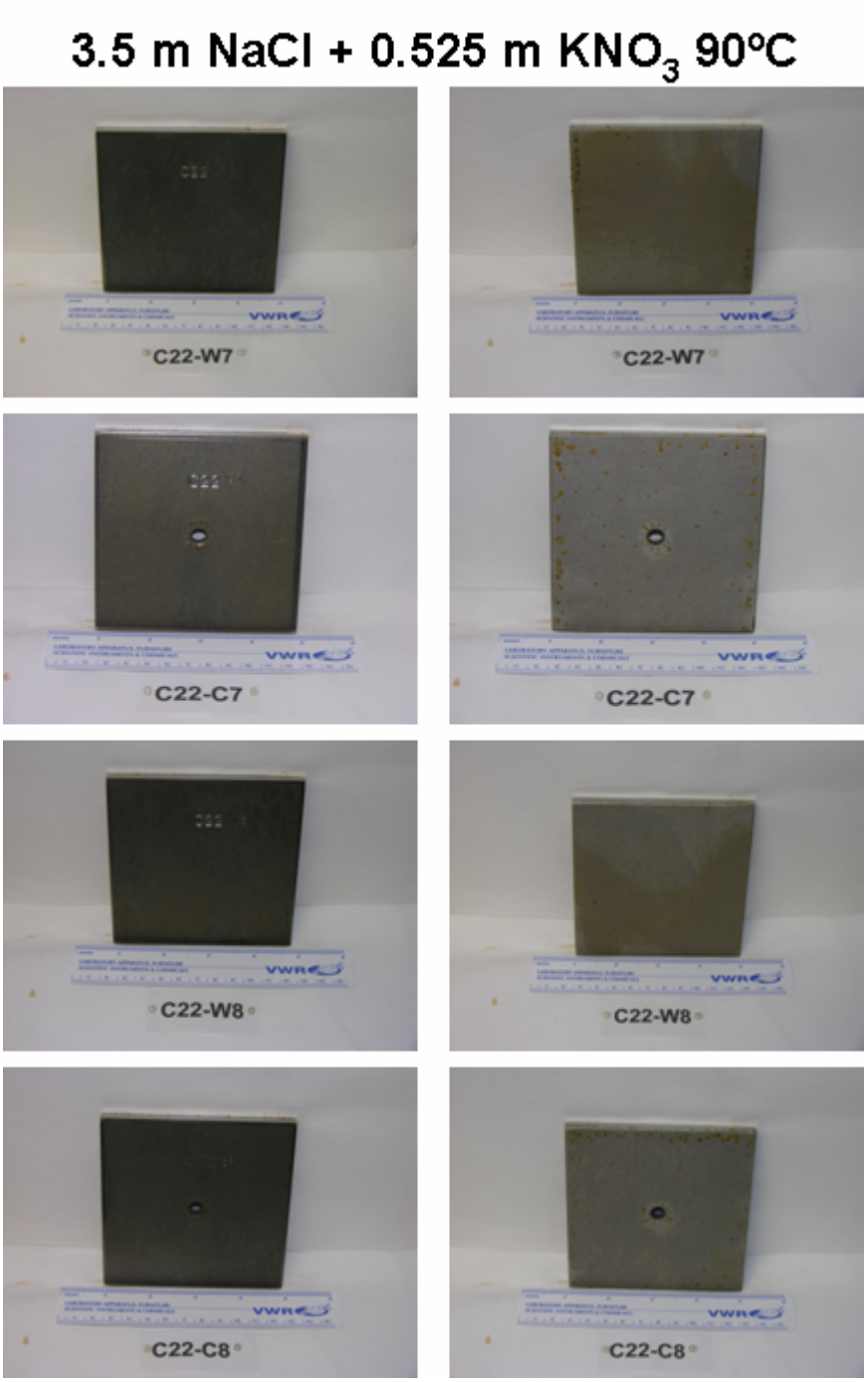

Figure 42 – Weight-loss samples identified as C22-W7 and C22-W8 were used to determine the corrosion rate of 4.6-5.1 μm/yr in 3.5-molal NaCl and 0.525-molal KNO_3 solution at 90°C; crevice-corrosion samples identified as C22-C7 and C22-C8 were used to determine the corrosion rate of 4.2-4.3 μm/yr in 3.5-molal NaCl and 0.525-molal KNO_3 solution at 90°C.

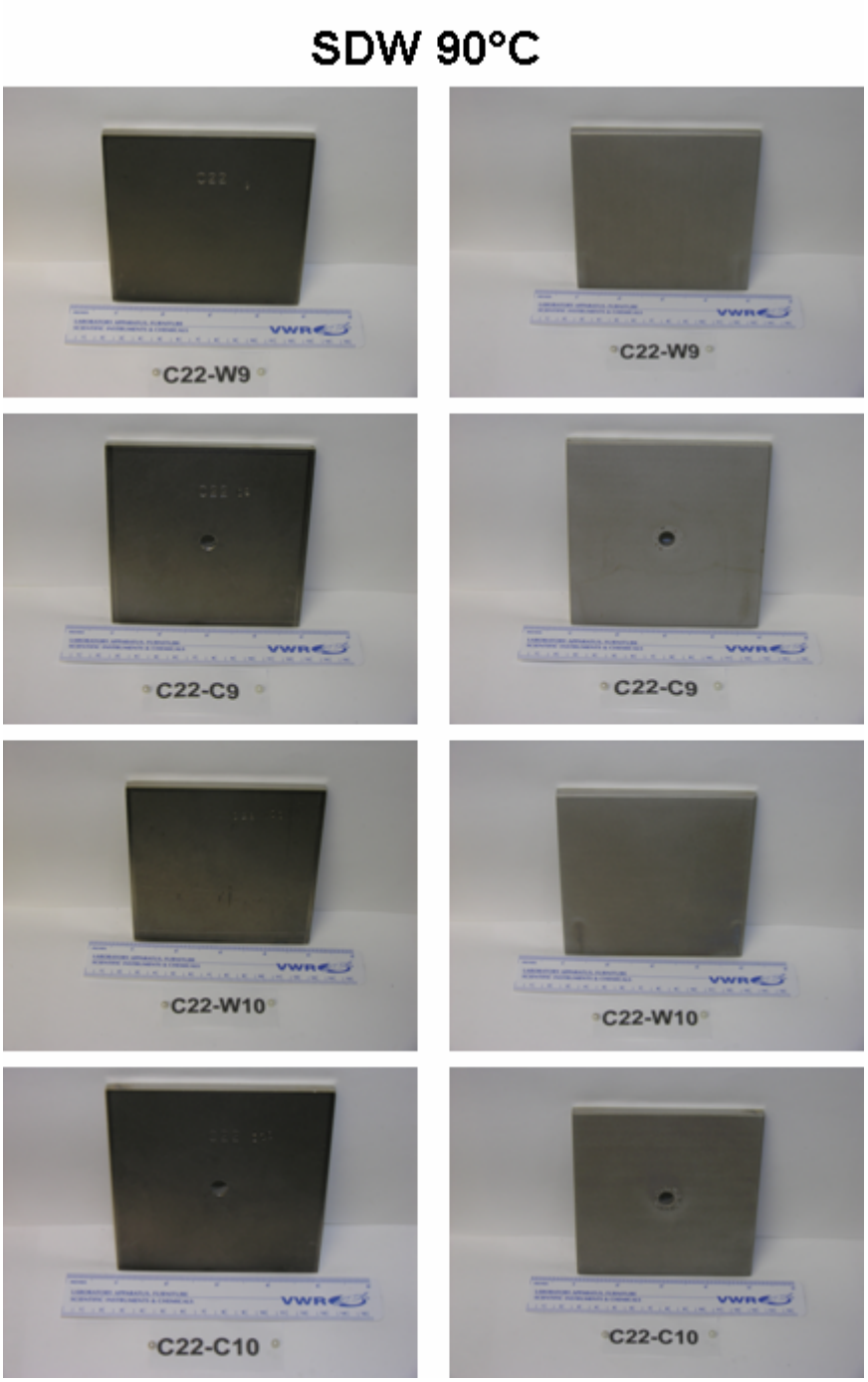

Figure 43 – Weight-loss samples identified as C22-W9 and C22-W10 were used to determine the corrosion rate of 8.3-9.4 µm/yr in SDW at 90°C; crevice-corrosion samples identified as C22-C9 and C22-C10 were used to determine the corrosion rate of 8.2-9.5 µm/yr in SDW at 90°C.

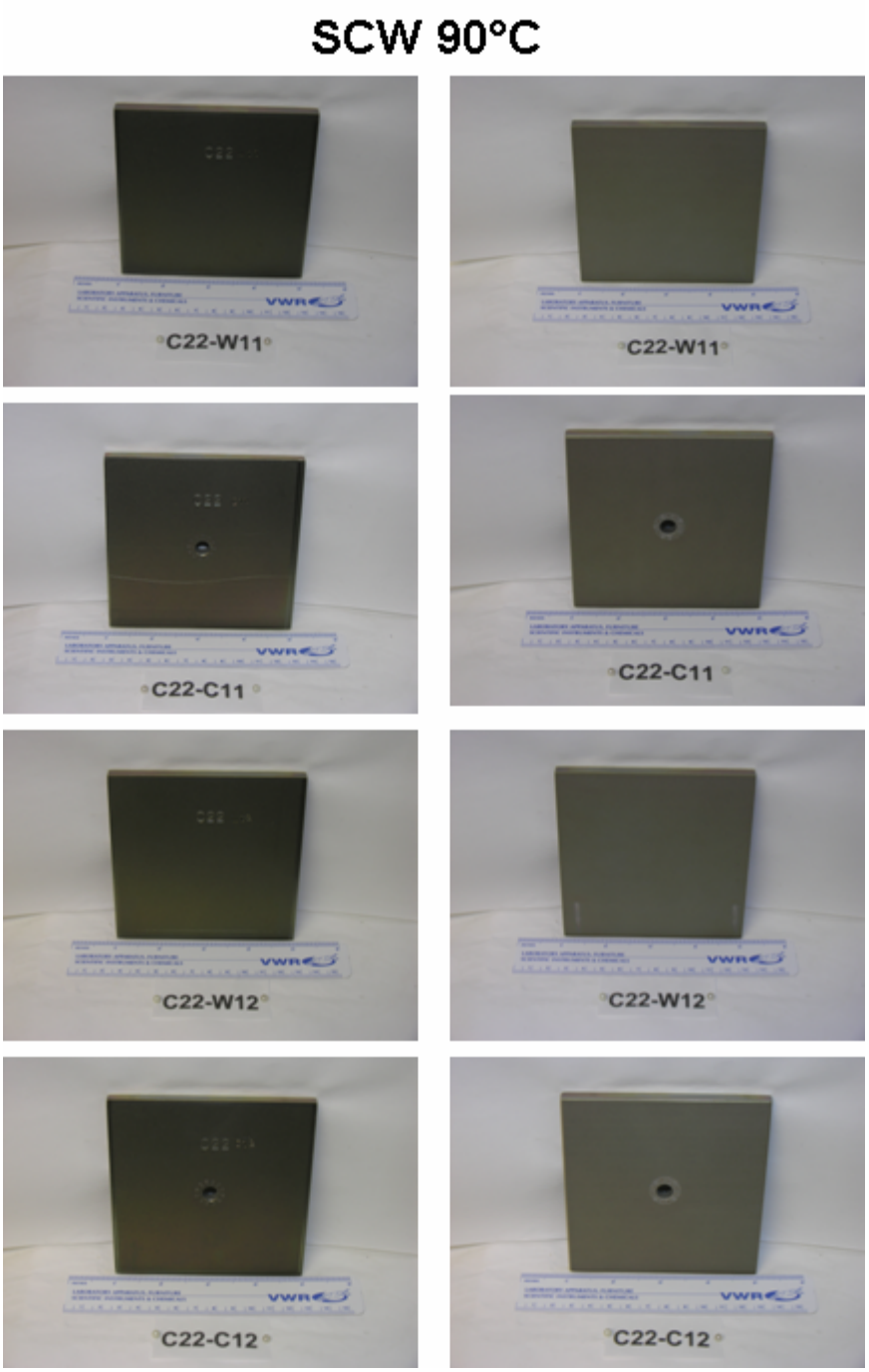

Figure 44 – Weight-loss samples identified as C22-W11 and C22-W12 were used to determine the corrosion rate of 2.8-3.0 µm/yr in SCW at 90°C; crevice-corrosion samples identified as C22-C11 and C22-C12 were used to determine the corrosion rate of 2.7-3.2 µm/yr in SCW at 90°C.

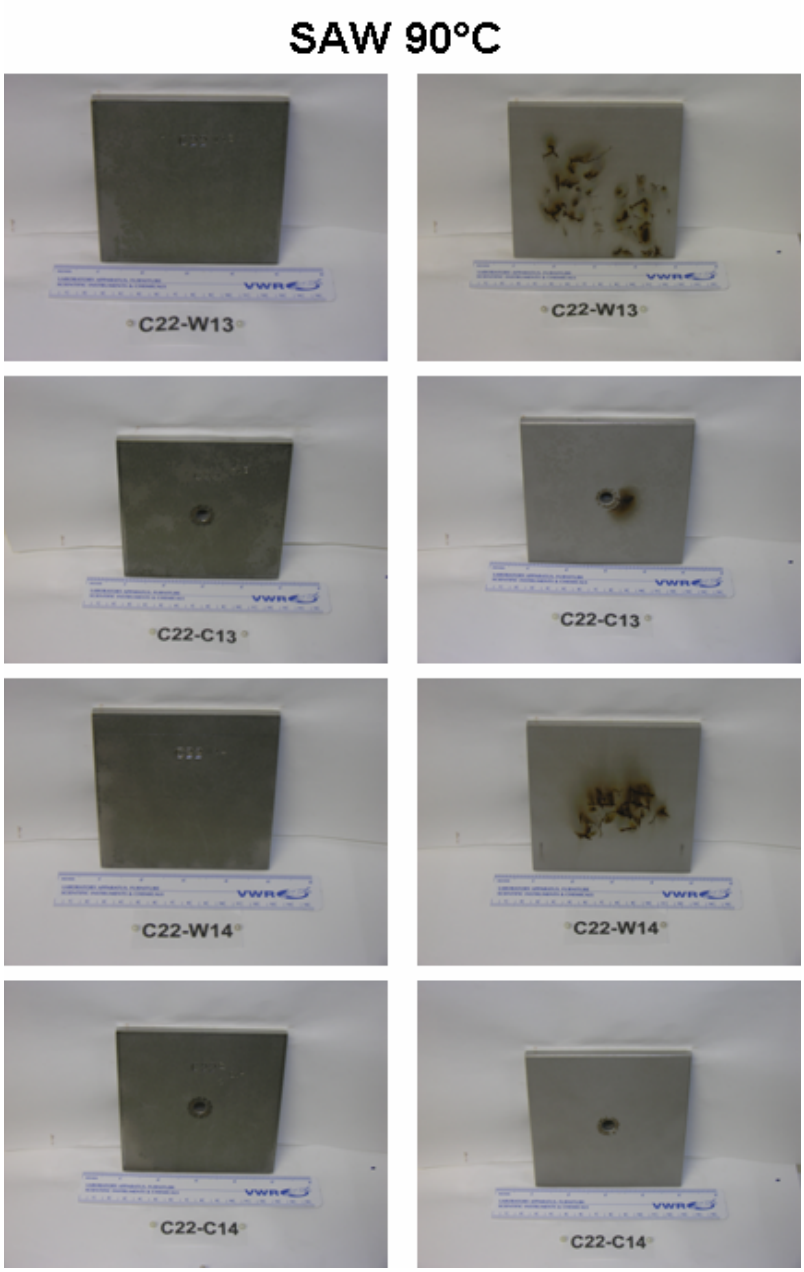

Figure 45 – Weight-loss samples identified as C22-W13 and C22-W14 were used to determine the corrosion rate of 16.5-18.1 μm/yr in SAW at 90°C; crevice-corrosion samples identified as C22-C13 and C22-C14 were used to determine the corrosion rate of 19.7-22.5 μm/yr in SAW at 90°C.